ABSTRACT

Title of dissertation: CORRELATING CRYSTAL STRUCTURE AND OXYGEN STORAGE PROPERTIES IN MIXED-METAL LAYERED OXIDES

Stephanie J. Hong, Doctor of Philosophy, 2026

Dissertation directed by: Professor Efrain E. Rodriguez
Department of Chemistry and Biochemistry

We investigate the relationship between crystal structure and oxygen storage properties in hexagonally layered AB_2O_4-type oxides. The research begins with a deep-dive investigation into $LuMnGaO_4$. Using a combination of neutron and synchrotron X-ray diffraction alongside thermogravimetric analysis, the study characterizes the topotactic transition from the reduced phase ($R\bar{3}m$) to the oxidized phase ($P\bar{3}$). A reversible colorimetric transition from greenish-grey to black upon oxygen uptake is observed, suggesting $LuMnGaO_4$ as a candidate for optical oxygen sensing.

The scope is expanded to the AMnGaO$_4$ series (A = Lu, Yb, In) to examine A-site substitution effects. While the Yb-analogue mirrors the oxygen storage behavior of $LuMnGaO_4$, the In-analogue exhibits a rigid lattice that suppresses oxygen insertion due to stronger In–O bonding. Magnetic characterization further reveals complex magnetic behaviors, including a transition into a frustrated spin-glass state in the oxidized Yb-based phases.

Finally, a comprehensive study across the AFe$_2$O$_4$, AMnFeO$_4$, and AMnGaO$_4$ (A = Lu, Yb, Er, Y) series reveals a divergent structural response to oxidation driven by B-site occupancy. While AFe$_2$O$_4$ undergoes typical lattice expansion upon oxygen intercalation,

Mn-substituted analogues exhibit an unconventional contraction of the *c*-lattice parameter and unit cell volume. This phenomenon is correlated with the changing coordination environment and effective ionic radii of manganese (Mn^{2+} to Mn^{3+}). These findings demonstrate that strategic cation selection at both *A* and *B* sites can affect the structural stability and oxygen capacity in the lattice. Future research should focus on the long-term cycling stability and kinetic performance of these oxides under industrial operating conditions.

CORRELATING CRYSTAL STRUCTURE AND OXYGEN STORAGE PROPERTIES IN MIXED-METAL LAYERED OXIDES

by

Stephanie J. Hong

Dissertation submitted to the Faculty of the Graduate School of the
University of Maryland, College Park in partial fulfillment
of the requirements for the degree of
Doctor of Philosophy
2026

Advisory Committee:
Professor Efrain E. Rodriguez, Chair/Advisor
Professor Zhiwei Li
Professor Mercedes Taylor
Professor Andrei Vedernikov
Professor Yifei Mo, Dean's Representative

© Copyright by
Stephanie J. Hong
2026

Dedication

To my family: my mom, my dad, and my sister.

Your endless love and unwavering support have been my source of strength throughout this journey. I am forever grateful to have you by my side.

Acknowledgments

First and foremost, I would like to express my deepest gratitude to my advisor, Professor Efrain Rodriguez, for his mentorship over the past five years. Beyond the extensive research skills and scientific knowledge I have gained, I have learned the invaluable virtues of patience and respect through his example. I feel privileged to have conducted my doctoral work under his supervision, and I will carry his lessons with me throughout my career.

I would also like to thank my committee members, Professors Zhiwei Li, Mercedes Taylor, Andrei Vedernikov, and Yifei Mo, for their time and for serving on my committee. I thank all the past and present Rodriguez group members for being such wonderful mentors, friends, and collaborators. Our discussions have been fruitful and were essential to the completion of this work.

This research was made possible through the support of several funding agencies and facilities. I acknowledge support from the NIST Cooperative Agreement Nos. 70NANB20H139 and 70NANB17H301. The use of the Spallation Neutron Source (POWGEN experiments IPTS-30479 and IPTS-32619) at Oak Ridge National Laboratory (ORNL) and the Advanced Photon Source (APS) at Argonne National Laboratory was supported by the U.S. Department of Energy, Office of Science, Office of Basic Energy Sciences, under Contract No. DE-AC02-06CH11357. I would like to extend my special thanks to my collaborator Alica Manjón-Sanz (ORNL), for help with neutron data collection, and to Kevin Beyer at 11-IDC (APS) for his assistance with the in-situ X-ray diffraction experiments. A portion of this research was carried out using the shared facilities of the Materials Research Science and Engineering Center (MRSEC) under NSF Award No. DMR-2308708. I also want to thank Dr. Hayden Evans from NIST for his assistance in obtaining synchrotron XRD data from beam line 28-ID-2 of the National Synchrotron Light Source II, a U.S. Department of Energy (DOE) Office of Science User Facility operated for the DOE Office of Science by Brookhaven National Laboratory under Contract No. DE-SC0012704.

At the University of Maryland, I would like to acknowledge the X-ray Crystallographic Center (XCC). My thanks go to the director of XCC, Dr. Peter Zavalij for his instrument training and helpful discussions. I also thank Dr. Karen Gaskell and Yuchen Niu at the Surface Analysis Lab for their assistance with XPS data collection and analysis, and Dr. Liou at the AIM Lab, Nanocenter for his expertise in TEM ED collection and analysis.

List of Figures

1.1 Solid oxide fuel cell. 5
1.2 Solar thermochemical water splitting (STWS). 9

2.1 Structural representation of solid states. 16
2.2 Unit cell showing (100), (010), and (001) planes. 17
2.3 Schematic illustration of X-ray diffraction 18

3.1 TGA, XPS, and EPR spectra for $LuMnGaO_4$ 34
3.2 TGA of $LuMnGaO_4$. 35
3.3 Mn 3s XPS spectra of $LuMnGaO_4$ and $LuMnGaO_{4.5}$ 36
3.4 Neutron powder diffraction patterns and the Rietveld refinement fits for (a) the reduced phase, $LuMnGaO_4$, and (b) the oxidized phase, $LuMnGaO_{4.5}$. . 37
3.5 Neutron powder diffraction pattern of LuMnGaO4 and the Rietveld refinement with a structural model of $R\bar{3}m$. 39
3.6 Neutron powder diffraction pattern of $LuMnGaO_4$ and the Rietveld refinement with a structural model of $R\bar{3}m$. 40
3.7 Neutron diffraction pattern of $LuMnGaO_4$ and Rietveld refinement with a structural model of $C2/m$. 41
3.8 SXPD pattern of $LuMnGaO_4$ and Rietveld refinement with a structural model of $C2/m$. 42
3.9 Neutron diffraction pattern of $LuMnGaO_{4.5}$ and Rietveld refinement with a structural model of $P\bar{3}$. 45
3.10 Neutron diffraction pattern of $LuMnGaO_{4.5}$ and Rietveld refinement with a structural model of $P\bar{3}$. 46
3.11 Rietveld refinement of $LuMnGaO_{4.5}$ at room temperature (RT) with high-resolution SXPD using a structural model of $P\bar{3}$. 47
3.12 (a) SXPD pattern and (b) neutron diffraction pattern of $LuMnGaO_{4.5}$, shown with Rietveld refinement fits using a structural model of $P\bar{3}$ based on a combined refinement of the two datasets. 48
3.13 Crystal structures of (a) $LuMnGaO_4$ ($R\bar{3}m$) and (b) $LuMnGaO_{4.5}$ ($P\bar{3}$) along the c-axis. (c) $LuMnGaO_4$ structure rotated 90° to display the ab plane, highlighting the disordered oxygen. (d) Superimposed Mn/GaO_n polyhedra (n = 4, 5, 6) forming the average Mn/GaO_n double layer structure. 49
3.14 SAED patterns along [001 52

3.15 In-situ SXPD of $LuMnGaO_4$. 53
3.16 Evolution of phase fractions and lattice parameters, a and normalized c, as a function of temperature in air, derived from sequential Rietveld refinements of in-situ SXPD data. 54
3.17 SXPD patterns of $LuMnGaO_4$ at various temperatures showing Rietveld refinement analysis. 55
3.18 Temperature-dependent SXPD patterns of $LuMnGaO_4$. 56
3.19 Color change from $LuMnGaO_4$ to $LuMnGaO_{4.5}$, and corresponding UV-vis spectroscopy measurements. 58

4.1 SXPD patterns with Rietveld fits for (a) $YbMnGaO_4$, (b) $YbMnGaO_{4.5}$, (c) $InMnGaO_4$, and (d) $InMnGaO_4$ heated at 600 °C. 65
4.2 The unit cell of the crystal structure of (a) $YbMnGaO_4$ and (b) $YbMnGaO_{4.5}$. 66
4.3 In situ SXPD contour plot of $YbMnGaO_4$ heated in air from 25 °C to 700 °C, showing the evolution of diffraction peaks associated with the structural transition from $R\bar{3}m$ to $P\bar{3}$ phase. 67
4.4 TGA of $YbMnGaO_4$ (a) and $InMnGaO_4$ (b) measured in air. 69
4.5 TGA of $YbMnGaO_4$ (a) and $InMnGaO_4$ (b) measured under nitrogen. . . . 70
4.6 Ex situ laboratory X-ray diffraction measurements of $InMnGaO_4$ annealed at 25 °C, 600 °C, 750 °C, 800 °C, 830 °C, and 950 °C. 72
4.7 Le Bail fit of the $InMnGaO_4$ sample heated at 950 °C using the $Fddd$ structural model. 73
4.8 Le Bail fit of the $InMnGaO_4$ sample heated at 950 °C using the $Pccn$ structural model. 73
4.9 Le Bail fit of the $InMnGaO_4$ sample heated at 950 °C using the $P222$ structural model. 74
4.10 Crystal structure of $YbMnGaO_4$. 75
4.11 Crystal structure of $InMnGaO_4$. 76
4.12 Temperature-dependent magnetic susceptibility of (a) $YbMnGaO_4$ and (b) $YbMnGaO_{4.5}$ measured under zero field cooled (ZFC) conditions in an applied field of $H = 100$ Oe. 80
4.13 Temperature-dependent magnetic susceptibility of $InMnGaO_4$ measured under zero field cooled (ZFC) conditions in an applied field of $H = 1000$ Oe. 81
4.14 Temperature-dependent magnetic susceptibility (χ) for (a) $YbMnGaO_4$ and (b) $YbMnGaO_{4.5}$, measured under zero-field cooled (ZFC, solid circles) and field cooled (FC, open circles) conditions at 100 Oe (red) and 1000 Oe (blue). 84
4.15 Neutron powder diffraction patterns of $YbMnGaO_4$ from POWGEN, ORNL, meausured at 7 K and 300 K. 85
4.16 Neutron powder diffraction patterns of $YbMnGaO_{4.5}$ from POWGEN, ORNL, measured at 7 K, 20 K, and 300 K. 85

5.1 Crystal structure of a cubic perovskite (ABO_3). 89

5.2 Rietveld refinement of powder X-ray diffraction patterns for reduced and oxidized AMnFeO$_{4+\delta}$ phases. 97
5.3 Comparison of lattice parameters and unit cell volume as a function of A-site ionic radius for AMnFeO$_4$ (A = Lu, Yb, Er, Y). 100
5.4 Comparison of lattice parameters and unit cell volume for oxidized AMnFeO$_{4.5}$ (A = Lu, Yb, Er, Y) as a function of A-site ionic radius. 101
5.5 Evolution of lattice parameters and unit cell volume upon oxidation of AMnFeO$_4$. 102
5.6 Relative structural changes in AMnFeO$_{4+\delta}$ upon oxidation. 102
5.7 TGA of AMnFeO$_4$ (A = Y, Er, Yb, Lu) in flowing air. 103
5.8 TGA of the reduction of oxidized AMnFeO$_{4.5}$ (A = Y, Er, Yb, Lu) in a 3% H$_2$/Ar atmosphere. 104
5.9 TGA of the reduction of oxidized AMnFeO$_{4.5}$ (A = Y, Er, Yb, Lu) in a 3% H$_2$/Ar atmosphere. 104
5.10 Rietveld refinement of powder X-ray diffraction patterns for reduced and oxidized AFe$_2$O$_{4+\delta}$ phases. 108
5.11 Comparison of lattice parameters and unit cell volume as a function of A-site ionic radius for AFe$_2$O$_4$ (A = In, Lu, Yb, Er, Y). 111
5.12 Comparison of lattice parameters and unit cell volume for oxidized AFe$_2$O$_{4.5}$ (A = Lu, Yb, Er) as a function of A-site ionic radius. 112
5.13 Evolution of lattice parameters and unit cell volume upon oxidation of AFe$_2$O$_4$. 113
5.14 Relative structural changes in AFe$_2$O$_{4+\delta}$ upon oxidation. 113
5.15 TGA of AFe$_2$O$_4$ (A = Er, Yb, Lu) in flowing air. 114
5.16 TGA of the reduction of oxidized AMnFeO$_{4.5}$ (A = Y, Er, Yb, Lu) in a 3% H$_2$/Ar atmosphere. 115
5.17 TGA of the reduction of oxidized AFe$_2$O$_{4.5}$ (A = Er, Yb, Lu) in a 3% H$_2$/Ar atmosphere. 115
5.18 TGA of LuFe$_2$O$_{4+\delta}$, LuMnFeO$_{4+\delta}$, LuMnGaO$_{4+\delta}$. 117
5.19 Crystal field splitting and electron configuration of high-spin Mn^{2+} (d^5) in a trigonal bipyramidal coordination. 120
5.20 Crystal field splitting and electron configuration of high-spin Mn^{3+} (d^4) in an octahedral coordination. 120
5.21 TGA of YbFe$_2$O$_{4+\delta}$, YbMnFeO$_{4+\delta}$, YbMnGaO$_{4+\delta}$. 122
5.22 TGA of ErFe$_2$O$_{4+\delta}$ and ErMnFeO$_{4+\delta}$. 123

List of Tables

3.1 Structural parameters obtained from Rietveld refinement with neutron diffraction data (POWGEN, ORNL) for LuMnGaO4 ($R\bar{3}m$) at 300K, with $R_{wp} =$ 4.851 %. 37
3.2 Structural parameters obtained from Rietveld refinement of LuMnGaO4 with neutron diffraction with a structural model of $R\bar{3}m$. 39
3.3 Structural parameters obtained from Rietveld refinement of $LuMnGaO_4$ with neutron diffraction with a structural model of $R\bar{3}m$. 40
3.4 Structural parameters from Rietveld refinement of $LuMnGaO_4$ with neutron diffraction with a structural model of $C2/m$. 41
3.5 Elemental composition (%) analysis using energy dispersive X-ray spectroscopy (EDS) of $LuMnGaO_4$ and $LuMnGaO_{4.5}$. 42
3.6 Structural parameters obtained from Rietveld refinement with neutron diffraction data (POWGEN, ORNL) for $LuMnGaO_{4.5}$ ($P\bar{3}$) at 300 K 43
3.7 Structural parameters from Rietveld refinement of $LuMnGaO_4$ with neutron diffraction with a structural model of $C2/m$. 45
3.8 Structural parameters from Rietveld refinement of $LuMnGaO_{4.5}$ with a structural model of $P\bar{3}$. 46
3.9 Structural parameters from Rietveld refinement of $LuMnGaO_{4.5}$ with high-resolution SXPD using a structural model of $P\bar{3}$. 47
3.10 Structural parameters from the combined Rietveld refinement of $LuMnGaO_{4.5}$ with synchrotron PXRD and neutron diffraction with a structural model of $P\bar{3}$. 48

4.1 Structural parameters obtained from Rietveld refinement of SXPD data for $YbMnGaO_4$, $YbMnGaO_{4.5}$, $InMnGaO_4$, and annealed $InMnGaO_4$, measured at 300K. 68

5.1 Reagent company and purity 91
5.2 Refined structural parameters for reduced AMnFeO$_4$ (A = Y, Er, Yb, Lu) obtained from Rietveld refinement of powder X-ray diffraction data at 300 K. 98
5.3 Refined structural parameters for oxidized AMnFeO$_{4.5}$ (A = Y, Er, Yb, Lu) obtained from Rietveld refinement of powder X-ray diffraction data at 300 K. 99
5.4 Experimental weight gain and calculated oxygen stoichiometry for AMnFeO$_4$ (A = Y, Er, Yb, Lu) following oxidation in air up to 700 °C. 103

5.5 Experimental weight loss and calculated oxygen stoichiometry for oxidized AMnFeO$_{4+\delta}$ (A = Y, Er, Yb, Lu) following reduction in 3% H$_2$/Ar up to 750 °C. 105
5.6 Refined structural parameters for reduced AFe$_2$O$_4$ (A = Er, Yb, Lu, Y, In) obtained from Rietveld refinement of powder X-ray diffraction data at 300 K. 109
5.7 Refined structural parameters for oxidized AFe$_2$O$_{4.5}$ (A = Er, Yb, Lu) obtained from Rietveld refinement of powder X-ray diffraction data at 300 K. 110
5.8 Experimental weight gain and calculated oxygen stoichiometry for AFe$_2$O$_4$ (A = Er, Yb, Lu) following oxidation in air up to 700 °C. 114
5.9 Experimental weight loss and calculated oxygen stoichiometry for oxidized AFe$_2$O$_{4+\delta}$ (A = Er, Yb, Lu) following reduction in 3% H$_2$/Ar at 700 °C (Er), 715 °C (Yb), 650 °C (Lu). 116
5.10 Refined lattice parameters (a, c), unit cell volume (V) for reduced (R) and oxidized (O) phases of LuFe$_2$O$_{4+\delta}$, LuMnFeO$_{4+\delta}$, LuMnGaO$_{4+\delta}$ and oxygen stoichiometry (δ) after oxygen uptake. 117
5.11 Refined lattice parameters (a, c), unit cell volume (V) for reduced (R) and oxidized (O) phases of YbFe$_2$O$_{4+\delta}$, YbMnFeO$_{4+\delta}$, YbMnGaO$_{4+\delta}$ and oxygen stoichiometry (δ) after oxygen uptake. 122
5.12 Refined lattice parameters (a, c), unit cell volume (V) for reduced (R) and oxidized (O) phases of ErFe$_2$O$_{4+\delta}$ and ErMnFeO$_{4+\delta}$ and oxygen stoichiometry (δ) after oxygen uptake. 123

List of Abbreviations

APS	Advanced Photon Source
ED	Electron Diffraction
EDS	Energy Dispersive X-ray Spectroscopy
EPR	Electron Paramagnetic Resonance
FC	Field-cooled
GDC	Gadolinium-doped Ceria
HRTEM	High-Resolution Transmission Electron Microscopy
MPMS	Magnetic Properties Measurement System
OSC	Oxygen Storage Capacity
OSM	Oxygen Storage Material
ORR	Oxygen Reduction Reaction
PEC	Photoelectrochemical
SAED	Selected Area Electron Diffraction
SOFC	Solid Oxide Fuel Cell
SQUID	Superconducting Quantum Interference Device
STWC	Solar-Thermochemical Water Splitting
SXPD	Synchrotron X-ray Powder Diffraction
TEM	Transmission Electron Microscopy
TGA	Thermogravimetric Analysis
TOF	Time-of-flight
TWC	Three-way catalyst
UV-vis DRS	Ultraviolet-Visible Diffuse Reflectance Spectroscopy
XRD	X-ray Diffraction
YSZ	Yttria-Stabilized Zirconia
ZFC	Zero Field-cooled

Table of Contents

Dedication ii

Acknowledgements iii

List of Figures vii

List of Tables ix

List of Abbreviations x

1 Introduction 1
- 1.1 Oxygen storage materials . . . 1
- 1.2 Applications . . . 2
  - 1.2.1 Three-way catalysts (TWCs) . . . 2
  - 1.2.2 Solid oxide fuel cells (SOFCs) . . . 4
  - 1.2.3 Solar thermochemical water splitting (STWS) . . . 6
  - 1.2.4 Limitations of current oxygen storage materials . . . 9
- 1.3 AB_2O_4 compounds . . . 10
- 1.4 Outline of the thesis . . . 12

2 Methodology 14
- 2.1 Solid State Synthesis . . . 14
- 2.2 Diffraction Techniques . . . 15
  - 2.2.1 Crystalline Materials . . . 15
  - 2.2.2 X-ray Diffraction . . . 17
  - 2.2.3 Neutron Diffraction . . . 20
  - 2.2.4 Powder Diffraction Analysis . . . 21
    - 2.2.4.1 Rietveld Analysis . . . 21
    - 2.2.4.2 Le Bail analysis . . . 22
- 2.3 Thermogravimetric Analysis . . . 23
- 2.4 Electron Microscopy . . . 24

2.4.1 Transmission Electron Microscopy . . . 24
2.4.2 Scanning Electron Microscopy . . . 25
2.5 UV-vis Diffuse Reflectance Spectroscopy . . . 25
2.6 Superconducting Quantum Interference Device (SQUID) . . . 26

3 Reversible Structural and Colorimetric Transitions in $LuMnGaO_4$ upon Oxygen Uptake and Release 28
3.1 Introduction . . . 28
3.2 Experimental . . . 30
3.2.1 Materials Synthesis . . . 30
3.2.2 Thermogravimetric Analysis (TGA) . . . 30
3.2.3 X-ray photoelectron spectroscopy (XPS) . . . 30
3.2.4 Electron paramagnetic resonance (EPR) . . . 31
3.2.5 High-resolution synchrotron X-ray and neutron diffraction . . . 31
3.2.6 Transmission Electron Microscopy (TEM) . . . 32
3.2.7 UV-Vis Reflectance Spectroscopy . . . 32
3.2.8 Energy Dispersive X-ray Spectroscopy (EDS) . . . 33
3.3 Results and Discussion . . . 33
3.3.1 Reversible oxgyen uptake of $LuMnGaO_4$ . . . 33
3.3.2 Crystal Structure of the reduced phase, $LuMnGaO_4$ . . . 36
3.3.3 Crystal structure of the oxidized phase, $LuMnGaO_{4.5}$ . . . 43
3.3.4 Diffuse scattering and modulation structures . . . 50
3.3.5 Structural evolution of $LuMnGaO_4$ during oxygen insertion . . . 51
3.3.6 Color change from $LuMnGaO_4$ to $LuMnGaO_{4.5}$ . . . 57
3.4 Conclusion . . . 59

4 Comparative Structural and Functional Analysis of AMnGaO$_4$ (A = Yb and In) 60
4.1 Introduction . . . 60
4.2 Experimental . . . 62
4.2.1 Materials synthesis . . . 62
4.2.2 Thermogravimetric analysis (TGA) . . . 62
4.2.3 X-ray diffraction (XRD) . . . 63
4.2.4 Neutron diffraction . . . 63
4.2.5 Magnetic susceptibility measurements with SQUID . . . 63
4.3 Results and Discussion . . . 64
4.3.1 Structural analysis upon annealing . . . 64
4.3.2 Oxygen storage properties . . . 69
4.3.3 Origin of the distinct behavior of $InMnGaO_4$ . . . 74
4.3.4 Oxidation states and magnetism . . . 77
4.4 Conclusion . . . 86

5 Systematic Study of A and B site Substitutions in AB_2O_4 Oxides 88
5.1 Introduction . . . 88
5.2 Experimental . . . 90
5.2.1 Materials synthesis . . . 90
5.2.2 Thermogravimetric analysis (TGA) . . . 91
5.2.3 X-ray diffraction (XRD) . . . 92
5.3 Results and Discussion . . . 92
5.3.1 A-site substitution . . . 92
5.3.1.1 AMnFeO$_4$ (A = Y, Er, Yb, Lu) series . . . 92
5.3.1.2 AFe$_2$O$_4$ (A = Er, Yb, Lu) series . . . 106
5.3.2 B-site substitution . . . 117
5.4 Conclusion . . . 124

6 Conclusions and Future Directions 125

Bibliography 127

Chapter 1: Introduction

1.1 Oxygen storage materials

Metal oxides play a critical role in modern materials science due to their structural versatility and broad functionality in environmental and energy technologies. Their technological impact comes from their tunable physicochemical properties, which are determined by crystal structure, stoichiometry, defect chemistry, etc. [1–4]. Subtle variations in these structural parameters give rise to a wide spectrum of properties, including mechanical robustness, optical transparency, semiconducting behavior, photosensitivity, and redox activity [5]. In addition, many metal oxides are composed of earth-abundant elements, making them economically viable and more sustainable alternatives to materials reliant on scarce resources. Their intrinsic stability and compatibility with safety standards support their scalable integration into advanced energy systems.

In many of these systems, metal oxides function specifically as oxygen storage materials (OSMs) or oxygen carriers. OSMs are defined by their capacity to reversibly uptake and release oxygen within their crystalline lattices, typically through the formation and annihilation of oxygen vacancies. This process is driven by changes in temperature or the external partial pressure of oxygen (P_{O_2}). The efficiency of an OSM is depends on its oxygen storage capacity and the kinetics of oxygen ion diffusion, both of which are fundamentally rooted in the material's electronic and structural configuration.

They serve critical roles in a wide range of systems, including battery electrodes, three-

way catalysts, and solid oxide fuel cells, as well as in chemical looping processes. By facilitating precise redox control, OSMs enable the high-efficiency performance required for modern sustainable energy solutions. The following sections detail their implementation in three primary applications: optimization of three-way catalysts for emission control, the development of solid oxide fuel cells for electrochemical energy conversion, and the advancement of solar thermochemical hydrogen production.

1.2 Applications

1.2.1 Three-way catalysts (TWCs)

Cerium-based oxides are well established as essential promoters within automotive TWCs. These exhaust emission control devices are engineered to mitigate the environmental impact of gasoline combustion by simultaneously oxidizing carbon mooxide (CO) and unburnt hydrocarbons (C_xH_y) while reducing nitrogen oxides (NO_x). These simultaneous reactions are represented by the following equations:

$$2\,\mathrm{NO} + 2\,\mathrm{CO} \longrightarrow \mathrm{N_2} + 2\,\mathrm{CO_2} \tag{1.1}$$

$$2\,\mathrm{CO} + \mathrm{O_2} \longrightarrow 2\,\mathrm{CO_2} \tag{1.2}$$

$$2\,\mathrm{C_2H_6} + 7\,\mathrm{O_2} \longrightarrow 4\,\mathrm{CO_2} + 6\,\mathrm{H_2O} \tag{1.3}$$

TWCs utilize noble metals such as platinum, palladium, and rhodium dispersed upon a ceramic honeycomb framework. The addition of a promoter is critical to the efficiency of the system. A promoter is a material that can temporarily store and release oxygen, a property known as oxygen storage capacity (OSC). This mechanism allows the catalyst to buffer fluctuations in the exhaust gas stream, thereby maintaining the stoichiometric air-to-fuel ratio required for optimal conversion.

The funtionality of these materials is governed by the reversible redox transition between the Ce^{4+} and Ce^{3+} oxidation states. Under oxygen-rich conditions, the material consumes excess oxygen to oxidize Ce^{3+} to Ce^{4+}. Conversely, under fuel-rich conditions, Ce^{4+} is reduced to Ce^{3+}, facilitating the release of lattice oxygen to react with adsorbed pollutants. This process is accompanied by the formation and migration of oxygen vacancies within the lattice, as described by Kröger-Vink notation [6]:

$$2\mathrm{Ce}_{\mathrm{Ce}}^{\times} + \mathrm{O}_{\mathrm{O}}^{\times} \rightleftharpoons 2\mathrm{Ce}_{\mathrm{Ce}}^{\prime} + \mathrm{V}_{\mathrm{O}}^{\bullet\bullet} + \frac{1}{2}\mathrm{O}_2(g) \tag{1.4}$$

In a Kröger-Vink notation, each atom or vacancy is represented as X_Y^Z. X is the occupant (element symbol or V for vacancy); Y is the site (host element or i for interstitial); and Z is the relative charge ($\bullet$ for positive, $'$ for negative, and $\times$ for neutral). In Equation (1.4):

- $\mathrm{Ce}_{\mathrm{Ce}}^{\times}$ and $\mathrm{O}_{\mathrm{O}}^{\times}$: Represent the perfect lattice where atoms sit on their own sites with no relative charge.
- $\mathrm{V}_{\mathrm{O}}^{\bullet\bullet}$: An oxygen vacancy. Removing a lattice O^{2-} leaves a site that is $+2$ more positive than the original, hence the two dots.
- $\mathrm{Ce}_{\mathrm{Ce}}^{\prime}$: A Ce^{3+} ion sitting on a site normally meant for Ce^{4+}. This creates a relative charge of -1 (one prime).

Modern TWCs typically use a CeO_2-ZrO_2 solid solution, which provides the necessary thermal stability for high-temperature operation, often exceeding 1000 °C for long periods. Pure CeO_2 has a cubic fluorite structure and the incorporation of zirconium (Zr^{4+}) ions into the ceria lattice stabilizes the structure and enhances the overall OSC. This occurs because the substitution of the smaller Zr^{4+} cation [7] reduces the lattice strain associated with the expansion of the unit cell during the Ce^{4+} to Ce^{3+} reduction, thereby increasing the mobility of bulk oxygen [8].

The phase behavior of $Ce_xZr_{1-x}O_2$ is highly sensitive to both temperature and molar

composition. At the elevated temperatures characteristic of catalytic operation, at around 1055 °C, the solution is in a tetragonal, monoclinic, or cubic phase at $x = 0.112$, 0.009, and 0.84, respectively [9]. Whereas the OSC of pure ceria typically ranges between 50 and 100 $\mu\text{mol O} \cdot g^{-1}$, optimized $Ce_xZr_{1-x}O_2$ formulations (specifically in the region of $0.6 < x < 0.8$) can achieve an OSC of approximately 185 $\mu\text{mol O} \cdot g^{-1}$ at temperatures as low as 377 °C[10].

1.2.2 Solid oxide fuel cells (SOFCs)

OSMs are an essential component of solid oxide fuel cells (SOFCs). A SOFC directly converts the chemical energy of a fuel into electrical power through a process of electrochemical oxidation. This technology is uniquely characterized by its all-solid-state construction, typically consisting of a dense, gas-tight electrolyte membrane sandwiched between two porous electodes: the anode (fuel electrode) and the cathode (air electrode) as shown in Figure 1.1. During operation, oxygen is reduced at the cathode to form oxide ions (O^{2-}) (Equation (1.7)). This oxygen reduction reaction (ORR) is a complex multi-step process that involves oxygen dissociation and charge transfer and is typically the rate-limiting step due to its slow kinetics [11]. The oxide ions migrate through the electrolyte to the fuel side. At the anode-electrolyte interface, these ions react with hydrogen fuel to produce water and release electrons. These electrons are subsequently transported through an external circuit, providing a flow of electrical current[12]. The chemical reactions at each electrode is as follows:

Cathode (Reduction): $$\frac{1}{2}O_2 + 2e^- \rightarrow O^{2-} \tag{1.5}$$

Anode (Oxidation): $$H_2 + O^{2-} \rightarrow H_2O + 2e^- \tag{1.6}$$

Overall Cell Reaction: $$H_2 + \frac{1}{2}O_2 \rightarrow H_2O \tag{1.7}$$

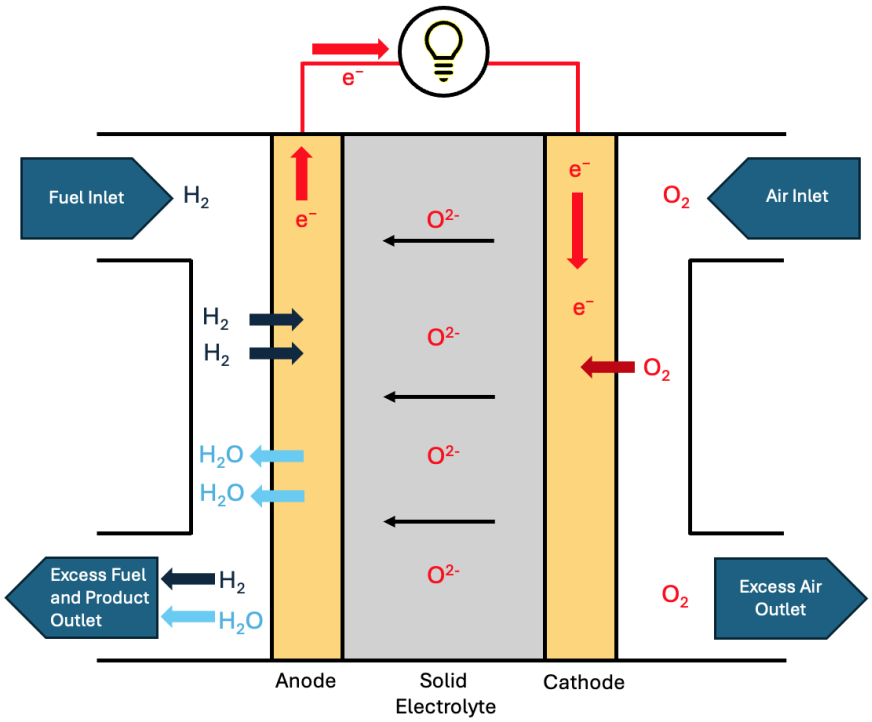


Figure 1.1: Solid oxide fuel cell.

For the cell to operate efficiently, the solid electrolyte must exhibit high ionic conductivity, typically in the range of 0.01 to 0.1 S cm^{-1}, while maintaining negligible electronic conductivity to prevent internal leakage currents. Furthermore, the electrolyte must remain chemically stable in both the highly reducing environment of the anode and the oxidizing environment of the cathode [13]. The state-of-the-art material for this application is 8 mol% yttria-stabilized zirconia (YSZ). The introduction of yttria serves to stabilize the zirconia in

its cubic fluorite phase at operating temperatures and creates a high concentration of oxygen vacancies within the lattice, thus leading to increased ionic conductivity[14]. However, YSZ generally requires high operating temperatures above 800 °C to achieve the necessary ionic conductivity, which can lead to accelerated material degradation and higher system costs.

To address the limitations of YSZ, ceria-based materials such as gadolinium-doped ceria (GDC), with the general formula $Ce_{1-x}Gd_xO_{2-\delta}$ have been widely adopted [13, 15]. GDC offers significantly higher ionic conductivity at lower temperatures, making it a promising candidate for intermediate-temperature SOFCs.

Beyond fluorite structures, cubic perovskite (ABO_3) materials are another important class of SOFC electrolyte materials such as strontium- and magnesium-doped lanthanum gallate, $La_{1-x}Sr_xGa_{1-y}Mg_yO_3$ (LSGM) [14, 16, 17]. In this system, partial substitution of La^{3+} by Sr^{2+} on the *A*-site and Ga^{3+} by Mg^{2+} on the *B*-site generates oxygen vacancies to maintain charge neutrality. These vacancies facilitate oxide-ion migration through the lattice. As a result, LSGM exhibits oxide-ion conductivity approximately an order of magnitude higher than that of YSZ at comparable temperatures and is capable of operating efficiently in the intermediate temperature range of 400 °C − 800 °C [16, 18]. Ongoing research efforts focus on addressing challenges related to phase stability, chemical compatibility with electrode materials, and further enhancement of ionic conductivity at lower operating temperatures.

1.2.3 Solar thermochemical water splitting (STWS)

OSMs can also be used for generating hydrogen, a cornerstone of the transition to clean energy. Currently, global hydrogen production is dominated by the steam-reforming of natural gas, accounting for over 45% of total supply, followed by oil reforming and coal gasification [19]. This process involves the catalytic conversion of hydrocarbons in

high-temperature steam (700 °C – 1000 °C) and high pressure (∼25 bar) to produce H_2, CO, and CO_2 [20, 21]. Taking methane as a representative hydrocarbon, the conversion occurs via steam-methane reforming (1.8)), which produces syngas (CO and H_2), followed by the water-gas shift reaction (1.9).

$$\mathrm{CH_4(g) + H_2O(g) \rightleftharpoons CO(g) + 3\,H_2(g)} \tag{1.8}$$

$$\mathrm{CO(g) + H_2O(g) \rightleftharpoons CO_2(g) + H_2(g)} \tag{1.9}$$

However, classifying this hydrogen as 'renewable' is challenging. Hydrogen is still drawn from fossil fuels and its production yields greenhouse gases as byproducts. This is known as *grey* or *blue hydrogen*.

As a way to preclude fossil fuel usage in H_2 production, electrolysis is an environmentally friendly process that splits water to produce hydrogen and oxygen without producing any greenhouse gas byproducts. This technique uses electricity to drive two half-cell reactions—the hydrogen evolution reaction (HER) and the oxygen evolution reaction (OER)—to split water [22]. The net reaction is as follows:

$$\mathrm{2\,H_2O(l) \longrightarrow 2\,H_2(g) + O_2(g)} \tag{1.10}$$

While water electrolysis represents an innovative approach due to its clean and renewable nature, the associated high electricity costs render the technique less practical for widespread application. Additionally, the production through electrolysis requires the use of electricity, which can still be linked to the combustion of fossil fuels. Another reason to produce H_2 electrolytically is to prevent the poisoning of hydrogen fuel cells via CO contaminants found in *grey/blue hydrogen* [23].

In 1972, Fujishima and Honda introduced an innovative approach known as photo-electrochemical (PEC) splitting [24], which lower the energy cost of hydrogen production. Here, they used a titanium oxide (TiO_2) electrode connected to a platinum black electrode through an external load. Upon irradiation of the TiO_2 surface, current flows from the platinum to the TiO_2 electrode, facilitating the oxidation and reduction reactions. Hydrogen produced either electrolytically or by PEC methods is considered *green hydrogen* if the energy input driving the water splitting is derived entirely from renewable energy sources.

An emerging field that utilizes sunlight more directly is solar thermochemical hydrogen production [25]. In solar-thermochemical water splitting (STWS), instead of using sunlight to generate charges in materials like titanium dioxide, sunlight is concentrated to raise the reaction temperature, employing this heat to drive the water-splitting process. STWS operates through a two-step cycle consisting of metal oxide reduction (1.11) and oxidation (1.12). The prime reaction is hydrogen evolution from water driven by the oxidization of metal oxide MeO_x. The second reaction is oxygen evolution from a fully oxidized metal oxide, MeO_{x+y}, where oxygen is released by the heat of concentrated solar radiation. The schematic of STWS is shown in Figure 1.2. The two coupled reactions are as follows:

$$\mathrm{MeO}_x\,(\mathrm{s}) + \mathrm{yH2O}\,(\mathrm{g}) \longrightarrow \mathrm{MeO}_{x+y}\,(\mathrm{s}) + \mathrm{yH}_2\,(\mathrm{g}) \tag{1.11}$$

$$\mathrm{MeO}_{x+y}\,(\mathrm{s}) \longrightarrow \mathrm{MeO}_x\,(\mathrm{s}) + \frac{\mathrm{y}}{2}\mathrm{O}_2\,(\mathrm{g}) \tag{1.12}$$

The STWS method offers notable advantages: The high cycle temperatures are compatible with concentrated solar energy; the system relies solely on water and heat; and the chemicals are recycled in a closed loop to produce pure *green hydrogen* [26].

Ceria is the benchmark material for STWS cycling, which uses the oxygen vacancy to transport oxygen and it was reported to produce $379\ \mu\mathrm{molH}_2 \cdot \mathrm{g}^{-1}$ when reduced at 1500 °C and oxidized at 800 °C [27, 28]. While higher reduction temperatures correlate with

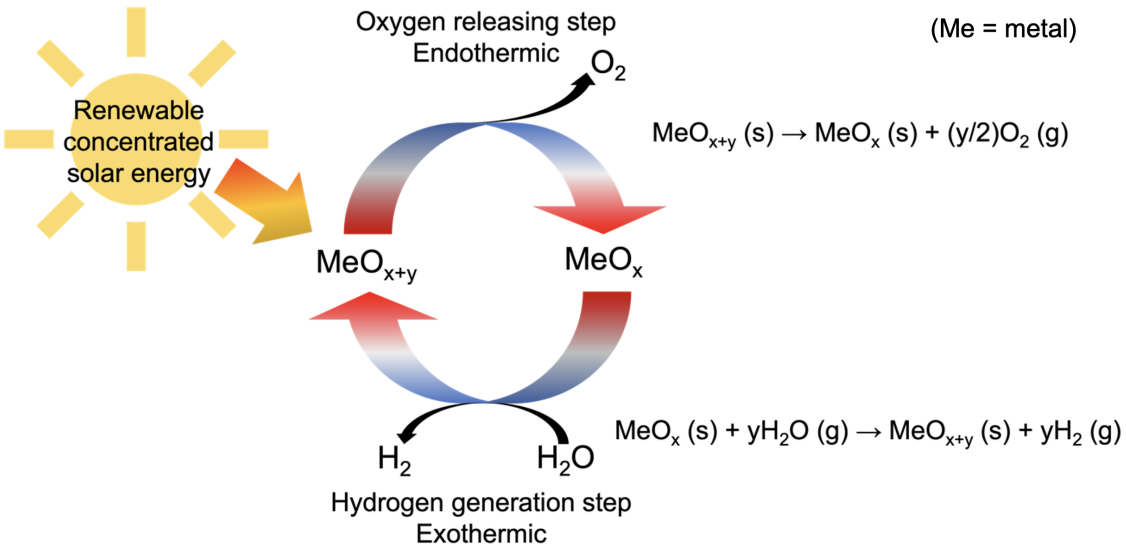


Figure 1.2: Solar thermochemical water splitting (STWS).

increased H_2 generation, the extreme thermal requirements of ceria remain a significant challenge. Consequently, perovskite-type materials such as $BaCe_xMn_{1-x}O_3$ (BCM) [25] or $La_xSr_{1-x}Mn_yAl_{1-y}O_3$ (SLMA) [29] have been investigated for their ability to produce hydrogen at lower reduction temperatures ($\sim$1350 °C). Nevertheless, despite their enhanced performance, these materials still face challenges in meeting the efficiency, stability, and scalability requirements necessary for practical solar thermochemical hydrogen production.

1.2.4 Limitations of current oxygen storage materials

Despite the extensive study of materials for these applications, several major challenges remain. The key challenge is the trade-off between thermodynamics and kinetics. While the primary goal is to have a fast oxygen redox cycle, this often conflicts with the high-temperature conditions required for high storage capacity. In the case of solid oxide fuel cells, the high temperatures currently used for YSZ (around 800 °C) are problems leading to secondary effects, such as the coarsening of microstructures, the segregation of dopants

at the surface, and unwanted reaction with other electrode materials [30]. If an alternative material is used to operate at a lower temperature, there is usually a significant drop in conductivity. Therefore, finding materials that can maintain high conductivity at lower temperatures is essential.

Solar thermochemical water splitting (STWS) is also currently limited by low overall energy efficiency. The highest reported efficiencies reported for the benchmark material, ceria is only about 5% when the minimum solar-to-fuel efficiency required for commercial use is approximately 20% [31]. This large efficiency gap is a major barrier to using this technology on a large scale. Another critical challenge arises from the high operating temperatures required to reduce the material. These elevated temperatures increase heat losses and make it harder to design reactor and choose system materials. Additionally, these redox materials must maintain structural and chemical stability over repeated cycles. Long term exposure to high heat cause microstructural degradation of the material [32]. Therefore, it is necessary to develope materials that exhibit high fuel production yields and fast reaction rates at lower operating temperatures for the practical employment of STWS technologies [32].

1.3 AB_2O_4 compounds

While the fluorite and perovskite metal oxides discussed earlier facilitate oxygen incorporation through vacancy formation, this thesis introduces a distinct class of materials: hexagonal AB_2O_4-type compounds. Instead of relying on vacancy formation, these materials undergo a reversible phase transition to accommodate oxygen.

The hexagonal AB_2O_4 family, characterized by an A-site rare-earth element and a mixed-valent B-site transition metal, has garnered significant interest due to its unique structural and physical phenomena. Historically, these compounds have been reported to crystallize in the

rhombohedral $R\bar{3}m$ space group with an alternating stack of octahedrally coordinated rare-earth metal layers and transition metal double-bipyramidal layers [33–38]. The structure is particularly distinctive because the trigonal bipyramidal coordination environment is relatively rare in solid-state oxides. Within this family, the rare-earth ferrites (RFe_2O_4) [39–41] are particularly notable for their multiferroic properties, which describes exhibiting simultaneous magnetic and ferroelectric properties [42]. Unlike traditional ferroelectrics where polarization stems from ionic displacement, ferroelectricity in RFe_2O_4 originates from a polar arrangement of electrons. Specifically the charge frustration of Fe^{2+} and Fe^{3+} ions in the triangular lattice creates such polar ordering [40, 41, 43]. M. A. Subramanian provided a comprehensive review of these materials, studying the relationship of their structural symmetry and magnetic ground states [44].

While initial research was limited to electronic and magnetic properties, the discovery of oxygen storage properties in 2014 by Hervieu et al. opened an entirely new avenue for studying these materials [45, 46]. They demonstrated that $LuFe_2O_4$ could undergo oxygen intercalation at approximately 200 °C, a remarkably low temperature compared to conventional fluorite- or perovskite-type oxygen storage materials. Structural analysis revealed that additional oxygen atoms can be topotactically intercalated into the Fe-O_5 layers, reaching a maximum stoichiometry of $LuFe_2O_{4.5}$ [45–47]. This ability to undergo reversible phase transitions while maintaining the primary structural framework makes these systems highly promising candidates for low-temperature oxygen storage and catalytic applications.

Building upon these findings, our research group at University of Maryland has systematically explored the *A*-site and *B*-site substitutions to tune these redox properties [48–50]. Previous work by R. Jayathilake et al. examined the *A*-site substituted AFe_2O_4 series (*A* = Lu, Yb, Y) and confirmed they all had similar oxygen storage behavior similar to the previously reported $LuFe_2O_4$ compound [48]. T. Li et al. explored substituting Mn^{2+} for

Fe^{2+} into the redox active *B* site in $YbFe_2O_4$, and explored the phase transition behavior and their lattice expansion linking it with the crystal field theory [49]. In my previous work, to further investigate the effects of *B*-site substitution on structure and redox behavior, we substituted Ga^{3+} for Fe^{3+} to form $LuMnGaO_4$ [51]. The greater disparity in size and chemical properties between Mn and Ga, compared to Mn and Fe, provided an opportunity to investigate the impact of elemental substitution on structural and redox characteristics.

1.4 Outline of the thesis

This dissertation provides a comprehensive understanding of AB_2O_4 as oxygen storage materials, from fundamental structural characterization to structure-property relationships. The goal is to systematically unravel the relationship between chemical composition, structural stability, and redox performance. To achieve this, I utilized neutron and X-ray diffraction, in-situ synchrotron X-ray studies, and thermogravimetric analysis to characterize these materials under various conditions.

Chapter 2 describes the experimental techniques used in this research, including synthesis, basic principles of instrumentation and analysis methods. Specific parameters for individual experiments are further elaborated in the introductory sections of their respective chapters.

Chapter 3 presents the deep-dive investigation into $LuMnGaO_4$ serving as a model system for the *B*-site substituted series. Using a combination of neutron and synchrotron X-ray diffraction alongside thermogravimetric analysis, I conduct a thorough characterization of the structural evolution from the reduced to the oxidized phase. Beyond the structural study, this chapter explores a distinct, reversible colorimetric transition, wherein the material shifts from a greyish green to black upon oxygen uptake. Using UV-Vis diffuse reflectance spectroscopy with structural data, I correlate these optical changes with the underlying

modifications in the transition metal coordination environment and electronic oxidation states.

Chapter 4 expands the scope to the AMnGaO$_4$ series, where the A-site is varied (A = Lu, Yb, In). Using synchrotron X-ray diffraction, I demonstrate that while these analogues share the same initial space group and symmetry in their reduced phases, the In analogue exhibits distinct behavior. This chapter explores how the specific chemical nature of the A-site cation influences the topotactic transition and oxygen intercalation capacity.

Chapter 5 presents a systematic investigation into the effects of A- and B-site substitution on the structural evolution and oxygen storage behavior of $AB_2O_{4+\delta}$ (A = Lu, Yb, Er, Y; B = Mn, Fe, Ga) compounds. This chapter explores how the ionic radius of the A-site cation dictates oxygen storage capacity and examines the role of B-site cations in driving the structural response to oxidation.

Chapter 2: Methodology

2.1 Solid State Synthesis

The AB_2O_4 oxide materials investigated in this work were synthesized using a conventional solid-state reaction method. Solid-state synthesis involves the formation of polycrystalline materials through reactions between solid precursors, without the involvement of liquid or gas phases. Reaction parameters such as temperature, particle size, and the surface area of the reactants play critical roles in determining the kinetics of the reaction and purity of the product.

A typical solid-state reaction consists of three main steps: grinding, pelletizing, and high-temperature sintering. Initially, stoichiometric amounts of the precursor powders are thoroughly ground using a mortar and pestle to reduce particle size and increase surface area, thereby enhancing reactivity. Alternatively, ball milling may be employed for more efficient and uniform grinding; this technique utilizes a milling apparatus with grinding balls to achieve fine particle sizes and improved mixing.

The homogenized powder mixture is subsequently pressed into pellets using a hydraulic pellet press. Pelletization improves physical contact between reactant particles by increasing surface area of the reactants and provides a more uniform and reproducible packing density compared to loose powders. The pellets are then subjected to high-temperature sintering to facilitate the solid-state reaction.

The AB_2O_4 compounds investigated in this study were synthesized by first grinding the

stoichiometric amounts of precursors using a mortar and pestle. The resulting mixture was pressed into 13 mm diameter pellets. The pellets were placed in a 2 mL alumina crucible, which was then inserted into a 16 mm (OD) quartz ampoule. The alumina crucible served as a protective liner to prevent the reagents from reacting with the quartz at high temperatures. This setup also acted as a barrier against oxygen diffusing from the quartz into the sample. The quartz ampoule was then evacuated and sealed under vacuum, which is an essential step to prevent the reagent oxidizing before forming the desired product. This sealed ampoule was sintered at approximately 1200 °C for 12 hours in a high-temperature tube or box furnace, followed by rapid quenching in an ice bath. During sintering, new phase is formed through solid-state diffusion, in which atoms and ions migrate across phase boundaries, ultimately resulting in the formation of the desired compound[52].

2.2 Diffraction Techniques

2.2.1 Crystalline Materials

The work presented in this thesis focuses exclusively on the solid state materials, which can be further categorized into amorphous or crystalline structures based on their atomic arrangement. Amorphous solids have an irregular pattern of ions, molecules, or atoms in a solid, while crystalline has a regular and repeating arrangement of components in a solid (Figure 2.1).

Historically, a solid was first defined as a crystal if its atoms, ions, and/or molecules form a long-range ordered arrangement. This definition changed a century later with the advent of X-ray diffraction. After the discovery of quasicrystals, the International Union of Crystallography (IUCr) officially broadened the definition in 1992. Today, a crystalline solid is formally defined as any material that produces a sharp diffraction pattern, where the majority of the intensity is concentrated into sharp Bragg peaks, distinguishing it from the

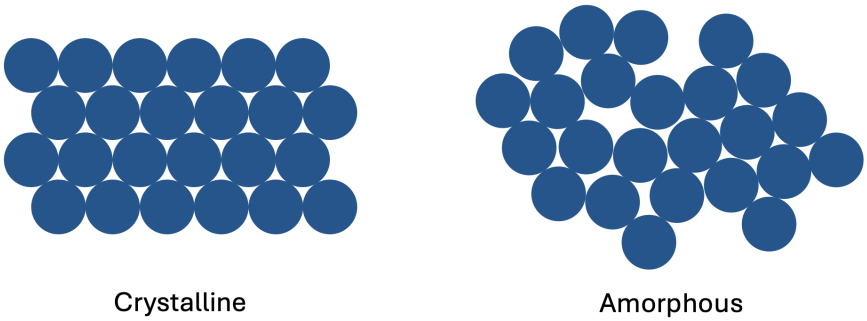


Figure 2.1: Structural representation of solid states.

diffuse scattering peaks [53]. I will dive more into X-ray diffraction in following sections.

A crystal's periodic structure can be described by a lattice, which consists of an infinite array of repeating elementary parallelepipeds extending in three dimensions. Each of these repeating units is called a unit cell. The arrangement and symmetry of atoms within a single unit cell fully define the structure of the entire crystal[54]. A unit cell is characterized by six paraameters: a, b, c, α, β, and γ. The parameters a, b, and c represent the lengths of the unit cell edges, while α, β, and and γ are the angles between b and c, c and a, and a and b, respectively (Figure 2.2).

Lattice planes, also called crystallographic planes, are used to describe the diffraction phenomenon in ideal crystal lattices. A family of crystallographic planes is defined as a set of parallel planes that intersect the lattice in a regular and periodic manner. These planes are equally spaced, and the distance between adjacent planes is called the interplanar spacing or d-spacing. Each family of planes is identified by three indices, h, k, and l, and is denoted as (h, k, l), known as Miller indices. Figure 2.2 shows three planes in a lattice as examples.

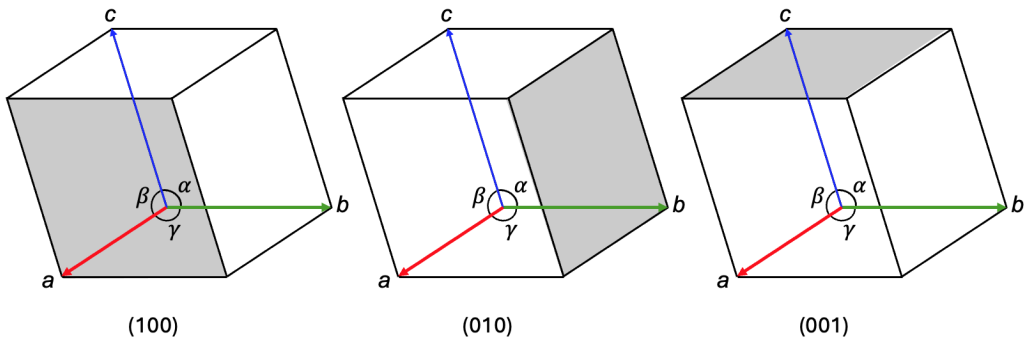


Figure 2.2: Unit cell showing (100), (010), and (001) planes.

2.2.2 X-ray Diffraction

The diffraction of X-rays by crystals was discovered by Max von Laue in 1912, who provided the first experimental proof that X-rays behave as waves as well as particles. Following the ground breaking discovery, William Henry Bragg and William Lawrence Bragg, father and son, developed a key insight that the diffraction is due to the "reflection" of X-rays from parallel planes. They provided a more intuitive explanation for the observed diffraction patterns. They considered an incident X-ray beam with a wavelength of λ hitting parallel crystal planes P_1 and P_2 with an angle θ with an interplanar spacing d (Figure 2.3). When referring to a specific set of planes defined by Miller indices (h, k, l) as mentioned in the previous section, this interplanar spacing d is more specifically denoted as d_{hkl}.

The oscillating electromagnetic field of the incident beam induces vibrations in the electrons located at points O and C in Figure 2.3, causing them to radiate in all directions. A diffracted beam of maximum intensity is produced in the specific direction where the secondary rays, $1'$ and $2'$, emerge at an angle θ. This occurs when the rays appear to be reflected from the planes and are perfectly in phase, leading to constructive interference. When we drop perpendicular lines from O to rays 2 and $2'$, it is evident that $\angle AOC = \angle BOC = \theta$. It follows that $AC = BC$, and waves in ray $2'$ is in phase with ray $1'$ if the path difference

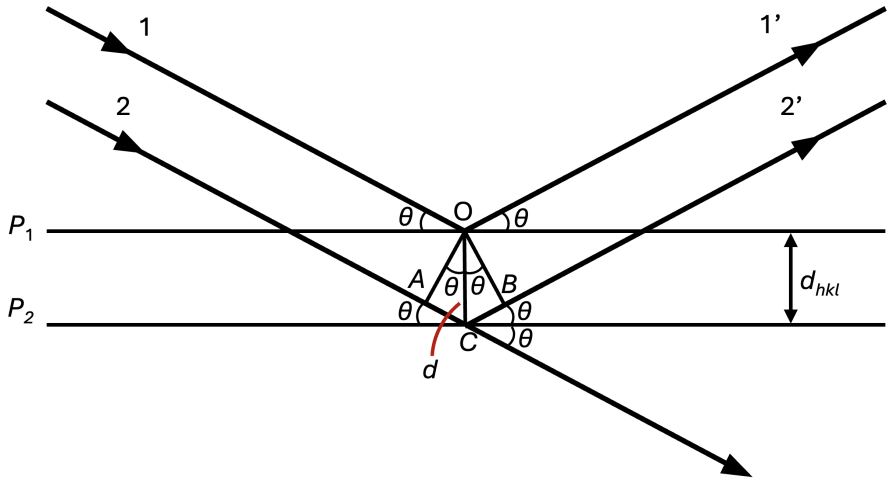


Figure 2.3: Schematic illustration of X-ray diffraction from parallel crystal planes P_1 and P_2. Incident rays (1, 2) are scattered at an angle θ, producing outgoing rays ($1'$, $2'$).

$AC + CB$ (= $2AC$) is an integral multiple of the wavelength λ, expressed as the following equality, where n is an integer.

$$2AC = n\lambda \tag{2.1}$$

By definition, $AC/d \equiv sin\theta$, and by substituting in Eq. (2.2)

$$2dsin\theta = n\lambda \tag{2.2}$$

This equation is called Bragg's law.

In practice, an X-ray beam incident upon a crystalline sample scatters off the periodically arranged atoms, creating a diffraction pattern unique to the material's internal structure. For the metal oxide powders analyzed in this study, X-ray powder diffraction was employed by scanning the sample through a range of 2θ angles. This technique ensures that all possible diffraction directions are attained due to the random orientation of the powdered particles. The resulting peaks are then converted to d-spacings, which serve as a unique 'fingerprint' for material identification because every crytalline substance possesses a unique set of lattice

planes.

The X-ray diffraction (XRD) data presented in this work were obtained using both laboratory-based and synchrotron radiation sources:

- Laboratory Diffractometers:
  - Bruker D8 Advance X-ray Crystallographic Center, University of Maryland; Cu $K\alpha$ radiation source
  - Anton Paar XRDynamic 500; Cu $K\alpha$ radiation source
- High-resolution Synchrotron X-ray Powder Diffraction:
  - Beamline I11, Diamond Light Source (UK); $\lambda = 0.8241$ Å[55]
  - Beamline 11-BM, Advanced Photon Source (APS), Argonne National Laboratory; $\lambda = 0.457895$ Å
  - Beamline 11-ID-C, Advanced Photon Source (APS), Argonne National Laboratory; $\lambda = 0.1173$ Å
  - Beamline 28-ID-2, National Synchrotron Light Source II (NSLS-II), Brookhaven National Laboratory; $\lambda = 0.1824$ Å

In a standard laboratory XRD, X-rays are produced via an X-ray tube, where a copper (Cu) target is bombarded with high-energy electrons to generate X-rays with a wavelength of 1.5406 Å. In contrast, synchrotron light sources generate X-rays using massive particle accelerators. Electrons are accelerated to near the speed of light and circulate within a storage ring. As they are deflected along curved paths, they emit highly intense and tunable X-ray radiation. The intensity of synchrotron beam is orders of magnitudes brighter than that of laboratory X-rays.

2.2.3 Neutron Diffraction

Neutron diffraction is another crucial technique used in this research to determine the crystal structures of metal oxide materials. The wave-particle duality of neutrons allow them to diffract off periodically arranged atoms in crystalline solids. However, unlike X-ray diffraction, neutrons interact primarily with the atomic nuclei rather than with the surrounding electron cloud. Thermal neutrons, characterized by wavelengths on the order of atomic dimensions (approximately $1–2 \times 10^{-10}$ m), diffract strongly from the periodic atomic arrangements in crystalline materials in a matter analogous to X-rays[56]. Since this interaction is independent of the atomic number Z, neutron diffraction is particularly effective for locating light elements, such as oxygen, within heavy metal oxide lattice. Differences in neutron scattering lengths can enable the distinction between elements with similar atomic numbers. Consequently, neutron diffraction serves as a powerful and complementary technique to X-ray diffraction.

While neutrons do not have a charge and are electrically neutral, they carry an intrinsic magnetic spin that allows them to interact directly with the magnetic moments of a material. These moments typically arise from the unpaired electrons within the atomic electron cloud. Therefore, neutron diffraction can resolve the microscopic magnetic structure of a material[57].

For this research, Time-of-flight (TOF) neutron diffraction experiments were conducted on the POWGEN beamline at the Spallation Neutron Source, Oak Ridge National Laboratory. [58]

2.2.4 Powder Diffraction Analysis

2.2.4.1 Rietveld Analysis

Rietveld refinement was performed on XRD and neutron diffraction patterns using GSASii [59] and TOPAS [60] software. Rietveld analysis [61, 62] is a method used to extract crystallographic information by performing a least-squares refinement of a theoretical model, fitting the calculated profile to the experimental diffraction pattern through the adjustment of structural and instrumental parameters. The parameters being refined include atomic position, thermal, and site-occupancy parameters as well as background, lattice, instrumental parameters [63]. The quantity being minimized by the least-squares approach is the residual, S_y, which can be expressed in the following equation.

$$S_y = \sum_i w_i (y_i - y_{ci})^2 \tag{2.3}$$

w_i $= 1/y_i$

y_i observed (gross) intensity at the ith step

y_{ci} calculated intensity at the ith step

A powder diffraction pattern of a material can be viewed as a collection of individual reflection profiles. Each profile is characterized by its peak height, position, width, and decaying tails. The integrated area under the peak is proportional to the Bragg intensity, I_K, where K represents the Miller indices, h, k, l. This intensity is directly proportional to the square of the absolute value of the structure factor, $|F_K|^2$, where the structure factor, F_K, represents the amplitude and phase of the scattered wave. Most systems have peaks with overlapping Bragg reflections and they contribute to the peak intensity, y_i, at an arbitrary point, i. The calculated intensity y_{ci} is calculated by the sum of the square of the structure

factor at the overlapping Bragg reflections with consideration of other factors, such as Lorenz-polarization, multiplicity factors, preferred orientation function, and background intensity[63]. Each calculated intensity is based on the following equation:

$$y_{ci} = s\sum_{K} L_K |F_K|^2 \phi(2\theta_i - 2\theta_K) P_K A + y_{bi} \tag{2.4}$$

- s scale factor
- K Miller indices, hkl, for a Bragg reflection
- L_K Lorentz-polarization, and multiplicity factors
- ϕ reflection profile function
- P_K preferred orientation function
- A absorption factor
- F_K structure factor for the Kth Bragg reflection
- y_{bi} background intensity at the ith step

Rietveld method uses the full pattern including all available intensity data instead of using only strong intensity peaks as the traditional integrated intensity methods[64]. The traditional approach was based on individual peaks and its integrated intensities which made it challenging because it could not resolve the overlapping peak problem. Through the iterative minimization of the difference between the calculated and observed diffraction patterns, key structural data including lattice parameters, atomic coordinates, site occupancy, and thermal parameters of the sample can be obtained.

2.2.4.2 Le Bail analysis

Le Bail analysis is similar to the Rietveld analysis in that it is a form of whole pattern fitting, but it does not require a detailed atomic structural model. Instead, only profile-related

parameters are refined, including unit cell parameters, background, instrumental zero error, peak-width, and other peak shape parameters; atomic positions are not needed for this refinement[65].

In practice, Le Bail refinement is normally performed prior to Rietveld refinement to obtain accurate lattice parameters and well-defined peak shape parameters. These refined values can then be fixed or used as starting parameters in the subsequent Rietveld refinement, where intensity-related parameters, such as atomic positions, site occupancies, and thermal parameters are refined. When the primary goal is to determine unit cell paramters and crystallite size or strain information, Le Bail refinement is sufficient.

2.3 Thermogravimetric Analysis

Thermogravimetric analysis (TGA) is a high-precision analytical technique used to characterize the physical and chemical properties of materials by monitoring the mass as a function of temperature. The instrument is equipped with an ultrasensitive microbalance capable of detecting mass changes on the order of micrograms, coupled with a temperature controlled furnace. Measurements can be performed under different atmospheric conditions, such as inert gas or air, depending on the experimental objectives. As the furnace temperature is increased at a controlled rate, materials may undergo decomposition, dehydration, or oxidation, which are reflected in corresponding mass changes. In this study, the metal oxide AB_2O_4 samples were analyzed under an air atmosphere in order to monitor their mass variations associated with oxygen uptake from the surrounding environment. To confirm the oxygen storage reversibility, the metal oxides in their oxidized phases ($AB_2O_{4.5}$) were heated under hydrogen gas. The instruments used in this research are Mettler Toledo TGA/DSC 2 HT 1600 and TA Instruments Discovery TGA-5500.

2.4 Electron Microscopy

Electron microscopy (EM) is a high resolution imaging technique that uses high energy electron beams to create ultra-high-resolution images from micro to atomic scale. This technique relies on the interaction of an accelerated electron beam with a sample to generate various signals. Depending on whether these electrons are transmitted through or scattered from the surface, the technique is categorized into Transmission Electron Microscopy (TEM) or Scanning Electron Microscopy (SEM), respectively.

2.4.1 Transmission Electron Microscopy

In Transmission Electron Microscopy (TEM), an accelerated beam of electrons is transmitted through a thin sample (typically < 100 nm) fixed on a support grid. The resulting image is formed by the interaction of electrons as they pass through the sample; the local density and atomic weight within the sample determine the degree of electron scattering, creating contrast between electron-dense and electron-sparse regions. For the purposes of this research, TEM was primarily utilized for electron diffraction (ED), which is generated by elastically scattered electrons. Because crystalline samples cause the electrons to diffract according to Bragg's Law, the resulting diffraction patterns provide a direct reciprocal space map of the crystal lattice. These patterns were used to analyze the modulated structure of the synthesized phase, allowing for the precise identification of symmetry and unit cell parameters. The instrument used for this research was JEOL 2100F field emission gun (scanning) TEM [FEG-(S)TEM], operated at an accelerating voltage of 200 kV at the AimLab at the University of Maryland.

2.4.2 Scanning Electron Microscopy

In Scanning Electron Microscopy (SEM), the images are primary generated through the detection of secondary electrons and backscattered electrons, produced by the interaction between the accelerated electron beam and the sample surface. The secondary electron detector captures the low-energy secondary electrons from the uppermost layer of the surface, providing high resolution data on surface topography and morphology. The backscattered electron detector measures high-energy electrons that are elastically scattered during interactions with the atomic nuclei of the elements in the sample. The number of backscattered electrons depend on the size of the atom nuclei which creates contrast of the images.

Energy Dispersive X-ray Spectroscopy (EDX) is normally coupled with an SEM. It is employed to detect characteristic X-rays emitted when the electron beam hits the sample. As these X-ray energies are unique to specific atomic transitions, they allow for precise elemental identification. In this study, EDX was utilized to verify the successful synthesis of the target compound by quantifying elemental ratios and confirming agreement with the expected stoichiometry. The chemical composition of the materials studied in Chapter 3 was analyzed using Hitachi SU-70 Schottky FEG-SEM equipped with the Bruker energy dispersive X-ray spectroscopy (EDS, XFlash(6/60).

2.5 UV-vis Diffuse Reflectance Spectroscopy

UV-vis Diffuse Reflectance Spectroscopy (UV-vis DRS) uses light from both ultraviolet and visible regions of the electromagnetic spectrum , typically ranging from 200 nm to 800 nm, to study the optical properties of solid samples. While traditional UV-vis spectroscopy relies on light transmitted through a liquid, DRS is designed for solids, especially those in powder form. When light hits a powder, it does not reflect at a single mirror-like angle;

instead, the various orientations of the crystal lattices cause the light to scatter in every direction. This phenomenon is known as diffuse reflectance. To capture this scattered light accurately, the instrument uses an integrating sphere, a hollow, highly reflective chamber that collects light from all angles and reflects it toward a detector to measure the total intensity.

The data collected by the detector is expressed as reflectance (R). This value is transformed into a value $F(R)$ that is proportional to the sample's absorption by the Kubelka-Munk (K-M) function. The formula is expressed as

$$F(R) = \frac{(1-R)^2}{2R} = \frac{k}{s} \tag{2.5}$$

where k is the absorption coefficient and s is the scattering coefficient. By obtaining the absorption coefficient, the wavelengths of light the material absorbs most strongly can be determined. In this work, UV-vis Diffuse Reflectance Spectroscopy was used to verify the color transition of $LuMnGaO_4$ from green to black as it oxidized. The instrument used in Chapter 3 of this dissertation was Shimadzu UV3600 UV-vis-NIR spectrometer equipped with an integrating sphere attachment. The recorded reflectance spectra were processed into pseudo-absorbance using the Kubelka-Munk transformation.

2.6 Superconducting Quantum Interference Device (SQUID)

SQUID magnetometry was used to analyze the magnetic properties of several compounds investigated in this work. It is a magnetometer that measures low magnetic fields as small as 10^{-14}–10^{-15} Tesla. The operating principle of SQUID relies on the fundamental phenomena of superconductivity, flux quantization, and the Josephson effect. The device consists of a superconducting loop interrupted by two parallel Josephson junctions. When an external magnetic flux penetrates the loop, it modulates the quantum phase of the circulating Cooper

pairs. This interaction causes the SQUID's critical current and resultant voltage to oscillate periodically as a function of the magnetic flux quantum (Φ_0), expressed in Eq.(2.6).

$$\Phi_0 = \frac{h}{2e} \approx 2.068 \times 10^{-15}\ \mathrm{T \cdot m^2} \tag{2.6}$$

h is Planck's constant and e is the elementary charge; the factor of $2e$ represents the paired nature of superconducting charge carriers (Cooper pairs).

In Chapter 4, magnetic susceptibility was analyzed as a function of temperature and field using a 7 T SQUID magnetometer (MPMS3) at the Maryland Quantum Materials Center at the University of Maryland. Measurements were performed at 100 Oe and 1000 Oe, employing both zero-field-cooled (ZFC) and field-cooled (FC) cycles between 2 K and 300 K to capture the material's direct current (DC) magnetization behavior.

Chapter 3: Reversible Structural and Colorimetric Transitions in $LuMnGaO_4$ upon Oxygen Uptake and Release

Note: The content of this chapter is adapted from "Reversible Structural and Colorimetric Transitions in $LuMnGaO_4$ upon Oxygen Uptake and Release," published in *Dalton Transactions* (`https://doi.org/10.1039/d5dt00798d`). I was responsible for the synthesis, neutron diffraction studies, and TGA measurements, as well as the preparation of the manuscript. Dr. Tianyu Li conducted the UV-vis spectroscopy and in-situ sequential refinements. TEM electron diffraction was performed and the data was analyzed with the assistance of Dr. Sz-Chian Liou.

3.1 Introduction

Recent advancements have broadened the scope of oxygen carrier materials beyond traditional binary metal oxides and perovskite-related oxides to include hexagonal layered $AB^{2+}B^{3+}O_4$-type compounds (A = rare earth metals; B = transitional metals) [33–36, 38]. These materials, characterized by a trigonal structure of alternating octahedrally coordinated rare earth metal layers and transition metal double bipyramidal layers, were initially recognized for their multiferroic properties [45]. $LuFe_2O_4$ was the first $AB^{2+}B^{3+}O_4$ compound reported to reversibly uptake oxygen at 200 °C, which is a relatively low temperature compared to previously known oxides, forming $LuFe_2O_{4+x}$ and reverting to its reduced phase [45, 46]. Following this discovery, various A-site and B-site substituted compounds

demonstrated similar oxygen storage capacities at temperatures around 250-300 °C in our previous work [48–50, 66]. In $LuMnFeO_4$, redox-active Mn^{2+} was substituted for Fe^{2+}, while Fe^{3+} occupied the redox-inactive site. This compound exhibited similar redox behavior to $LuFe_2O_4$, undergoing a phase transition from Rm to P symmetry during oxygen absorption, forming $LuMnFeO_{4.5}$ [50]. To further investigate the effects of *B*-site substitution on structure and redox behavior, we substituted Ga^{3+} for Fe^{3+} to form $LuMnGaO_4$. The greater disparity in size and chemical properties between Mn and Ga, compared to Mn and Fe provided an opportunity to investigate the impact of elemental substitution on structural and redox characteristics.

In addition to oxygen storage, oxygen sensors play a critical role in modern technologies, with applications spanning food production, automotive systems, healthcare, and environmental monitoring [67–69]. These sensors, categorized by mechanisms such as electrochemical, resistive, and optical methods, are designed to monitor oxygen levels accurately [70–72]. Developing materials that not only store oxygen but also enable real-time sensing of oxygen capacity offers exciting opportunities for advancing sensor technologies. Such multifunctional materials could revolutionize oxygen monitoring by integrating storage and sensing capabilities into a single platform.

In this study, we present a comprehensive investigation of $LuMnGaO_4$ and its oxidized phase, utilizing neutron and synchrotron X-ray powder diffraction (SXPD). In-situ SXPD revealed phase transitions and structural modulations in the oxidized phase. Notably, $LuMnGaO_4$ displayed a color change from greenish-grey to black upon oxidation, a phenomenon not observed in previously studied $LnFe_2O_4$ and $LnMnFeO_4$ compounds. We establish a correlation between this color transition and the changes in the oxygen environment surrounding Mn due to structural evolution during oxidation. This distinct color change suggests potential applications for $LuMnGaO_4$ not only in oxygen transport but also in oxygen sensing, highlighting its potential as a bifunctional material.

3.2 Experimental

3.2.1 Materials Synthesis

The reduced phase, $LuMnGaO_4$, was synthesized via solid-state reactions. Stoichiometric amounts of Lu_2O_3 (99.999 %), MnO (99 %), and Ga_2O_3 (99.999 %) were ground to produce 2 g of the target compound. The powder mixture was pressed into 13 mm diameter pellets, placed in a 2 mL alumina crucible, and sealed inside an evacuated 8 mm diameter quartz ampoule. The ampoule was heated to 1180 °C at a ramp rate of 5 °C/min, held at this temperature for 24 hours, and then rapidly quenched in an ice-water bath to preserve the metastable $LuMnGaO_4$ phase and prevent the formation of oxide impurities. The oxidized phase, $LuMnGaO_{4.5}$, was prepared by heating $LuMnGaO_4$ at 600 °C in ambient air for 12 hours, followed by a natural cooling to room temperature.

3.2.2 Thermogravimetric Analysis (TGA)

TGA was conducted on the reduced phase, $LuMnGaO_4$, using a Mettler Toledo TGA/DSC 2 HT 1600. Approximately 5 mg of the sample was heated in air to 700 °C with a ramp rate of 10 °C/min. For reduction studies, 10 mg of the oxidized phase was heated to 800 °C in 3% H_2/Ar.

3.2.3 X-ray photoelectron spectroscopy (XPS)

XPS data were collected using a Kratos AXIS Supra+ X-ray photoelectron spectrometer equipped with a monochromatic Al Kα X-ray source (1486.6 eV, 225 W). The base pressure of the analysis chamber was $\sim 1 \times 10^{-9}$ torr. Spectra were acquired in hybrid lens mode with slot collimation and a spot size of 700 μm $\times$ 300 μm. The pass energy and step sizes were set to 160 eV and 0.5 eV for survey spectra, and 20 eV and 0.1 eV for high-resolution

spectra, respectively. Samples were grounded during analysis, and charging effects were minimized using a charge neutralizer. Instrument calibration was performed using Au $4f_{7/2}$ (84.0 eV) and Cu $2p_{3/2}$ (932.6 eV) peaks from sputter-cleaned metal foils.

Data calibration involved aligning the adventitious C 1s peak to 284.8 eV. Deconvolution was performed using a Voigt peak profile (70% Gaussian, 30% Lorentzian) after Shirley background subtraction. For Ga and Lu quantification, the Ga $3p_{3/2}$ and Lu $4p_{3/2}$ peaks were used, with sensitivity factors adjusted based on spin-orbit splitting ratios of p orbitals. All data were analyzed using CasaXPS software.

3.2.4 Electron paramagnetic resonance (EPR)

EPR measurements were carried out by Dr. Tianyu Li at the University of California, Santa Barbara, using a Bruker EMXPlus X-band spectrometer equipped with a high-sensitivity Bruker ER 4199HS-LC resonator. Spectral acquisition involved averaging three scans over a field sweep of 0 mT to 600 mT, with a magnetic field modulation of 100 kHz and a modulation amplitude of 0.4 mT. Data processing and spectral fitting were performed using the EasySpin toolbox. Standard (non-operando) measurements were conducted at a microwave power of 2 mW.

3.2.5 High-resolution synchrotron X-ray and neutron diffraction

High-resolution synchrotron X-ray powder diffraction (SXPD) was performed to characterize the crystal structures of $LuMnGaO_4$ and $LuMnGaO_{4.5}$. Measurements were conducted at the Advanced Photon Source (APS), Argonne National Laboratory, on the 11-BM beamline using X-rays with a wavelength of 0.457895 Å. Data were collected at room temperature (300 K). Time-of-flight (TOF) neutron diffraction experiments were conducted on the POWGEN beamline at the Spallation Neutron Source, Oak Ridge National Laboratory,

with data acquired at 300 K. Structural analysis was performed using Rietveld refinement with the GSAS-II software.

For in-situ SXPD studies, data were collected on the APS 11-ID-C beamline using a high-temperature furnace. A wavelength of 0.1173 Å was used, covering a Q-range of ~ 0.6 $Å^{-1}$ to 11 $Å^{-1}$. The sample was heated at a controlled ramp rate of 10 °C/min in flowing air, diffraction patterns continuously recorded during heating to monitor the real-time structural evolution of $LuMnGaO_4$.

3.2.6 Transmission Electron Microscopy (TEM)

Transmission electron microscopy (TEM) and selected area electron diffraction (SAED) patterns were acquired using a JEOL 2100F field emission gun (scanning) TEM [FEG-(S)TEM] and operated at an accelerating voltage of 200 kV. These measurements were carried out with the assistance of Dr. Sz-Chian Liou at the Aim Lab at the University of Maryland Nanocenter.

3.2.7 UV-Vis Reflectance Spectroscopy

Diffuse reflectance spectra of the powder samples were obtained using a Shimadzu UV3600 UV-vis-NIR spectrometer equipped with an integrating sphere attachment. Prior to measurement, the powders were diluted with $BaSO_4$ in a 1:4 volume ratio and packed into solid sample holders. The recorded reflectance spectra were processed into pseudo-absorbance using the Kubelka-Munk transformation. This measurement was performed by Dr. Tianyu Li.

3.2.8 Energy Dispersive X-ray Spectroscopy (EDS)

The chemical composition of the reduced and oxidized phases was analyzed on powder samples using Hitachi SU-70 Schottky FEG-SEM equipped with the Bruker energy dispersive X-ray spectroscopy (EDS, XFlash(6/60).

3.3 Results and Discussion

3.3.1 Reversible oxgyen uptake of $LuMnGaO_4$

Previous studies have demonstrated that $Ln Fe_2O_4$ [45, 48] and $Ln FeMnO_4$ [50] (*Ln* = lanthanides) compounds can uptake oxygen at elevated temperatures, leading to the oxidation of Fe^{2+} to Fe^{3+} $Ln Fe_2O_4$ or Mn^{2+} to Mn^{3+} ($Ln FeMnO_4$) and the formation of final products $Ln Fe_2O_{4.5}$ and $Ln FeMnO_{4.5}$. Similarly, we examined the oxygen uptake behavior of $LuMnGaO_4$, which contains the redox-active element Mn^{2+} and shares structural similarities with $Ln Fe_2O_4$ [45, 48] and $Ln FeMnO_4$ [50]. Thermogravimetric analysis (TGA) was performed on $LuMnGaO_4$ under flowing air. As shown Figure 3.1 and Figure 3.2, $LuMnGaO_4$ begins to absorb oxygen at approximately 250 °C, a higher temperature than $Ln Fe_2O_4$ (< 200 °C) and $Ln FeMnO_4$ (~ 200 °C). The oxidation process results in a 2.57(1) % weight gain in the final product, corresponding to an uptake of 0.603(2) oxygen atoms per formula unit. This value slightly exceeds the 0.5 moles of oxygen atoms expected from full oxidation of Mn^{2+} to Mn^{3+}. We attribute this to slight oxygen deficiency in the starting reduced material $LuMnGaO_{4-\delta}$, which would result in a slightly greater weight gain upon oxidation. To confirm that the small amount of impurity in the sample, $Lu_3Ga_5O_{12}$ does not influence the observed weight gain and oxidation, parallel measurements with $LuMnGaO_4$ were conducted under identical conditions (heated under air atmosphere, up to 700 °C), resulting in no weight gain (Figure 3.2).

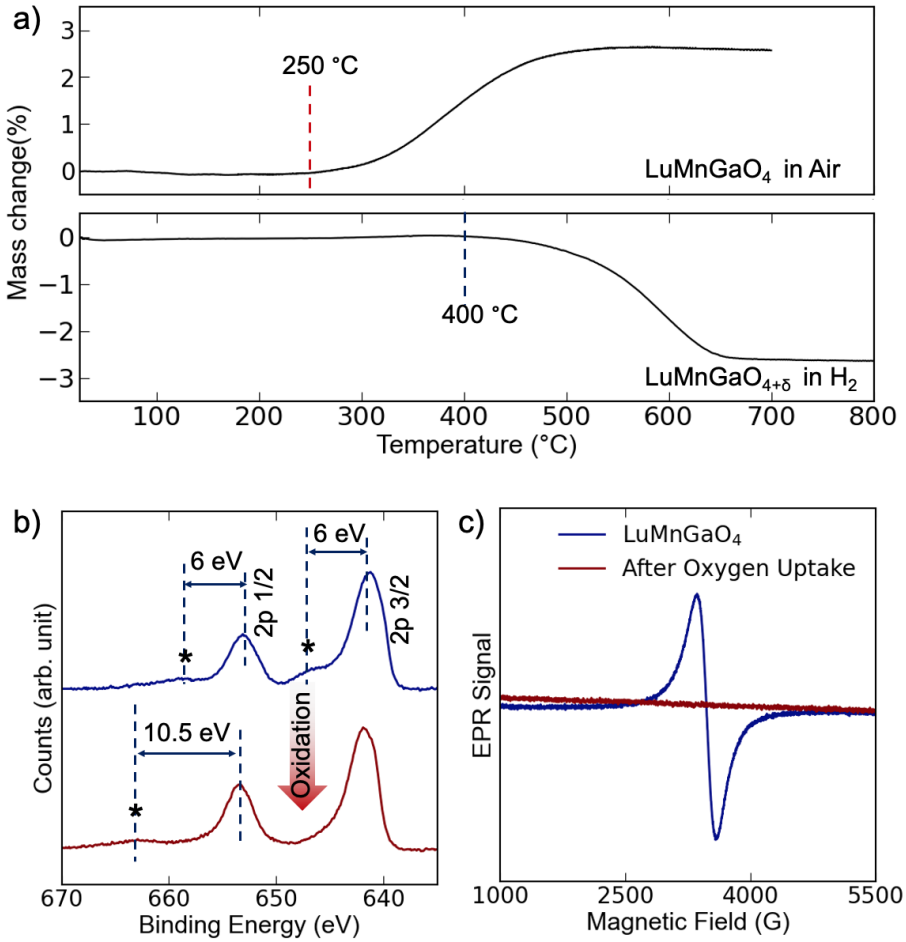


Figure 3.1: (a) Thermogravimetric analysis (TGA) measurements for $LuMnGaO_4$ in air (top) and $LuMnGaO_{4.5}$ in 3% H_2/Ar atmosphere (bottom). (b) Mn 2p XPS spectra comparison between LuMnGaO4 and $LuMnGaO_{4.5}$. (c) EPR Spectra of the samples.

To further verify the valence change of $LuMnGaO_4$ upon oxidation, XPS and EPR measurements were conducted on $LuMnGaO_4$ before and after oxidation. The Mn 2p XPS spectra are shown in Figure 3.1b. For $LuMnGaO_4$, the binding energy of Mn $2p_{3/2}$ and the satellite separation are 641.2 eV and 5.6 eV, respectively, while for $LuMnGaO_{4.5}$, these values are 641.8 eV and 10.5 eV. These results are consistent with reported values for Mn^{2+} and Mn^{3+} in MnO and Mn_2O_3 [73–76]. The Mn 3s XPS spectra analysis was also performed. Figure 3.3 shows the Mn 3s XPS spectra for $LuMnGaO_4$ and its oxidized counterpart, $LuMnGaO_{4.5}$. The binding energy difference of the Mn 3s multiplet splitting,

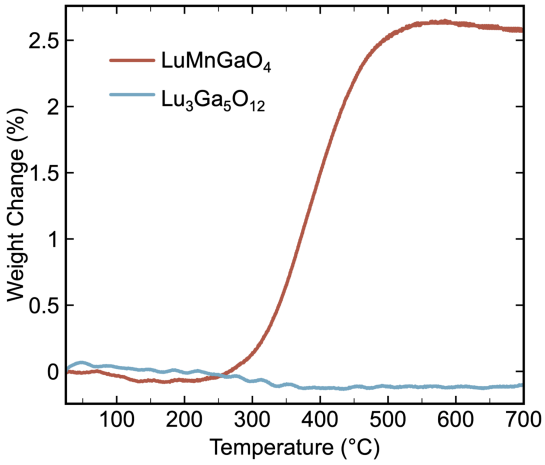


Figure 3.2: (a) Thermogravimetric analysis (TGA) of $LuMnGaO_4$ and the impurity, $Lu_3Ga_5O_{12}$.

often used to determine the Mn valence state in manganese oxides, is measured as 6.1 eV for $LuMnGaO_4$ and 5.6 eV for $LuMnGaO_{4.5}$. These values align with reported literature values for Mn^{2+} and Mn^{3+}, respectively, indicating an increase in the Mn oxidation state following oxygen uptake. This shift further supports the oxidation process occurring in the material.

EPR measurements further corroborated the oxidation from Mn^{2+} to Mn^{3+}. Since Mn is the only magnetic center in $LuMnGaO_{4+x}$, the EPR signal of $LuMnGaO_{4+x}$ exclusively originates from Mn. In parallel-mode X-band EPR spectroscopy, only ions with non-integer spin values respond to the magnetic field gradient [77]. The Mn^{2+} cations in $LuMnGaO_4$ are $S = 5/2$ (d^5, high spin) or $S = 3/2$ from 3 e^- occupation of the e'' manifold and, therefore, displays an EPR response, as presented in Figure 3.1c. However, after oxygen uptake, the EPR signal becomes silent, indicating oxidation to Mn^{3+} (d^4, $S = 2$) rather than Mn^{4+} (d^3, $S = 3/2$).

Overall, the TGA, XPS, and EPR data consistently demonstrate that $LuMnGaO_4$ transforms into $LuMnGaO_{4.5}$ upon oxygen uptake, accompanied by the oxidation of Mn^{2+} to Mn^{3+} within the structure. To investigate the reversibility of this progress, TGA measurements were performed on the oxidized phase, $LuMnGaO_{4.5}$, under a reducing atmosphere

(3 % H_2/Ar gas), as shown in Figure 3.1a. A weight decrease of -2.64(1) % was observed in the final product, indicating a reversible oxygen release, converting $LuMnGaO_{4.5}$ back to $LuMnGaO_4$. After reduction, the sample returned to its original greenish-grey color.

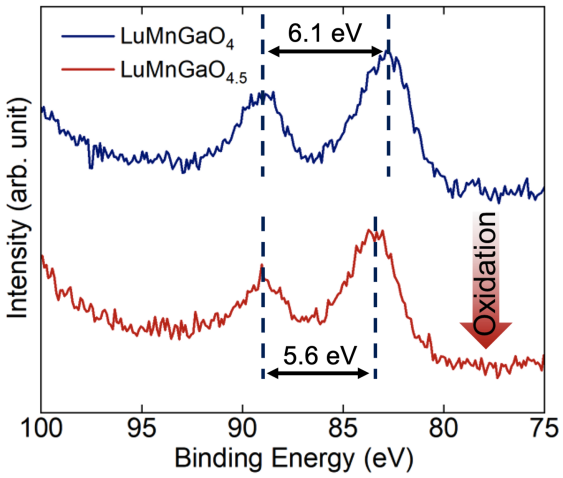


Figure 3.3: Mn 3s XPS spectra of $LuMnGaO_4$ and $LuMnGaO_{4.5}$

3.3.2 Crystal Structure of the reduced phase, $LuMnGaO_4$

The room-temperature neutron diffraction pattern of $LuMnGaO_4$, along with its Rietveld refinement, is shown in Figure 3.4a, with the refined parameters in Table 3.1. The structure was confirmed to be isostructural to the parent phase $LnFe_2O_4$, [33, 34, 44] belonging to space group $R\bar{3}m$, which served as the initial model for the refinement. The phase is nearly pure, with a minimal impurity of $Lu_3Ga_5O_{12}$ ($< 0.3\%$). The structure consists of alternating layers of Lu in octahedral coordination layers and trigonal bipyramidal Mn/Ga, where Mn and Ga are completely disordered as illustrated in Figure 3.13a [34, 78].

The refinement was initially conducted with Lu positioned at the Wyckoff position, 3a (0, 0, 0), yielding an agreement index (R_{wp}) value of 8.198 % (Figure 3.5, Table 3.2). The subsequent introduction of anisotropic thermal displacement for Lu reduced the R_{wp} by half (Figure 3.6, Table 3.3). However, the notable large thermal parameter along the c-axis for

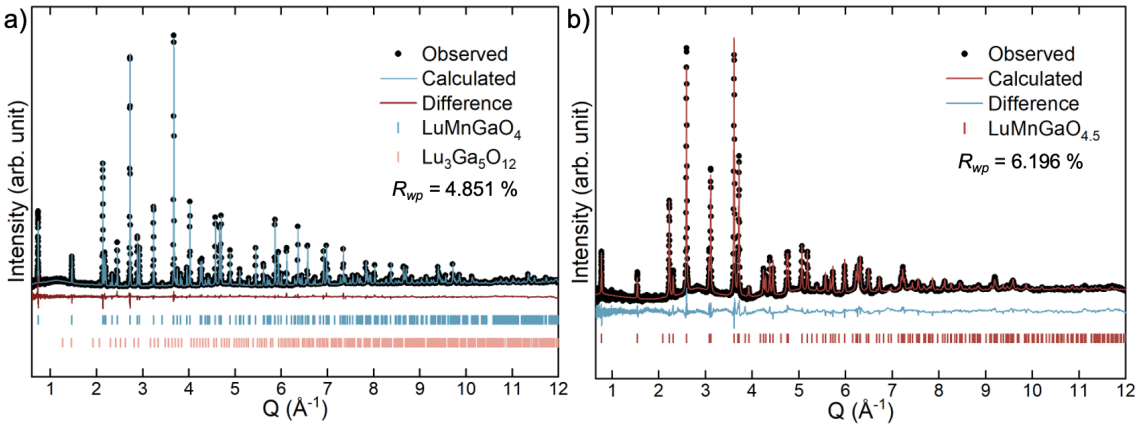


Figure 3.4: Neutron powder diffraction patterns and the Rietveld refinement fits for (a) the reduced phase, $LuMnGaO_4$, and (b) the oxidized phase, $LuMnGaO_{4.5}$. Data were collected using the POWGEN instrument at the Spallation Neutron Source, Oak Ridge National Laboratory, with wavelength 0.8 Å at 300 K.

Table 3.1: Structural parameters obtained from Rietveld refinement with neutron diffraction data (POWGEN, ORNL) for LuMnGaO4 ($R\bar{3}m$) at 300K, with $R_{wp} = 4.851$ %.

Atom	Wyc. Pos.	x	y	z	Site Occ.	U_{iso}	U_{11}	U_{22}	U_{33}	U_{12}	U_{13}	U_{23}
Lu	6c	0	0	0.00675(4)	0.5	0.0047(2)						
Mn	6c	0	0	0.22046(6)	0.5	0.0045(3)						
Ga	6c	0	0	0.22046(6)	0.5	0.0045(3)						
O1	6c	0	0	0.12779(3)	1		0.0098(2)	0.0098(2)	0.0118(3)	0.0048(1)	0	0
O2	6c	0	0	0.29271(3)	1		0.0267(4)	0.0267(4)	0.0363(5)	0.0134(2)	0	0

Lattice parameters

$a = b = 3.42515(2)$ Å $c = 25.7621(2)$ Å $\alpha = \beta = 90°$ $\gamma = 120°$ vol = 261.741(2) Å^3

Lu indicated static disorder in its positional arrangement along this direction, a phenomenon commonly observed in related compounds [66, 79]. Consequently, in the final structural model, Lu was slightly displaced from its ideal position and assigned to the 6c (0, 0, z) site [80], with the refined value of z = 0.00675(4). In this final refinement, the thermal vibration for Lu was isotropically refined, yielding a satisfactory fit consistent with previous observations for $LuCuGaO_4$. The refinement parameters are summarized in Table 3.1. The positional disorder of Lu is likely due to the significant chemical disparity between Mn and Ga, which share the same crystallographic site. The size difference between Mn (0.75 Å)[7] and Ga (0.55 Å)[7] creates variations in the local environment, particularly in their interactions with surrounding oxygen atoms bonded to Lu, resulting in a displacement of Lu along the c-axis.

The crystal structure of hexagonal-type AB_2O_4 compounds can also be represented by the space group $C2/m$, a maximal non-isomorphic subgroup of $R\bar{3}m$ [81]. The Rietveld refinement of the neutron pattern is shown in Figure 3.7. Refinement of the anisotropic thermal vibration of Lu and oxygen atoms yielded an R_{wp} of 4.793 %, with a notably large thermal elongation of Lu along the c-axis, similar to the case for $R\bar{3}m$ (Table 3.4 and Table 3.3). However, no peak splitting due to lattice distortion was observed in the Bragg peaks of the neutron diffraction pattern or high-resolution SXPD patterns (Figure 3.7 and Figure 3.8), indicating no need to lower the symmetry. Therefore, we conclude that the space group $R\bar{3}m$ best describes the reduced phase, $LuMnGaO_4$. The elemental composition of $LuMnGaO_4$ was verified using EDS (Table 3.5), which confirmed the stoichiometric ratios of the cations, Lu, Mn, and Ga. However, the oxygen content could not be accurately quantified by this method because of the low energy of the oxygen $K\alpha$ characteristic X-rays, which are significantly absorbed within the sample matrix before reaching the detector.

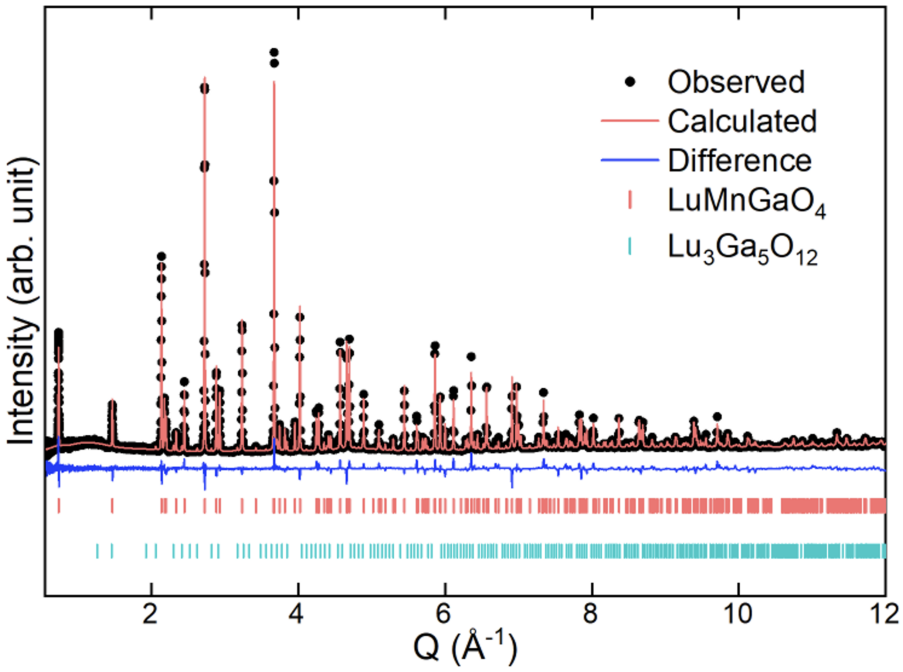


Figure 3.5: Neutron powder diffraction pattern of LuMnGaO4 and the Rietveld refinement with a structural model of $R\bar{3}m$. The refined structural parameters are shown in Table 3.2.

Table 3.2: Structural parameters obtained from Rietveld refinement of LuMnGaO4 with neutron diffraction with a structural model of $R\bar{3}m$. $R_{wp} = 8.198\%$. The thermal parameter of Lu atom, positioned at (0, 0 ,0) was refined isotropically.

Atom (Wyc. Pos.)	x	y	z	Site Occ.	U_{iso}	U_{11}	U_{22}	U_{33}	U_{12}	U_{13}	U_{23}
Lu(3a)	0	0	0	1	0.0131(2)						
Mn(6c)	0	0	0.2208(1)	0.5	0.0059(4)						
Ga(6c)	0	0	0.2208(1)	0.5	0.0059(4)						
O1(6c)	0	0	0.29261(4)	1		0.0067(3)	0.0067(3)	0.0200(5)	0.0033(2)	0	0
O2(6c)	0	0	0.12778(5)	1		0.0264(6)	0.0264(6)	0.0404(7)	0.0132(3)	0	0
Lattice parameters a = b = 3.42515(3) Å c =25.76020(2) Å α = β = 90° γ = 120° vol = 261.740(3) Å^3											

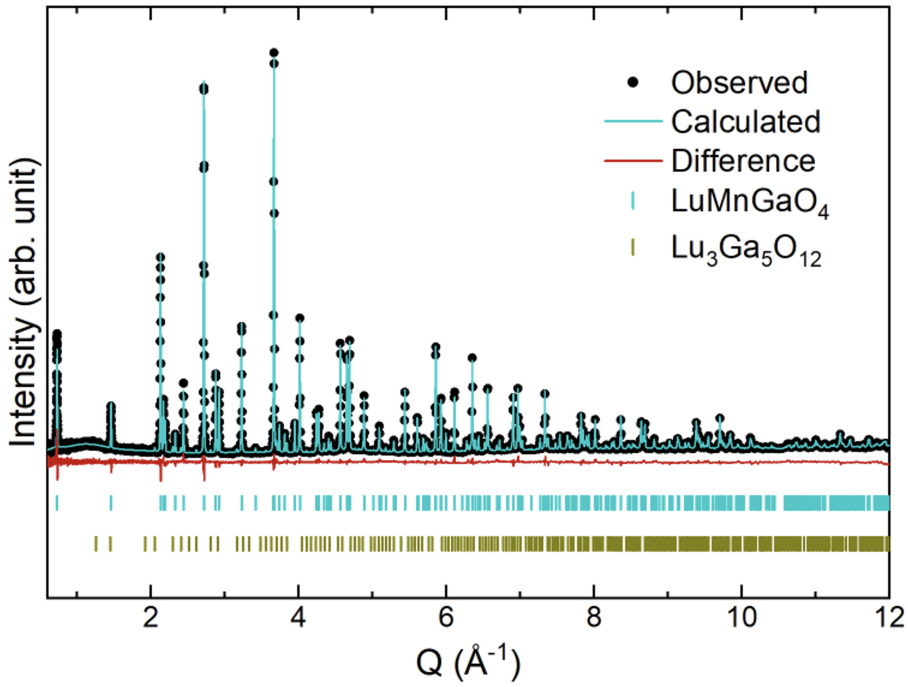


Figure 3.6: Neutron powder diffraction pattern of $LuMnGaO_4$ and the Rietveld refinement with a structural model of $R\bar{3}m$. The refined structural parameters are shown in Table 3.3

Table 3.3: Structural parameters obtained from Rietveld refinement of $LuMnGaO_4$ with neutron diffraction with a structural model of $R\bar{3}m$. $R_{wp} = 4.744\%$. The thermal parameter of Lu atom, positioned at (0, 0 ,0) was refined anisotropically.

Atom (Wyc. Pos.)	x	y	z	Site Occ.	U_{iso}	U_{11}	U_{22}	U_{33}	U_{12}	U_{13}	U_{23}
Lu(3a)	0	0	0	1		0.0040(3)	0.0040(3)	0.0430(5)	0.0020(1)	0	0
Mn(6c)	0	0	0.22047(1)	0.5	0.0045(3)						
Ga(6c)	0	0	0.22047(1)	0.5	0.0045(3)						
O1(6c)	0	0	0.29261(4)	1		0.0100(2)	0.0270(4)	0.0367(5)	0.0135(2)	0	0
O2(6c)	0	0	0.12778(5)	1		0.0270(4)	0.0270(4)	0.0367(5)	0.0135(2)	0	0
Lattice parameters a = b = 3.42516(2) Å c =25.7621(2) Å α = β = 90° γ = 120° vol = 261.741(2) Å^3											

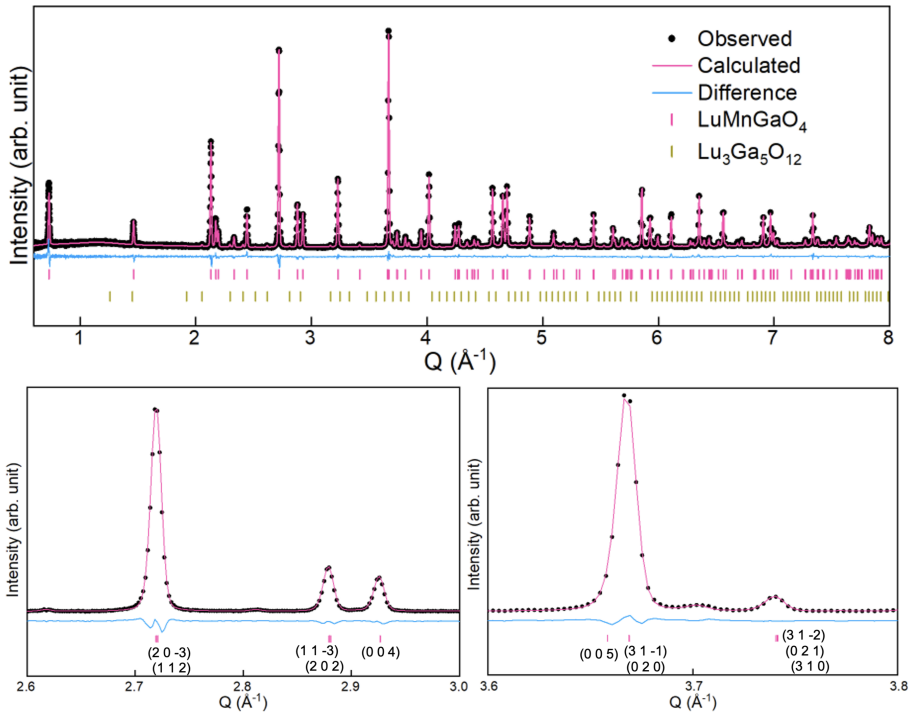


Figure 3.7: Neutron diffraction pattern of $LuMnGaO_4$ and Rietveld refinement with a structural model of $C2/m$. Data were collected using the POWGEN instrument at the Spallation Neutron Source, Oak Ridge National Laboratory, with wavelength 0.8 Å at 300 K.

Table 3.4: Structural parameters from Rietveld refinement of $LuMnGaO_4$ with neutron diffraction with a structural model of $C2/m$. $R_{wp} = 4.744\%$.

Atom (Wyc. Pos.)	x	y	z	Occ.	U_{iso}	U_{11}	U_{22}	U_{33}	U_{12}	U_{13}	U_{23}
Lu(2a)	0	0	0	1		0.008(2)	0.005(2)	0.0437(6)	0	0.014(3)	0
Mn(4i)	0.225(2)	0	0.6620(3)	0.5	0.0045(3)						
Ga(4i)	0.225(2)	0	0.6620(3)	0.5	0.0045(3)						
O1(4i)	0.2955(6)	0	0.8779(1)	1		0.011(2)	0.011(2)	0.0114(3)	0	0.002(2)	0
O2(4i)	0.128(1)	0	0.3834(2)	1		0.032(3)	0.027(3)	0.0376(5)	0	0.017(3)	0

Lattice parameters

a = 5.9328(3) Å b = 3.42502(7) Å c = 8.8134(5) Å α = γ = 90° β = 103.008(1)° vol = 174.493(2) Å^3

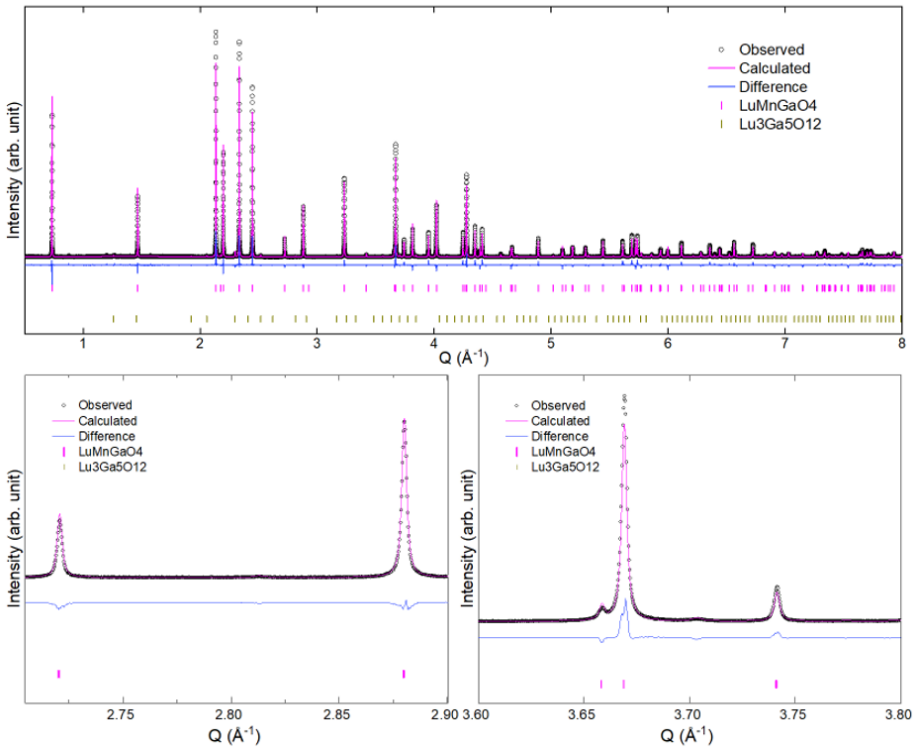


Figure 3.8: Synchrotron X-ray powder diffraction pattern of $LuMnGaO_4$ and Rietveld refinement with a structural model of $C2/m$. Data were collected using the 11-BM beamline at Advanced Photon Source, Argonne National Laboratory, with a wavelength of 0.457895 Å at 300 K.

Table 3.5: Elemental composition (%) analysis using energy dispersive X-ray spectroscopy (EDS) of $LuMnGaO_4$ and $LuMnGaO_{4.5}$.

	Atom (%)	
Element	$LuMnGaO_4$	$LuMnGaO_{4.5}$
Lu	17.45 ± 1.55	13.28 ± 1.51
Mn	17.97 ± 0.47	13.57 ± 0.45
Ga	17.68 ± 0.73	13.47 ± 0.73
O	46.90 ± 1.40	59.67 ± 2.21

3.3.3 Crystal structure of the oxidized phase, $LuMnGaO_{4.5}$

As anticipated from similar compounds, $LuMnGaO_{4.5}$ is structurally distinct compared to its reduced phase, $LuMnGaO_4$ [48, 50, 66]. A significant change in the neutron diffraction pattern is observed upon the oxygen uptake of $LuMnGaO_4$ (Figure 3.4b). Previous studies suggest that $LnFe_2O_4$ and $LnFeMnO_4$ transition from the $R\bar{3}m$ to $P\bar{3}$ space group upon oxidation [45, 46, 48, 49, 82]. Here, the $P\bar{3}$ structural model of $LnFe_2O_{4.5}$ and $LnFeMnO_{4.5}$ was used as the starting model to refine the average structure of $LuMnGaO_{4.5}$, yielding good agreement with the observed diffraction pattern, as shown in Figure 3.4b.

Table 3.6: Structural parameters obtained from Rietveld refinement with neutron diffraction data (POWGEN, ORNL) for $LuMnGaO_{4.5}$ ($P\bar{3}$) at 300 K, with $R_{wp} = 6.196\%$.

Atom	Wyc. Pos.	x	y	z	Site Occ.	U_{iso}
Lu	2c	0	0	0.0284(4)	0.5	0.0148(6)
Mn	2d	0.66667	0.33333	0.345(1)	0.5	0.019(2)
Ga	2d	0.66667	0.33333	0.345(1)	0.5	0.019(2)
O1	2d	0.66667	0.33333	0.1227(3)	1	0.0203(4)
O2	6g	0.242(2)	0.552(1)	0.4061(4)	0.265(2)	0.011(1)
O3	6g	0.011(4)	0.087(2)	0.3147(5)	0.152(2)	0.002(2)
Lattice parameters						
$a = b = 3.4801(1)$ Å $c = 8.1714(2)$ Å $\alpha = \beta = 90°$ $\gamma = 120°$ vol = 85.707(3) Å^3						

Initial refinements were conducted with Lu maintained at its special position (0, 0, 0) and isotropic thermal parameters, resulting in an R_{wp} value of 8.576% (Figure 3.9 and Table 3.7). Subsequent refinement of the thermal parameters for Lu and the oxygen atoms improved the fit. Similar to the refinement of $LuMnGaO_4$, Lu exhibited an unusual ellipsoidal elongation along the c-axis. Therefore, Lu was assigned to the 2c (0, 0, z) site, slightly shifted from its ideal position. The O2 and O3 oxygen atoms also exhibited elongation in the xy-plane, leading to slight shifts that placed them in disordered positions (Figure 3.10 and Table 3.8). This oxygen disorder was identified for the first time in $LnM_2O_{4.5}$-type materials and

attributed to the distinct chemical and size disparity between Mn and Ga. Compared to compounds where B sites are occupied by similar ions (e.g., Fe^{2+}/Fe^{3+} or Mn^{2+}/Fe^{3+}) [50, 66], the significant differences between Mn^{2+} and Ga^{3+} ionic radii contribute to local disorder. This disparity is evident when comparing neutron and electron diffraction patterns, as materials with less ion size disparity exhibit substantially less diffuse scattering than $LuMnGaO_{4.5}$ [50, 66, 81]. Additionally, this oxygen disorder brought on by Mn/Ga mixing leads to a more diffuse nature in the superlattice reflections, which get broadened out into the background of the neutron (Figure 3.4b) and 11-BM powder diffraction patterns (Figure 3.11 and Table 3.9). For the final refinement, the occupancies of O2 and O3 oxygens were constrained to have a sum of 0.417, and only the isotropic thermal parameters were refined. The final refinement results are provided in Table 3.6. The results from a dual refinement of the oxidized phase's structure at 300 K with both the neutron diffraction and synchrotron PXRD data sets can be found in Figure 3.12 and the resulting structural parameters in Table 3.10.

As shown in Figure 3.13b, oxygen is inserted into the Mn/Ga–O layers to occupy the O3 sites. The disordered oxygen sites are depicted in Figure 3.13c. The Mn/Ga site in the bilayer is coordinated by eight oxygen atoms, with partial occupancy at the O2 and O3 positions, which cannot be occupied simultaneously due to their short interatomic distance of 1.589(7) Å. This suggests that the observed Mn/Ga$-$O$_n$ polyhedral structure represents the average of multiple local polyhedral configurations. In a previous study on $YbFe_2O_{4.5}$, Nicoud et al. described a rearrangement of Fe coordination polyhedra following the insertion of interstitial oxygen, forming a range of FeO$_n$ polyhedral units ($n = 4, 5, 6$) within the double bipyramid layer [66]. Similarly, for $LuMnGaO_{4.5}$, we propose that the bilayer consists of a superimposition of trigonal bipyramid, tetrahedral, and octahedral polyhedra (Figure 3.13d). This is a qualitative suggestion based on previous work, as we have not conducted a quantitative analysis to determine the exact proportion of each polyhedral unit.

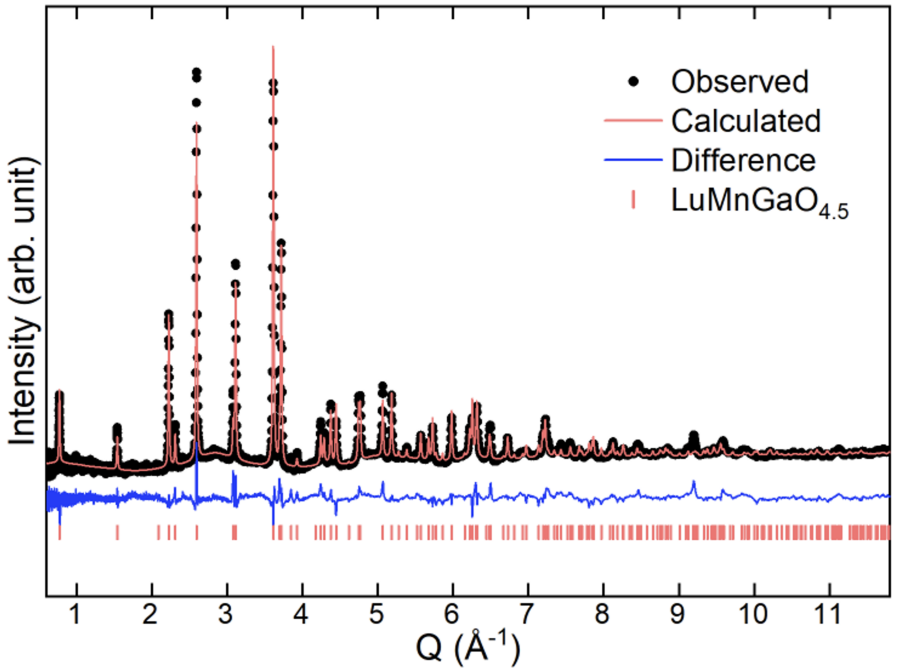


Figure 3.9: Neutron diffraction pattern of $LuMnGaO_{4.5}$ and Rietveld refinement with a structural model of $P\bar{3}$. The refined structural parameters are shown in Table 3.7.

Table 3.7: Structural parameters from Rietveld refinement of $LuMnGaO_4$ with neutron diffraction with a structural model of $C2/m$. $R_{wp} = 4.744\%$.

Atom (Wyc. Pos.)	x	y	z	Site Occ.	U_{iso}
Lu(1a)	0	0	0	1	0.041(1)
Mn(2d)	0.66667	0.33333	0.347(1)	0.5	0.017(1)
Ga(2d)	0.66667	0.33333	0.347(1)	0.5	0.017(1)
O1(2d)	0.66667	0.33333	0.1225(4)	1	0.0153(4)
O2(2d)	0.33333	0.66667	0.4048(8)	0.821(8)	0.072(2)
O3(2c)	0	0	0.3084(5)	0.429(8)	0.015(2)
Lattice parameters					
a = b = 3.4801(2) Å c = 8.1714(3) Å α = β = 90° γ = 120° vol = 85.707(4) $Å^3$					

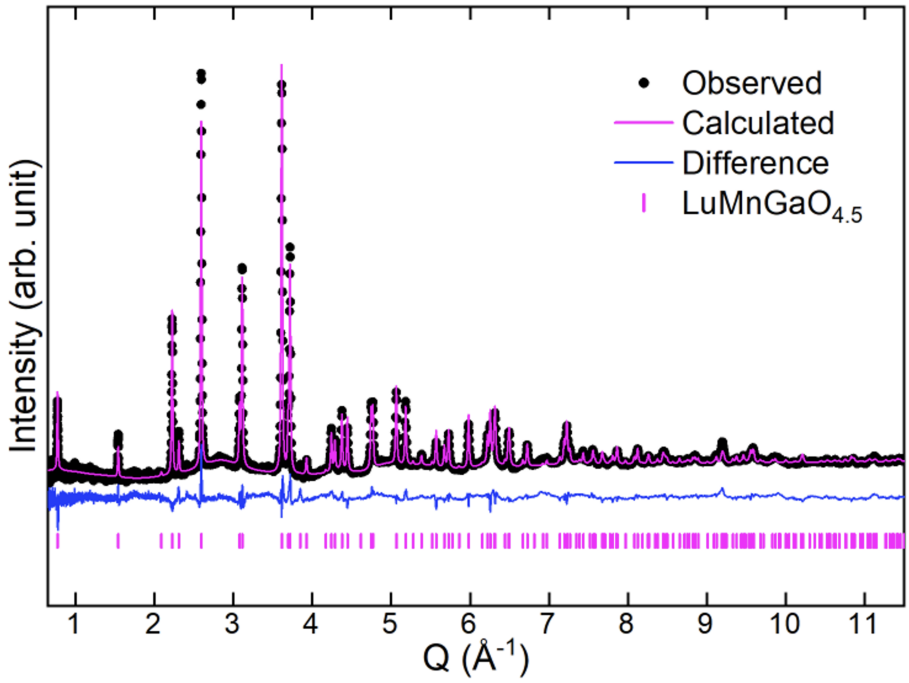


Figure 3.10: Neutron diffraction pattern of $LuMnGaO_{4.5}$ and Rietveld refinement with a structural model of $P\bar{3}$. The refined structural parameters are shown in Table 3.8.

Table 3.8: Structural parameters from Rietveld refinement of $LuMnGaO_{4.5}$ with a structural model of $P\bar{3}$. $R_{wp} = 8.576\%$. The thermal parameter of the Lu atom, positioned at (0, 0, 0), was refined anisotropically.

Atom (Wyc. Pos.)	x	y	z	Site Occ.	U_{iso}	U_{11}	U_{22}	U_{33}	U_{12}	U_{13}	U_{23}
Lu(1a)	0	0	0	1		0.0062(8)	0.0062(8)	0.095(3)	0.0031(4)	0	0
Mn(2d)	0.66667	0.33333	0.342(1)	0.5	0.0059(4)						
Ga(2d)	0.66667	0.33333	0.342(1)	0.5	0.0059(4)						
O1(2d)	0.66667	0.33333	0.1221(3)	1		0.027(1)	0.027(1)	0.013(1)	0.0135(5)	0	0
O2(2d)	0.33333	0.66667	0.4064(4)	0.7630		0.102(3)	0.102(3)	0.001(2)	0.051(2)	0	0
O3(2c)	0	0	0.3158(6)	0.4870		0.053(3)	0.053(3)	0.016(3)	0.027(1)	0	0

Lattice parameters

a = b = 3.4802(1) Å c = 8.1711(2) Å α = β = 90° γ = 120° vol = 85.7052(3) Å^3

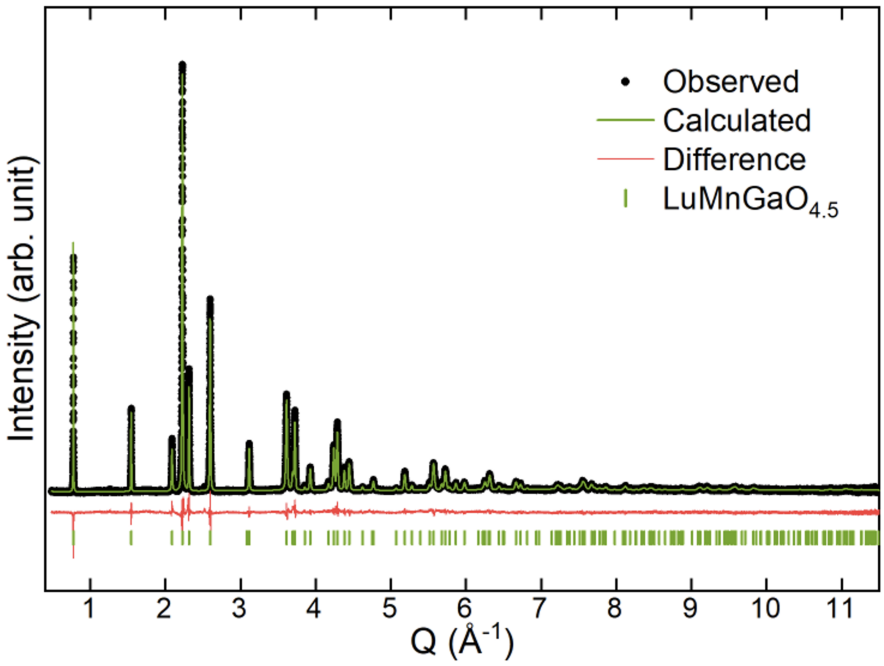


Figure 3.11: Rietveld refinement of $LuMnGaO_{4.5}$ at room temperature (RT) with high-resolution synchrotron X-ray powder diffraction using a structural model of $P\bar{3}$. A wavelength of 0.457895 Å was used. The refined structural parameters are shown in Table 3.9.

Table 3.9: Structural parameters from Rietveld refinement of $LuMnGaO_{4.5}$ with high-resolution synchrotron X-ray powder diffraction using a structural model of $P\bar{3}$. $R_{wp} = 12.488\%$. Occupancy was achieved using the constraint: $O2_{2d} + O3_{2c} = 1.25$.

Atom (Wyc. Pos.)	x	y	z	Site Occ.	U_{iso}	U_{11}	U_{22}	U_{33}	U_{12}	U_{13}	U_{23}
Lu(1a)	0	0	0	1		0.0001(1)	0.0001(1)	0.0766(6)	0.00004(6)	0	0
Mn(2d)	0.66667	0.33333	0.351(2)	0.5	0.0175(4)						
Ga(2d)	0.66667	0.33333	0.351(2)	0.5	0.0175(4)						
O1(2d)	0.66667	0.33333	0.1275(4)	1	0.015(1)						
O2(2d)	0.33333	0.66667	0.3992(9)	0.819(6)†	0.046(4)						
O3(2c)	0	0	0.3271(9)	0.431(6)†	0.017(2)						

Lattice parameters

a = b = 3.48298(3) Å c = 8.16177(6) Å α = β = 90° γ = 120° vol = 85.7465(8) Å^3

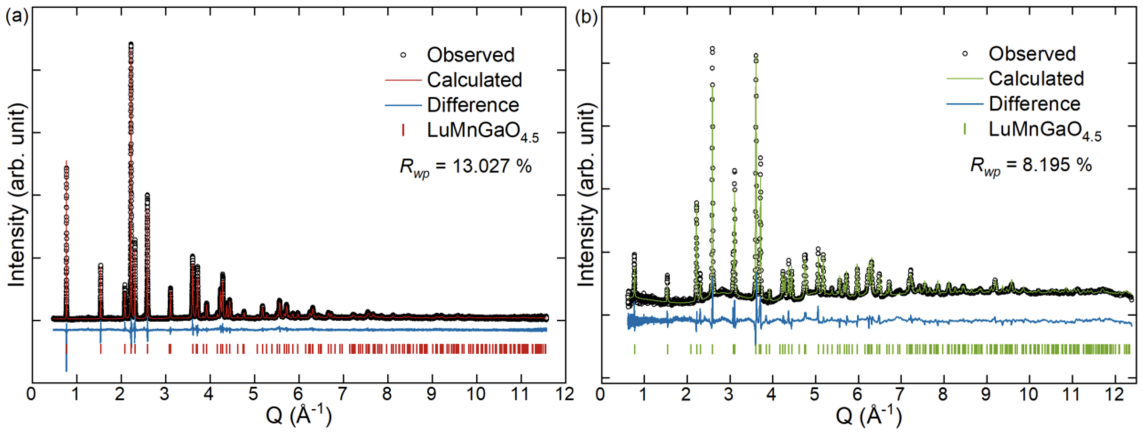


Figure 3.12: (a) SXPD pattern and (b) neutron diffraction pattern of $LuMnGaO_{4.5}$, shown with Rietveld refinement fits using a structural model of $P\bar{3}$ based on a combined refinement of the two datasets. Synchrotron data were collected at 300 K using the 11-BM beamline at the Advanced Photon Source, Argonne National Laboratory, with a wavelength of 0.457895 Å. Neutron data were collected at 300 K using the POWGEN beamline at the Spallation Neutron Source, Oak Ridge National Laboratory, with a central wavelength of 0.8 Å.

Table 3.10: Structural parameters from the combined Rietveld refinement of $LuMnGaO_{4.5}$ with synchrotron PXRD and neutron diffraction with a structural model of $P\bar{3}$.

Atom	Wyc. Pos.	x	y	z	Site Occ.	U_{iso}
Lu	2c	0	0	0.02888(8)	0.5	0.0030(1)
Mn	2d	0.66667	0.33333	0.3512(2)	0.5	0.0173(3)
Ga	2d	0.66667	0.33333	0.3512(2)	0.5	0.0173(3)
O1	2d	0.66667	0.33333	0.1261(2)	1	0.0260(3)
O2	6g	0.242(1)	0.5613(8)	0.4044(2)	0.272(1)	0.0068(8)
O3	6g	0.013(3)	0.080(1)	0.3141(3)	0.144(1)	0.0063(9)
Lattice parameters						
$a = b = 3.48229(1)$ Å $c = 8.16423(6)$ Å $\alpha = \beta = 90°$ $\gamma = 120°$ vol = 85.7387(9) Å^3						

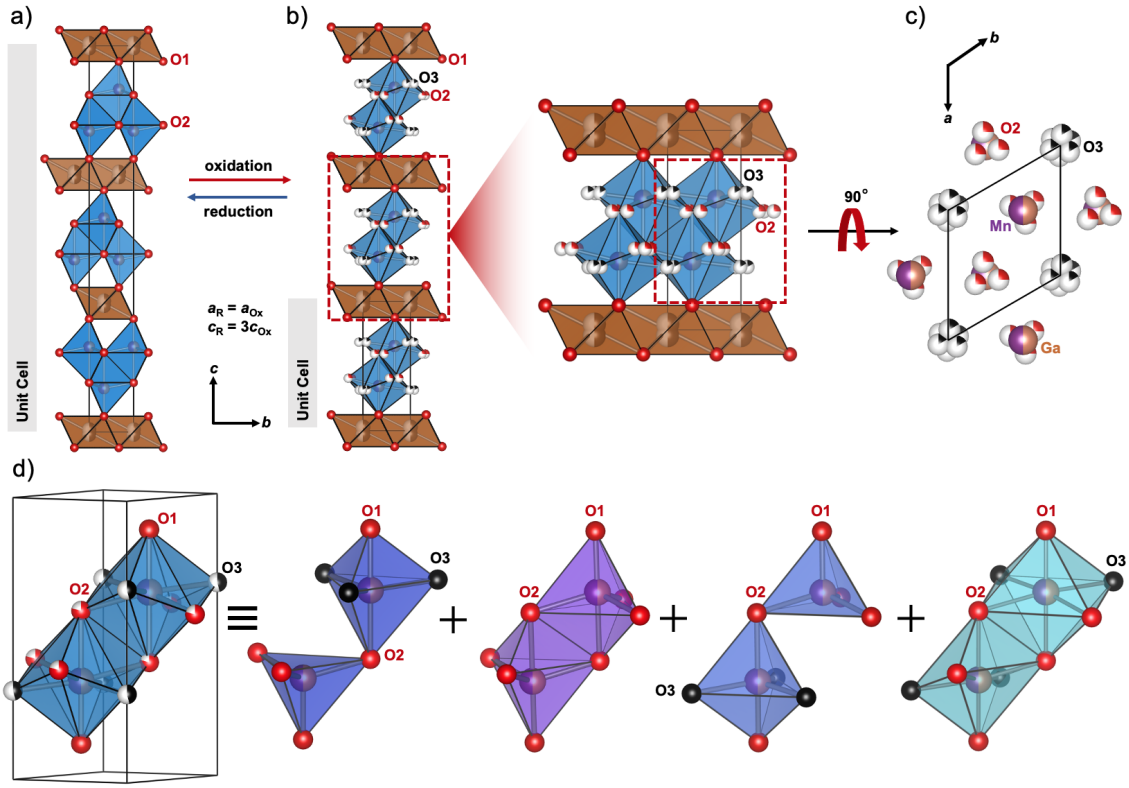


Figure 3.13: Crystal structures of (a) $LuMnGaO_4$ ($R\bar{3}m$) and (b) $LuMnGaO_{4.5}$ ($P\bar{3}$) along the c-axis. (c) $LuMnGaO_4$ structure rotated 90° to display the ab plane, highlighting the disordered oxygen. (d) Superimposed Mn/GaO_n polyhedra (n = 4, 5, 6) forming the average Mn/GaO_n double layer structure.

The splitting of oxygen positions O2 and O3 from their special positions indicates complex oxygen disorder, likely contributing to the structural modulation observed in the oxidized phase, as evident in the selected-area electron diffraction (SAED) patterns discussed below (Figure 3.13d, e, f).

3.3.4 Diffuse scattering and modulation structures

Figure 3.14a, c and Figure 3.14d, f present the SAED patterns for the reduced and oxidized phases, respectively, with the reciprocal lattice indicated and several reflections (h,k,l) labeled. In the reduced phase, the SAED pattern along the [001] zone axis in Figure 3.14a reveals regular Bragg spots of $\{110\}$ and $\{300\}$. Additionally, weak $\{100\}$ Bragg reflections are present, which might result from multiple scattering due to the increased specimen thickness. The electron diffraction was performed on crushed powders with a selected-area aperture covering a dimension of a few hundred nm scale. Furthermore, the SAED pattern along the [110] zone axis in Figure 3.14c reveals regular Bragg spots accompanied by weak diffuse streaks, which are within the green circle indicated by the red arrow. This diffuse streak is parallel to the [106] direction and may correspond to the background hump observed in the neutron diffraction pattern at lower Q (Figure 3.4a).

Upon oxidation and structural transformation, the SAED patterns show significant differences. First, the [001] zone axis SAED pattern for $LuMnGaO_{4.5}$ in Figure 3.14d reveals a sharp intensity of the $\{100\}$ Bragg spots compared to the weak reflection condition in Figure 3.14a, indicating different reflection conditions. Second, six additional diffuse satellite reflections appear around each Bragg reflection, marked by a blue cube, which cannot be indexed using the unit cell of the $P\bar{3}$ space group listed in Table 3.6. Furthermore, the [110] zone axis SAED pattern for $LuMnGaO_{4.5}$ in Figure 3.14f reveals additional weaker $\{1/3\ 0\ 0\}$ and $\{0\ 2/3\ 0\}$ superlattice reflections, in contrast to the diffuse streaks seen in Figure 3.14c. These satellite reflections indicate the presence of structural modulations, which lead to a new periodic arrangement in the HRTEM images from Figure 3.14b and d, caused by oxygen order leading to a superlattice. These satellite peaks are also evident in the SXPD data shown in Figure 3.15.

3.3.5 Structural evolution of $LuMnGaO_4$ during oxygen insertion

An in-situ SXPD experiment was conducted to investigate the structural evolution of $LuMnGaO_4$ upon heating. Figure 3.15a shows the contour plots of in-situ SXPD patterns for $LuMnGaO_4$ heated in air up to 700 °C. Below 350 °C, no new reflections were observed, indicating that the room temperature structure of $LuMnGaO_4$ was maintained. A phase transition began at approximately 350 °C, consistent with the TGA results (Figure 3.1a). Sequential refinement of the in-situ measurements revealed that this transition differs from that of the parent phase $LuFe_2O_4$, which forms a supercell structure around 250 °C, as evidenced by satellite reflections in SXPD data. Additionally, an intermediate phase appears before $LuFe_2O_4$ fully oxidizes to $LuFe_2O_{4.5}$. In contrast, for $LuMnGaO_4$ the phase transition occurs without an intermediate phase and directly coincides with oxygen absorption.

Figure 3.15c presents four selected SXPD patterns from the sequential in-situ measurements at 50 °C, 350 °C, 450 °C, and 600 °C, illustrating the changes in SXPD patterns upon heating. The evolution of lattice parameters a and c over the entire temperature range is depicted in Figure 3.16, where the c parameters of the oxidized phases ($P\bar{3}$) are multiplied by three for direct comparison with those of the reduced phases ($R\bar{3}m$). As the reduced phase oxidizes, the lattice parameter a increases, while c decreases. These structural changes align well with the weight changes observed in TGA. The Rietveld refinements of the SXPD patterns at 50 °C, 350 °C, 450 °C, and 600 °C are shown in Figure 3.17. A closer examination of the magnified SXPD patterns reveals additional satellite peaks (Figure 3.15 and Figure 3.18), also observed in the SAED patterns (Figure 3.14d-f). These peaks emerge above 400 °C during heating and indicate a structural modulation that resembles one observed previously in LnMnFeO$_4$ [50].

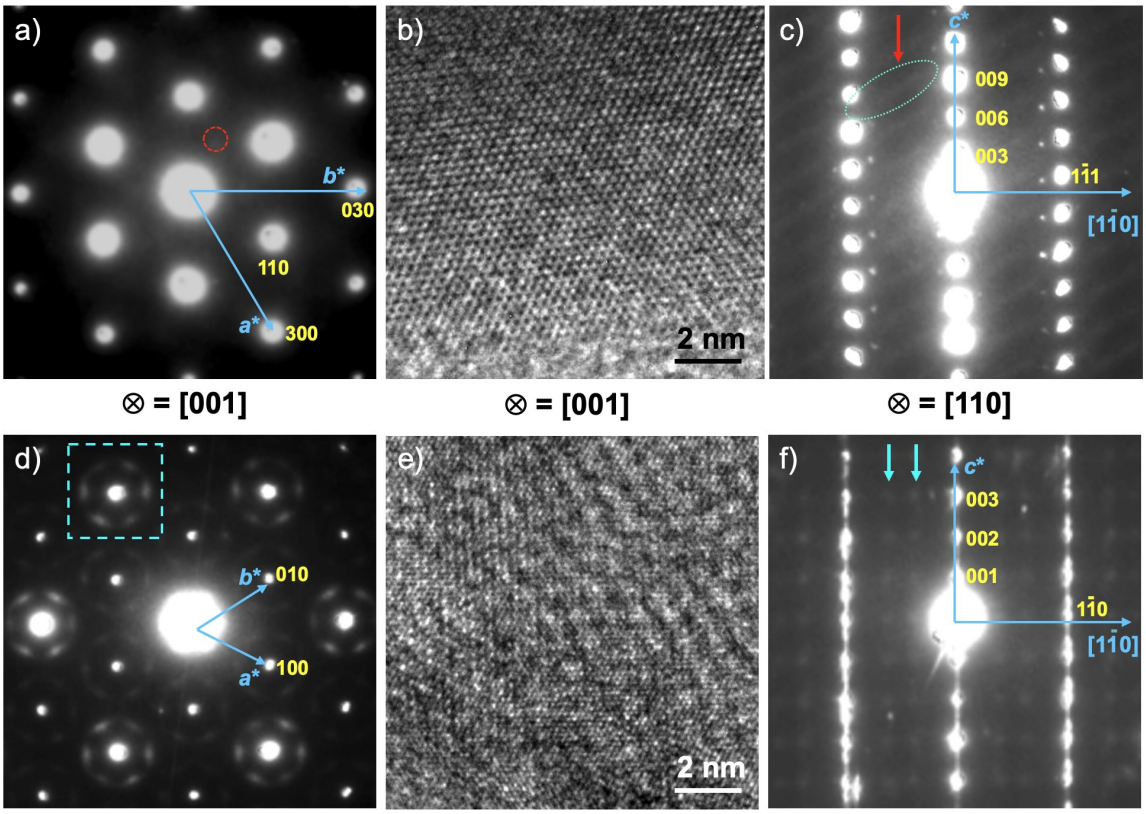


Figure 3.14: (
a, d) and [110] (c, f) zone axes for (a, c) $LuMnGaO_4$ and (d, f) $LuMnGaO_{4.5}$.]Selected-area electron diffraction patterns along [001] (a, d) and [110] (c, f) zone axes for (a, c) $LuMnGaO_4$ and (d, f) $LuMnGaO_{4.5}$. Indexed diffraction spots are labeled in yellow. In (a, c), diffuse scattering is indicated by red circles and streaks marked by green circles observed in $LuMnGaO_4$. In (d, f), the blue cube and arrows indicate structural modulation in $LuMnGaO_{4.5}$. (b, e) The HRTEM images recorded along the [001] zone axis for (b) $LuMnGaO_4$ and (e) $LuMnGaO_{4.5}$. A modulation structure is revealed in (e).

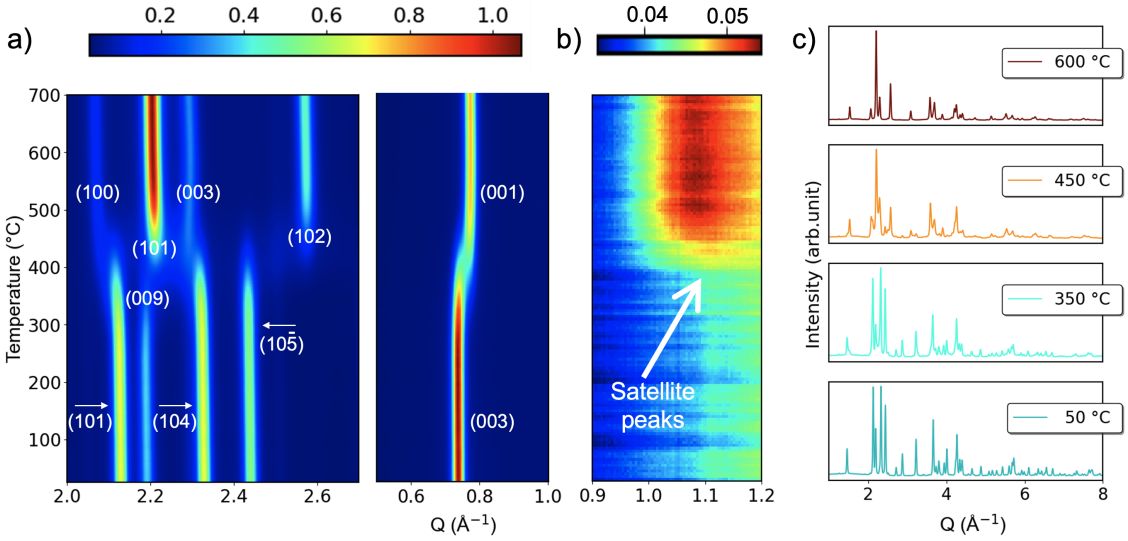


Figure 3.15: In-situ SXPD of $LuMnGaO_4$ as it oxidizes. (a) Contour plots of in-situ SXPD data for $LuMnGaO_4$ heated in air from 25 °C to 700 °C. (b) Enlarged view (magnified 20×) highlighting the appearance of satellite peaks. (c) Selected diffraction patterns at 50 °C, 350 °C, 450 °C, and 600 °C.

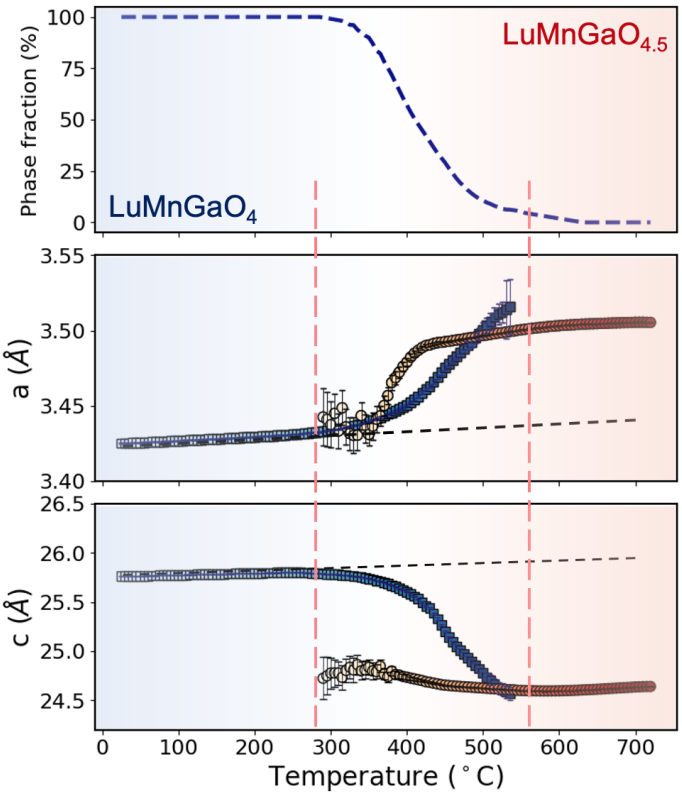
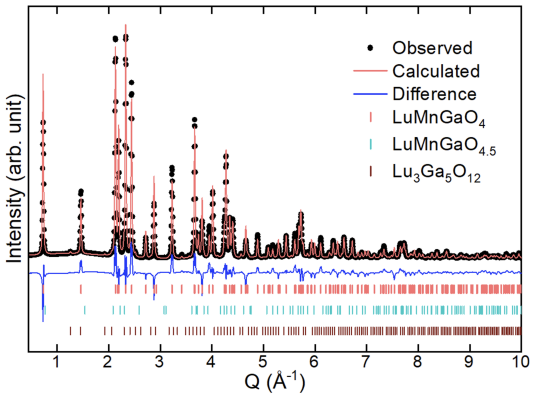
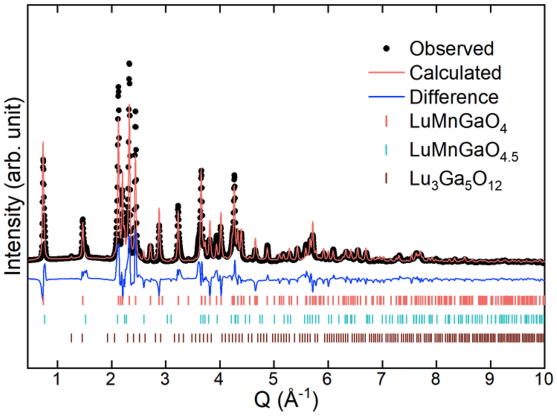


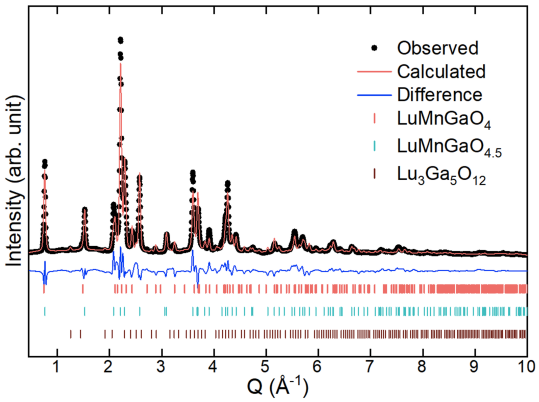
Figure 3.16: Evolution of phase fractions and lattice parameters, a and normalized c, as a function of temperature in air, derived from sequential Rietveld refinements of in-situ SXPD data. The top panel shows the phase fraction transition from $LuMnGaO_4$ to $LuMnGaO_{4.5}$, while the middle and bottom panels display the corresponding changes in the lattice parameters a and c, respectively. The red dashed lines indicate where phase transformation or structural changes occur.



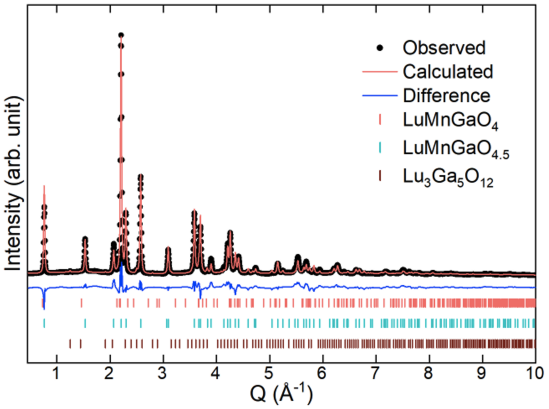
(a) 50°C; $R_{wp} = 11.585\%$



(b) 350°C; $R_{wp} = 14.959\%$



(c) 450°C; $R_{wp} = 10.171\%$



(d) 600°C; $R_{wp} = 9.337\%$

Figure 3.17: SXPD patterns of LuMnGaO4 at various temperatures showing Rietveld refinement analysis. Phase compositions for (a) 50°C, (b) 350°C, (c) 450°C, and (d) 600°C are detailed in the text.

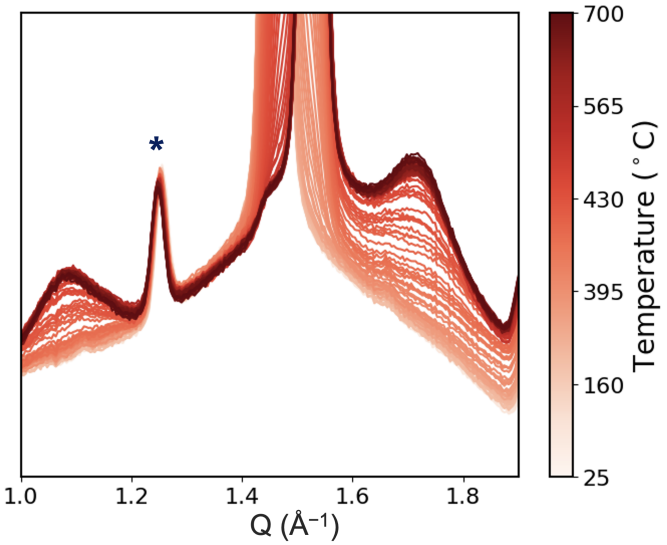


Figure 3.18: Temperature-dependent SXPD patterns. Satellite peaks emerge around 1.1 $Å^{-1}$ and 1.7 $Å^{-1}$, indicating structural modulation. The peak marked with * corresponds to an impurity phase.

3.3.6 Color change from $LuMnGaO_4$ to $LuMnGaO_{4.5}$

The structures of $LuMnGaO_4$ and related compounds are closely correlated with the $YIn_{1-x}Mn_xO_3$ phases, where the hexagonal structure consists of layers of Y^{3+} ions separating layers of corner-shared MO_5 trigonal bipyramids (M = In, Mn) [83–85]. This compound exhibits a bright-blue hue due to the crystal field splitting of Mn^{3+} in trigonal bipyramidal coordination. Building on this understanding, we investigated the distinct color change in $LuMnGaO_4$ upon oxygen insertion, focusing on the role of the Mn site during oxidation.

The reduced phase of $LuMnGaO_4$ exhibits a greenish-grey hue as shown in Figure 3.19. Following oxidation, the color transitions to black. Diffuse reflectance spectra and approximated absorbance spectra, calculated using the Kubelka-Munk function, confirmed this chromatic shift [86]. The blue curve in Figure 3.19 represents the absorbance spectra of $LuMnGaO_4$, with two major peaks at 2 eV and 3.7 eV, while the red curve for $LuMnGaO_{4.5}$ displays broad absorption across the visible spectrum, consistent with the black color.

The color change could be attributed to either a d-d transition or ligand-to-metal charge transfer. First, we describe the transition arising from the Mn/Ga-O trigonal bipyramidal coordination. It has been explained that the blue hue of $Y(In,Mn)O_3$ arises from the crystal field splitting of Mn^{3+} in trigonal bipyramid coordination [84]. Similarly, $LuMnGaO_4$ consists of double layers of edge-sharing trigonal bipyramidal units, where Mn and Ga are disordered at the same site. In the reduced phase, Mn^{2+}, with five d-electrons, occupies the doubly degenerate e' and e'' energy levels. Spin- and symmetry-allowed transitions would therefore include $e' \rightarrow a'$ and $e'' \rightarrow a'$, corresponding to the absorption peaks at 2 eV and 3.7 eV, respectively. The lack of absorption in the 450–600 nm range results in the greenish-grey hue. Upon oxidation, Mn oxidizes to the +3 state, as confirmed by XPS and EPR spectra (Figure 3.1b and c). This oxidation alters the coordination geometry from trigonal bipyramidal to a combination of octahedral, tetrahedral, and trigonal bipyramidal

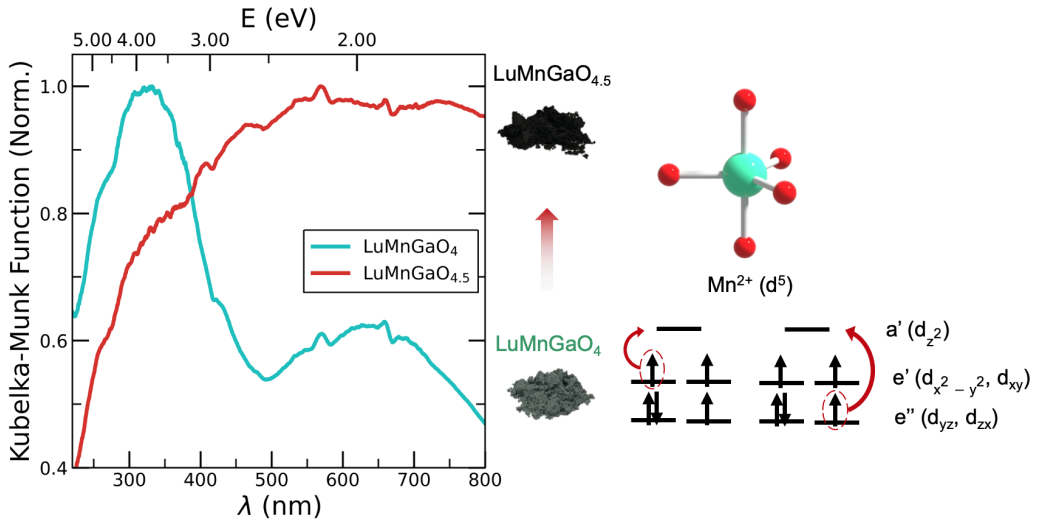


Figure 3.19: Color change from $LuMnGaO_4$ to $LuMnGaO_{4.5}$, and corresponding UV-vis spectroscopy measurements. The y-axis represents the Kubelka-Munk transformed absorbance spectra. The schematic energy levels for Mn^{2+} $3d$ orbitals in trigonal bipyramidal coordination are shown, with possible electronic transitions ($e' \rightarrow a'$ and $e'' \rightarrow a'$) contributing to the observed color of $LuMnGaO_4$.

configurations. These complex crystal field environments produce broad absorption across the visible spectrum, which results in the black color.

The second possibility to understand the origin of color in $LuMnGaO_4$ is the ligand-to-metal charge transfer (LMCT). Manganese (II) oxide (MnO), which crystallizes in a cubic rock-salt structure with Mn^{2+} ions in octahedral coordination, exhibits a green color [87]. MnO has been widely studied as a borderline between a Mott insulator and a charge-transfer insulator [88, 89]. The optical band gaps of the colloidal MnO nanoparticles have been reported to be 3.19 eV and 2.18 eV, attributed to the direct and indirect transitions respectively, arising from the O 2p–Mn e_g transitions [90]. Although the Mn/Ga sites in $LuMnGaO_4$ adopt a trigonal bipyramidal coordination rather than an octahedral, the UV-vis absorption occurred at 3.7 eV and 2 eV are similar to those in MnO. The resemblance suggests that LMCT transitions involving O 2p to Mn 3d orbitals may also contribute to the optical absorption in $LuMnGaO_4$ alongside crystal field effects.

The pronounced color change from greenish-grey ($LuMnGaO_4$) to black ($LuMnGaO_{4.5}$) highlights the potential of this material for colorimetric oxygen sensing. Color sensing, which translates color changes into quantifiable data, has applications in environmental monitoring, diagnostics, and industrial processes [91, 92]. These systems leverage reflected or transmitted light to detect chromatic transitions, employing advanced algorithms and optical systems for enhanced sensitivity [93]. In $LuMnGaO_4$, the oxidation-induced Mn coordination transformation enables efficient oxygen detection, positioning this material as a potential candidate for oxygen and colorimetric sensing applications.

3.4 Conclusion

In this study, we have synthesized and characterized the reduced and oxidized phases of $LuMnGaO_4$, exploring their structural evolution and unique color changes upon oxygen insertion. Using neutron and SXPD diffraction, we determined that the reduced phase ($LuMnGaO_4$) crystallizes in the $R\bar{3}m$ space group, while the oxidized phase ($LuMnGaO_{4.5}$) adopts the $P\bar{3}$ space group. Our in-situ SXPD experiments revealed a phase transition during oxidation, accompanied by a distinct shift in color from greenish-grey to black, confirmed through UV-visible spectroscopy. The observed color change is attributed to changes in the coordination geometry of the Mn/Ga-O layer, which transitions from trigonal bipyramid to a combination of octahedral, tetrahedral, and trigonal bipyramidal configurations. The structural modulations and satellite peaks indicate complex oxygen ordering and disordering. These findings highlight the potential of $LuMnGaO_4$ as a bifunctional material, with promising applications in both oxygen transport and sensing technologies at relatively low temperatures. This study provides new insight into the structure-property relationships of AB_2O_4-type compounds and lays the groundwork for further investigations into the effects of elemental substitution and phase transitions in oxygen carrier materials.

Chapter 4: Comparative Structural and Functional Analysis of AMnGaO$_4$ (A = Yb and In)

4.1 Introduction

Layered oxide materials, including the perovskite (ABO_3), Ruddlesden-Popper (A_2BO_4), and double perovskite ($A_2B_2O_6$) families, provide a versatile platform for tuning chemical and physical properties through strategic ionic substitution. A prominent example is LaMnO3-based perovskites, which are widely utilized in energy conversion and catalytic applications due to their robust structural stability [94]. While the oxygen storage capacity (OSC) of stoichiometric LaMnO3 is relatively limited, it can be significantly enhanced via A-site doping. For example, Ce-doped $La_{1-x}Ce_xMnO_3$ has recently been reported as an effective electrocatalyst for the Oxygen Reduction Reaction (ORR) in Zn-air batteries [95]. Similarly, Sr-substitution in $La_{1-x}Sr_xMnO_3$ has been shown to advance electrochemical performance in supercapacitors [96, 97]. The underlying principle of these enhancements is charge compensation. By substituting a trivalent La^{3+} with a divalent or tetravalent cation induces a mixed-valence state in the manganese (Mn^{3+}/Mn^{4+}), which facilitates the formation of oxygen vacancies and thus enhances ionic mobility.

Beyond electrochemical performance, A-site substitution can influence fundamental physical properties as well. The rare-earth nickelates ($ANiO_3$, where A = lanthanide) serve as a good example [98]. The ionic radius of the A-site cation influences the tilting of the NiO_6 octahedra and this distortion reduces the $Ni-O-Ni$ bond angle, thereby narrowing

the electronic bandwidth and altering the superexchange interactions. Consequently, the metal-insulator transition could be controlled through the tuning of *A*-site elements.

Inspired by these structure-property relationships, this chapter expands upon the investigation of the layered AMnGaO$_4$ system initiated in Chapter 3 with LuMnGaO$_4$. Here, we specifically explore the effects of *A*-site substitution by comparing the Yb- and In-analogues: YbMnGaO$_4$ and InMnGaO$_4$. We use high-resolution synchrotron X-ray diffraction and thermogravimetric analysis to compare their oxidation behavior and discuss how variations in *A*-site cation chemistry and bonding characteristics influence lattice flexibility and oxygen uptake capability.

Interestingly, these materials also exhibit complex magnetic behavior that is inextricably linked to their structure. Recently, YbMgGaO$_4$[99] and YbZnGaO$_4$ [100] have emerged as candidates for Quantum Spin Liquids (QSLs). In a QSL state, spins remain disordered even as temperatures approach absolute zero. Unlike a standard paramagnet, however, the spins are highly correlated through energy scales comparable to those of magnetically ordered systems [101].

These QSL states are predicted to occur in triangular systems with interactions extending beyond nearest neighbors, especially in materials with strong spin-orbit coupling [100]. Both YbMgGaO$_4$ and YbZnGaO$_4$ crystallize in $R\bar{3}m$ space group, with Yb^{3+} ions arranged in a triangular lattice and the Mg/Zn and Ga ions occupying a trigonal bipyramidal double layer. This makes the system particularly interesting, as the Yb^{3+} ($J = 1/2$) ions represent a rare example of a triangular lattice composed of lanthanide ions [99, 101]. It has been argued that site-mixing between the non-magnetic cations induces structural disorder that plays a major role in this phenomenon, though research into this remains ongoing.

In our previous research, Li et al. reported the structural modulation and spin glassiness upon oxidation in *Ln*FeMnO$_4$ (*Ln* = Y, Lu, and Yb) materials [50]. That study discussed not only the oxygen storage behavior as different trivalent cations are substituted but also

dived into the spin-glass behavior of both the reduced and oxidized phases, with short-range magnetic ordering observed in the reduced phases.

In the final section of this chapter, we include magnetic susceptibility data analysis and neutron diffraction measurements to discuss the spin-glass behavior observed in our materials.

4.2 Experimental

4.2.1 Materials synthesis

The reduced phase, $YbMnGaO_4$, was synthesized by solid-state reactions. Stoichiometric amounts of Yb_2O_3 (99.99%), MnO (99%), and Ga_2O_3 (99.999%) were thoroughly ground, pressed into 13 mm diameter pellets, and placed in a 2 mL alumina crucible. The crucible was placed in an 16 mm diameter quartz ampoule, sealed, and heated to 1180 °C at a ramp rate of 5 °C min^{-1}. The sample was held at this temperature for 24 hours and subsequently quenched in an ice-water bath. The oxidized phase, $YbMnGaO_{4.5}$, was obtained by heating $YbMnGaO_4$ at 600 °C for 12 hours, followed by a natural cooling to room temperature.

For $InMnGaO_4$, Stoichiometric amounts of In_2O_3 (99.99%), MnO (99%), and Ga_2O_3 (99.999%) were mixed, ground, and pelletized. The sealed ampoule was heated to 900 °C for 64 hours, followed by quenching in an ice bath. Additional annealing experiments were carried out at various temperatures up to 950 °C to investigate possible phase transitions.

4.2.2 Thermogravimetric analysis (TGA)

TGA of the reduced phases, $YbMnGaO_4$ and $InMnGaO_4$, was performed using a TA Instruments Discovery TGA-5500. Approximately 10 mg of each sample was loaded into

platinum pans (100 μL) and heated in air to 950 °C at a rate of 10 °C min^{-1}.

4.2.3 X-ray diffraction (XRD)

High-resolution synchrotron X-ray powder diffraction (SXPD) data were collected at the I11 beamline of Diamond Light Source, UK, using X-rays with a wavelength of 0.8241 Å[55]. Measurements were performed at room temperature (300 K) on the reduced and oxidized phases of $YbMnGaO_4$, as well as on $InMnGaO_4$ samples previously annealed at 600 °C and 950 °C.

Laboratory X-ray diffraction was performed ex situ on a Bruker D8 Advance diffractometer equipped with a Cu Kα radiation source at the X-ray Crystallographic Center at University of Maryland under ambient conditions. In-situ diffraction experiments on $YbMnGaO_4$ were carried out using an Anton Paar XRDynamic 500 diffractometer with a Cu Kα source. The temperature was ramped to 700 °C at a heating rate of 5 °C min^{-1}.

4.2.4 Neutron diffraction

Time-of-flight neutron powder diffraction data were collected at the POWGEN beamline at the Spallation Neutron Source, Oak Ridge National Laboratory. Data were acquired at 300 K and 7 K using detector banks 1 and 3, which provide d-spacing coverages of 0.1–8 Å and 1–20.5 Å with central wavelengths (CWL) of 0.8 Å and 2.665 Å, respectively.

4.2.5 Magnetic susceptibility measurements with SQUID

Temperature- and field-dependent magnetic susceptibility measurements of $YbMnGaO_4$, $YbMnGaO_{4.5}$, and $InMnGaO_4$ were carried out using a 7 T Quantum Design Superconducting Quantum Interference Device magnetometer (MPMS3). Direct current (dc) magnetization measurements were collected under zero-field-cooled (ZFC) conditions while warming

from 2 K to 300 K. Field-cooled (FC) data were subsequently recorded during cooling back to 2 K. Magnetic susceptibility measurements were performed under applied fields of 100 Oe and 1000 Oe.

4.3 Results and Discussion

4.3.1 Structural analysis upon annealing

The average crystal structure of $YbMnGaO_4$ and $InMnGaO_4$ were studied via synchrotron X-ray powder diffraction (SXPD). Figure 4.1 shows the SXPD patterns along with Rietveld refinement fits. As reported for analogous compounds, oxidation of $YbMnGaO_4$ induces a phase transition from the $R\bar{3}m$ to $P\bar{3}$ symmetry [45, 48–51]. In contrast, $InMnGaO_4$ retains the $R\bar{3}m$ symmetry even after heating to 600 °C, the temperature at which most analogues undergo full oxidation, showing only minor intensity variations.

Figure 4.2 shows the crystal structures of $YbMnGaO_4$ and its oxidized phase $YbMnGaO_{4.5}$ based on the Rietveld refinement results. $YbMnGaO_4$ adopts a hexagonal layered structure composed of edge-sharing YbO6 octahedral layers (dark blue) alternating with double Mn/Ga-O bipyramidal layers (light blue). Upon oxidation, additional oxygen atoms are incorporated into the Mn/Ga-O layers, leading to a change in coordination and local disorder. The refined parameters are summarized in Table 4.1. The structural model was based on the previously reported $LuMnGaO_4$ refinement [51], where the z-coordinate of Lu was slightly displaced from the special position (0, 0, 0). For the oxidized phase, we did not use the model of $LuMnGaO_{4.5}$ where the oxygen positions were shifted from their original positions because X-ray diffraction has limited sensitivity to light elements compared to neutron diffraction. Also, isotropic thermal displacement parameter (U_{iso}) were fixed to that of the $LuMnGaO_4$ values to avoid nonphysical results.

In situ X-ray diffraction experiments on $YbMnGaO_4$ further revealed the temperature-

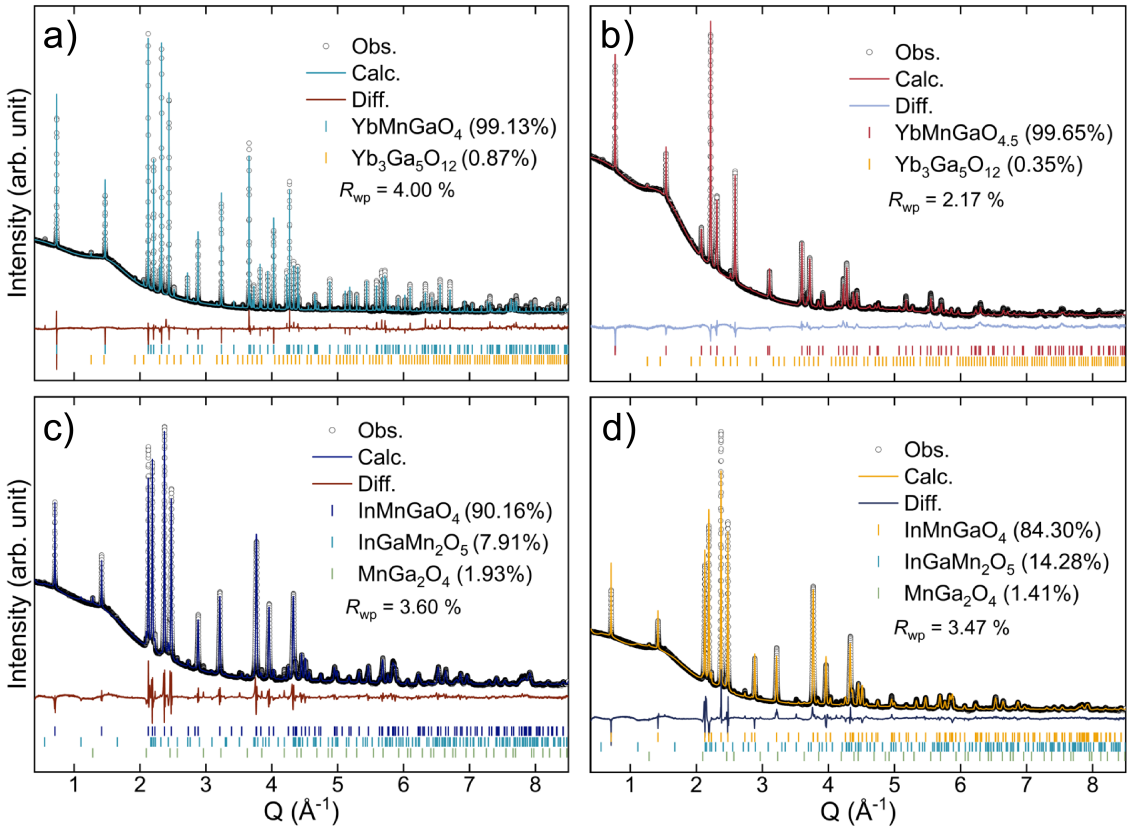


Figure 4.1: SXPD patterns with Rietveld fits for (a) $YbMnGaO_4$, (b) $YbMnGaO_{4.5}$, (c) $InMnGaO_4$, and (d) $InMnGaO_4$ heated at 600 °C.

dependent phase evolution (Figure 4.3). A gradual change in diffraction intensities begins around 250 °C, followed by a distinct transformation near 300 °C. These results confirm a single-step transition from the reduced $R\bar{3}m$ to the oxidized $P\bar{3}$ phase without observable intermediate phases.

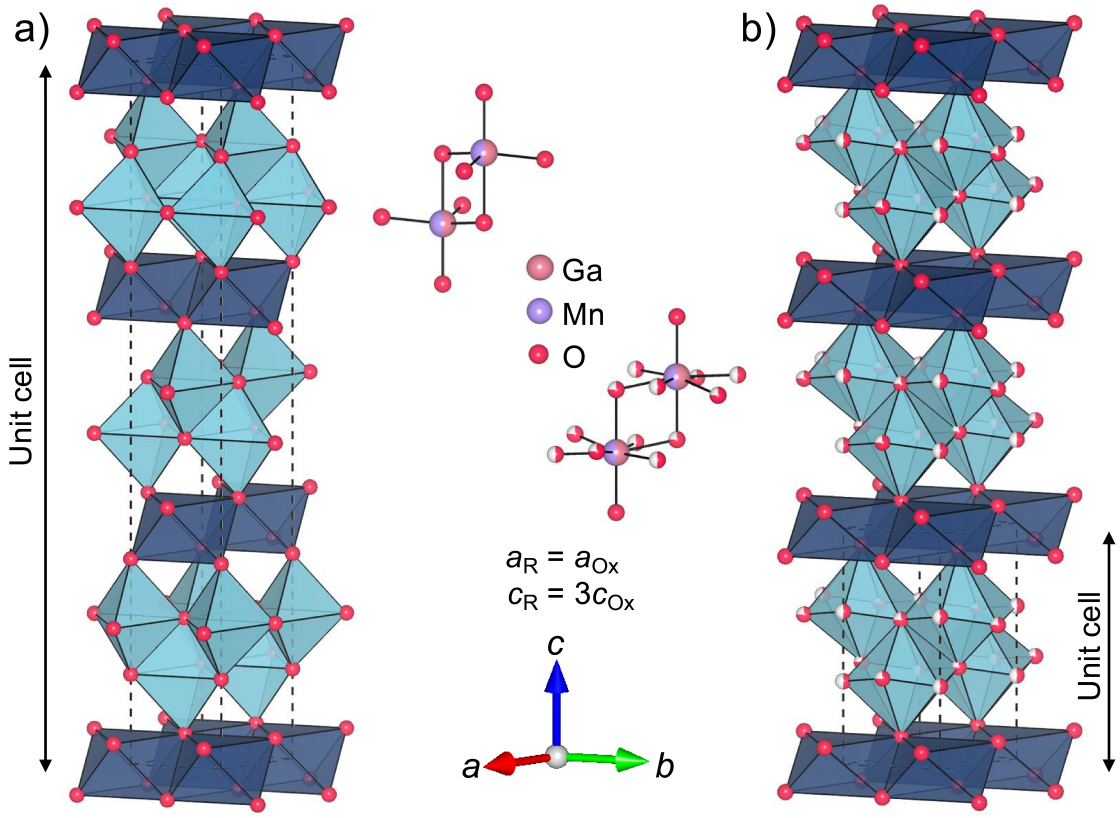


Figure 4.2: The unit cell of the crystal structure of (a) $YbMnGaO_4$ and (b) $YbMnGaO_{4.5}$. For $YbMnGaO_{4.5}$, three unit cells are drawn for comparison to the reduced phase. The change in the double Mn/Ga-O layer is drawn in the middle.

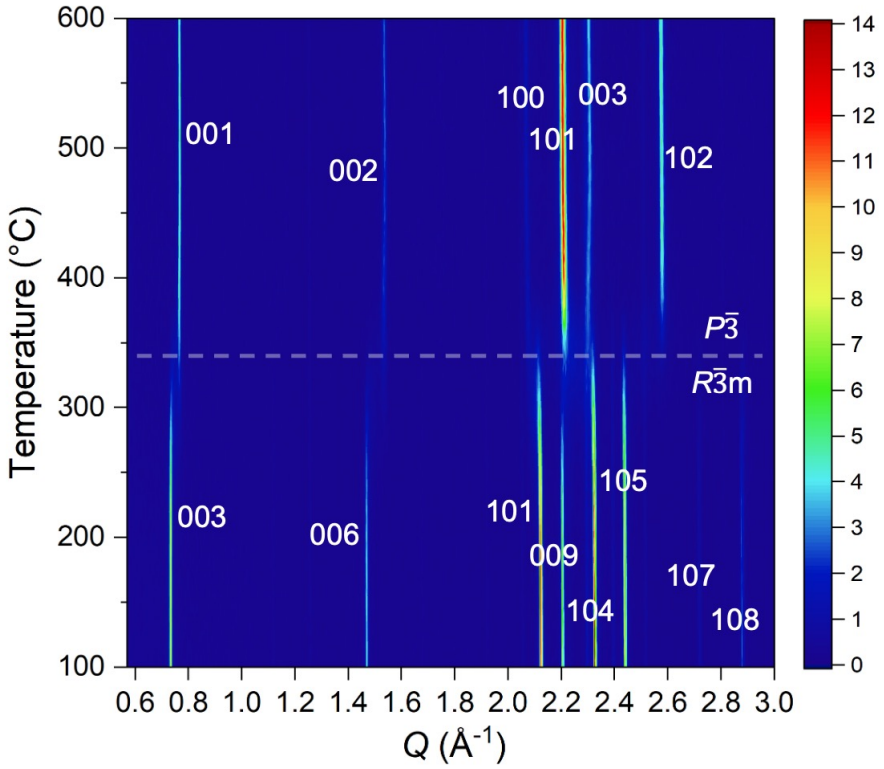


Figure 4.3: In situ SXPD contour plot of $YbMnGaO_4$ heated in air from 25 °C to 700 °C, showing the evolution of diffraction peaks associated with the structural transition from $R\bar{3}m$ to $P\bar{3}$ phase. Indexed reflections are labeled for each phase.

Table 4.1: Structural parameters obtained from Rietveld refinement of SXPD data for $YbMnGaO_4$, $YbMnGaO_{4.5}$, $InMnGaO_4$, and annealed $InMnGaO_4$, measured at 300K.

$YbMnGaO_4$	Atom	Wyc. Pos.	x	y	z	Site Occ.	U_{iso}
$R\bar{3}m$	Yb	6c	0	0	0.00396(7)	0.5	0.0047
$a = b = 3.43817(1)$ Å	Mn	6c	0	0	0.21608(4)	0.5	0.0045
$c = 25.63143(9)$ Å	Ga	6c	0	0	0.21608(4)	0.5	0.0045
α = β = 90° γ = 120°	O1	6c	0	0	0.1286(2)	1	0.0267
vol = 262.397(1) Å^3	O2	6c	0	0	0.2900(2)	1	0.0267
$R_{wp} = 4.00$ %							
$YbMnGaO_{4.5}$	Atom	Wyc. Pos.	x	y	z	Site Occ.	U_{iso}
	Yb	2c	0	0	0.0150(3)	0.5	0.0148
$P\bar{3}$	Mn	2d	0.66667	0.33333	0.351(4)	0.5	0.019
$a = b = 3.49211(5)$ Å	Ga	2d	0.66667	0.33333	0.351(4)	0.5	0.019
$c = 8.1513(1)$ Å	O1	2d	0.66667	0.33333	0.1097(8)	1	0.0203
α = β = 90° γ = 120°	O2	2d	0.33333	0.66667	0.395(2)	0.7411	0.011
vol = 86.086(1) Å^3	O3	2c	0	0	0.352(1)	0.5089	0.002
$R_{wp} = 2.17\%$							
$InMnGaO_4$	Atom	Wyc. Pos.	x	y	z	Site Occ.	U_{iso}
	In	6c	0	0	0.0022(2)	1	0.0063(1)
$R\bar{3}m$	Mn	6c	0	0	0.21867(3)	0.5	0.0063(1)
$a = b = 3.33204(2)$ Å	Ga	6c	0	0	0.21867(3)	0.5	0.0063(1)
$c = 26.5725(3)$ Å	O1	6c	0	0	0.1274(2)	1	0.041(2)
α = β = 90° γ = 120°	O2	6c	0	0	0.2938(2)	1	0.019(1)
vol = 255.497(4) Å^3							
$R_{wp} = 3.60$ %							
InMnGaO4 annealed at 600°C	Atom	Wyc. Pos.	x	y	z	Site Occ.	U_{iso}
	In	6c	0	0	0.00755(7)	0.5	0.0082(2)
$R\bar{3}m$	Mn	6c	0	0	0.21944(4)	0.5	0.0082(2)
$a = b = 3.33009(4)$ Å	Ga	6c	0	0	0.21944(4)	0.5	0.0082(2)
$c = 26.5284(5)$ Å	O1	6c	0	0	0.1336(2)	1	0.042(1)
α = β = 90° γ = 120°	O2	6c	0	0	0.2891(2)	1	0.019(1)
vol = 254.773(8) Å^3							
$R_{wp} = 3.47$ %							

4.3.2 Oxygen storage properties

The oxygen uptake behavior of $YbMnGaO_4$ and $InMnGaO_4$ was evaluated by thermogravimetric analysis (TGA) under flowing air (Figure 4.4). $YbMnGaO_4$ exhibits a distinct weight gain beginning at approximately 250 °C, comparable to the behavior observed for $LuMnGaO_4$ [51]. The total mass increase of 2.6(4) % corresponds to the incorporation of 0.6 oxygen atoms per formula unit. Assuming full oxidation of Mn^{2+} to Mn^{3+}, the resulting composition can be expressed as $YbMnGaO_{4.5}$. The slightly higher experimental oxygen content likely arises from a small initial oxygen deficiency in the reduced phase ($YbMnGaO_{4-\delta}$). The temperature-dependent oxidation trend aligns well with the structural transformation seen in the in situ SXPD data (Figure 4.3).

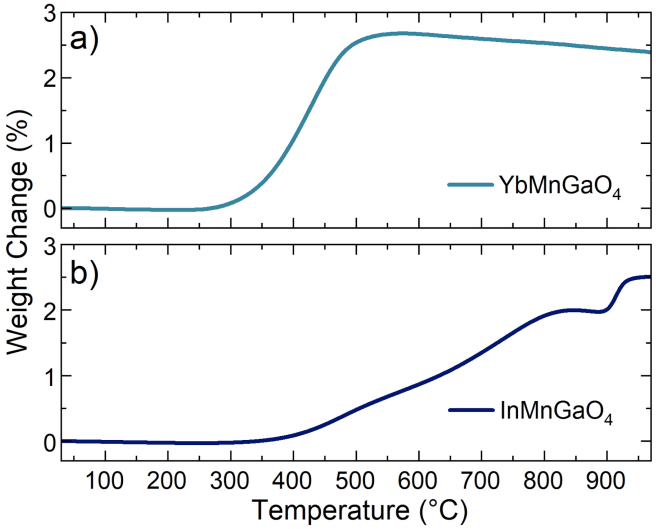


Figure 4.4: TGA of $YbMnGaO_4$ (a) and $InMnGaO_4$ (b) measured in air.

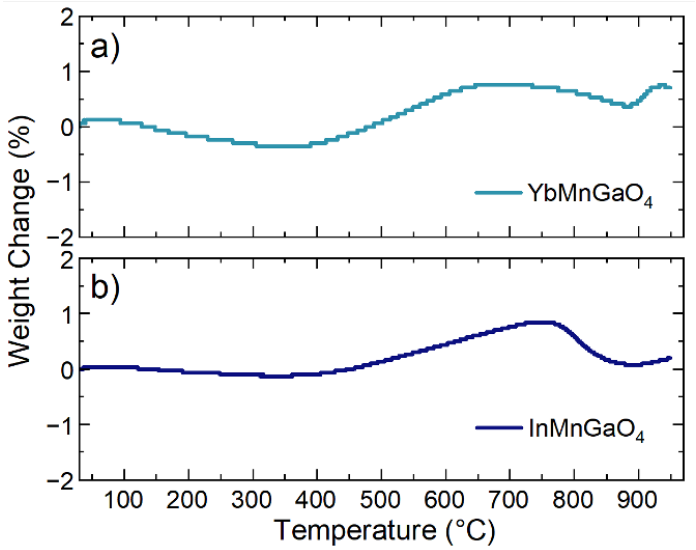


Figure 4.5: TGA of $YbMnGaO_4$ (a) and $InMnGaO_4$ (b) measured under nitrogen.

In contrast, $InMnGaO_4$ displays different behavior. The SXPD patterns remain unchanged up to 600 °C (Figure 4.1d), suggesting that the phase does not accommodate oxygen intercalation. Nevertheless, the TGA profile reveals a slow, continuous mass increase starting at approximately 350 °C, with a steady rise up to 800 °C, a short plateau until 900 °C, and another increase, thereafter, reaching a total weight gain of 2.5% by 1000 °C. To verify that the weight gain was specifically due to reaction with air, rather than inherent instability, measurements were repeated under flowing nitrogen. As shown in Figure 4.5, both $YbMnGaO_4$ and $InMnGaO_4$ exhibit a weight change of less than 1% up to 950 °C. The fluctuations observed are likely due to instrumental noise or buoyancy effects.

To understand the behavior of $InMnGaO_4$, ex situ XRD was performed on $InMnGaO_4$ samples annealed at 25 °C, 600 °C, 750 °C, 800 °C, 830 °C, and 950 °C in air (Figure 4.6). Up to 750 °C, only intensity changes are observed without peak shifts, confirming phase stability. At 800 °C, new reflections emerge, and by 830 °C the diffraction pattern changes dramatically, indicating decomposition of the $R\bar{3}m$ phase. At 950 °C, most of the original $InMnGaO_4$ reflections disappear.

These results indicate that $InMnGaO_4$ does not absorb oxygen into its lattice. Instead, the gradual weight increase in TGA likely originates from surface oxidation reactions. Between 800 °C and 830 °C, the compound undergoes decomposition, forming a secondary phase that remains stable up to 1000 °C. Preliminary indexing of this new phase suggests orthorhombic symmetry (possible $Fddd$, $Pccn$, and $P222$ space groups), but no isostructural analogues were identified (Figures 4.7 and 4.9). Further structural determination will require complementary diffraction or spectroscopic analysis.

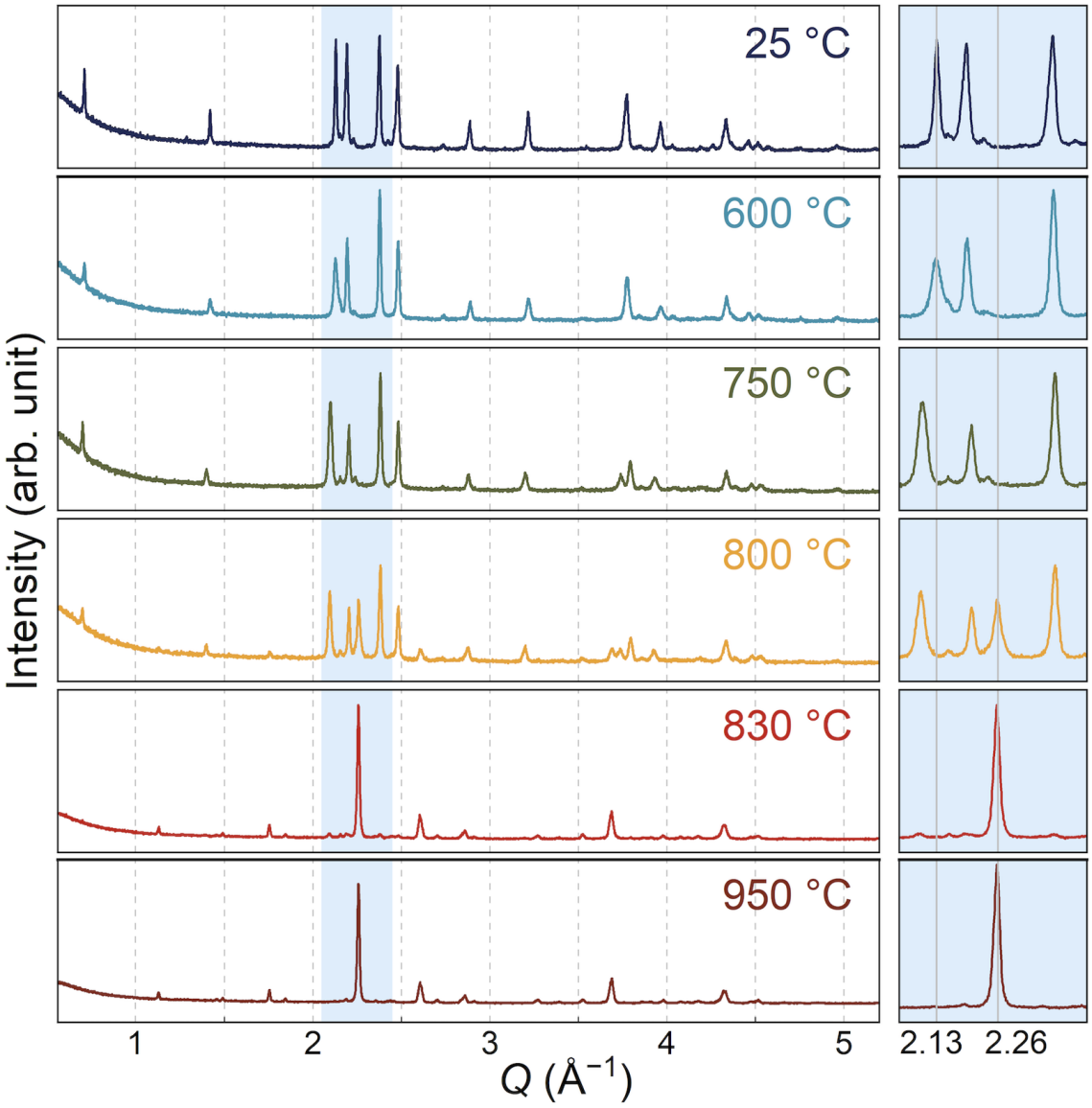


Figure 4.6: Ex situ laboratory X-ray diffraction measurements of $InMnGaO_4$ annealed at 25 °C, 600 °C, 750 °C, 800 °C, 830 °C, and 950 °C. The Q range from 2.1 $Å^1$ to 2.4 $Å^1$ is highlighted on the right, showing a new peak arising at 800 °C and the pattern completed changing from 830 °C.

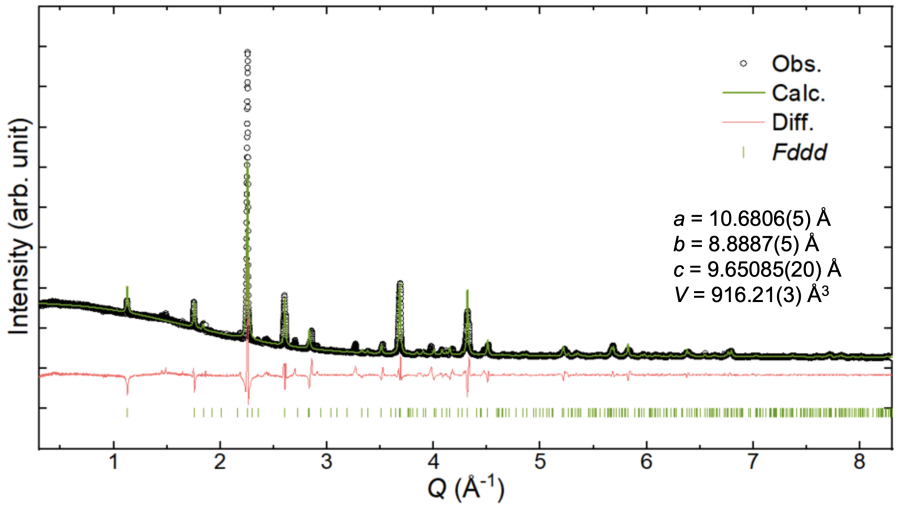


Figure 4.7: Le Bail fit of the $InMnGaO_4$ sample heated at 950 °C using the $Fddd$ structural model. The experimental (black circles), calculated (green line), and difference (red line) profiles are shown. Vertical green ticks mark Bragg reflections indexed to the $Fddd$ phase. Refined lattice parameters: $a = 10.6806(5)$ Å, $b = 8.8887(5)$ Å, $c = 9.65085(20)$ Å, $V = 916.21(3)$ Å^3

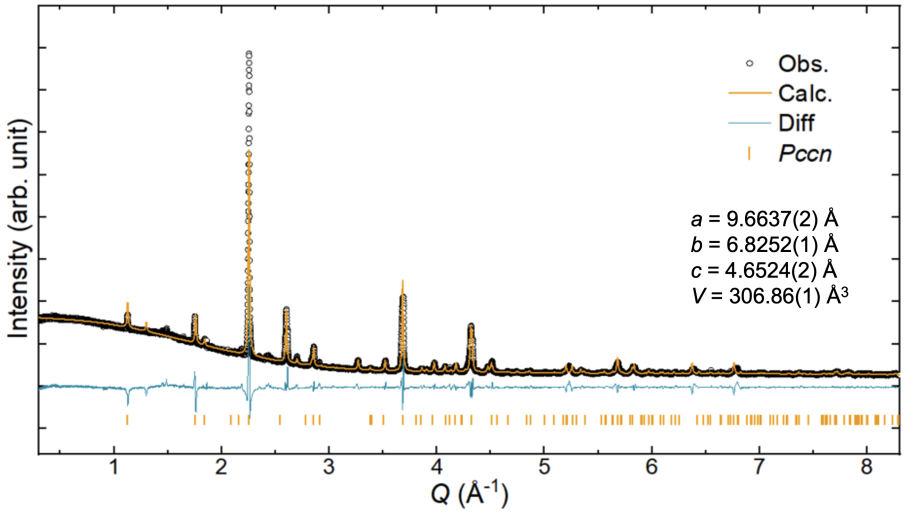


Figure 4.8: Le Bail fit of the $InMnGaO_4$ sample heated at 950 °C using the $Pccn$ structural model. The experimental (black circles), calculated (orange line), and difference (blue line) profiles are shown. Vertical orange ticks mark Bragg reflections indexed to the $Pccn$ phase. Refined lattice parameters: $a = 9.6637(2)$ Å, $b = 6.8252(1)$ Å, $c = 4.6524(2)$ Å, $V = 306.86(1)$ Å^3.

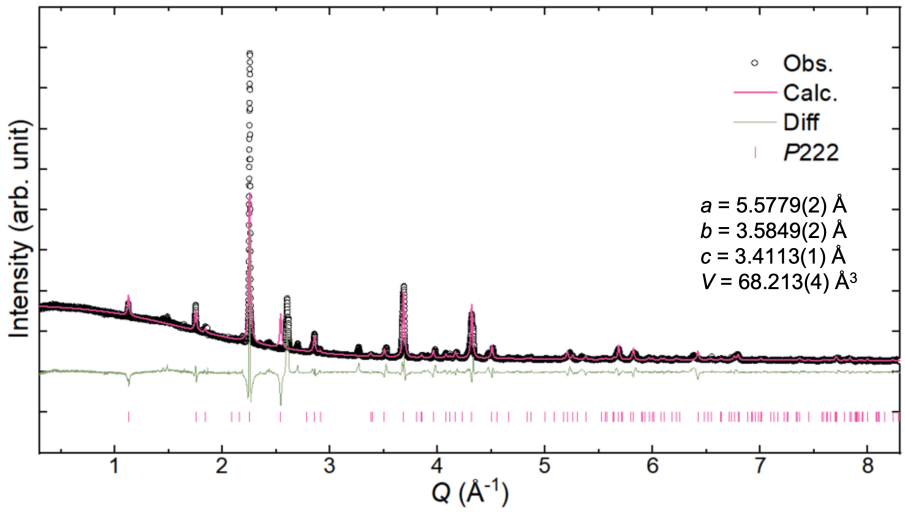


Figure 4.9: Le Bail fit of the $InMnGaO_4$ sample heated at 950 °C using the *P*222 structural model. The experimental (black circles), calculated (pink line), and difference (green line) profiles are shown. Vertical pink ticks mark Bragg reflections indexed to the *P*222 phase. Refined lattice parameters: $a = 5.5779(2)$ Å, $b = 3.5849(2)$ Å, $c = 3.4113(1)$ Å, $V = 68.213(4)$ Å^3.

4.3.3 Origin of the distinct behavior of $InMnGaO_4$

Previous studies on the AFe_2O_4 series (*A* = Lu, Yb, Y, In) demonstrated that all compounds reversibly absorb and release oxygen except for $InFe_2O_4$ [48]. Under O_2/He – H_2/He cycling, Lu-, Yb-, Y- analogue phases retained structural reversibility, whereas $InFe_2O_4$ degraded under reducing conditions. The behavior of $InMnGaO_4$ observed here is therefore consistent with the anomalous nature of indium-containing analogues.

Although $InMnGaO_4$ adopts the same nominal $R\bar{3}m$ structure, the post-transition metal nature of In^{3+} imparts distinct bonding characteristics. The smaller ionic radius of In^{3+} (0.80Å)[7] compared with Yb^{3+} (0.868Å)[7] or Lu^{3+} (0.861Å)[7] leads to shorter In-O bonds and a contracted lattice in the ab plane. The bond lengths are labeled in Figures 4.10 and 4.11. As summarized in Table 4.1, $YbMnGaO_4$ has $a = b = 3.44$ Å, while $InMnGaO_4$ exhibits $a = b = 3.33$ Å. Despite a slightly larger *c*-parameter, the overall cell volume of

$InMnGaO_4$ is smaller. The resulting rigid bonding network likely hinders oxygen insertion into the double Mn/Ga-O layers, whereas the more flexible framework of $YbMnGaO_4$ accommodates oxygens more readily.

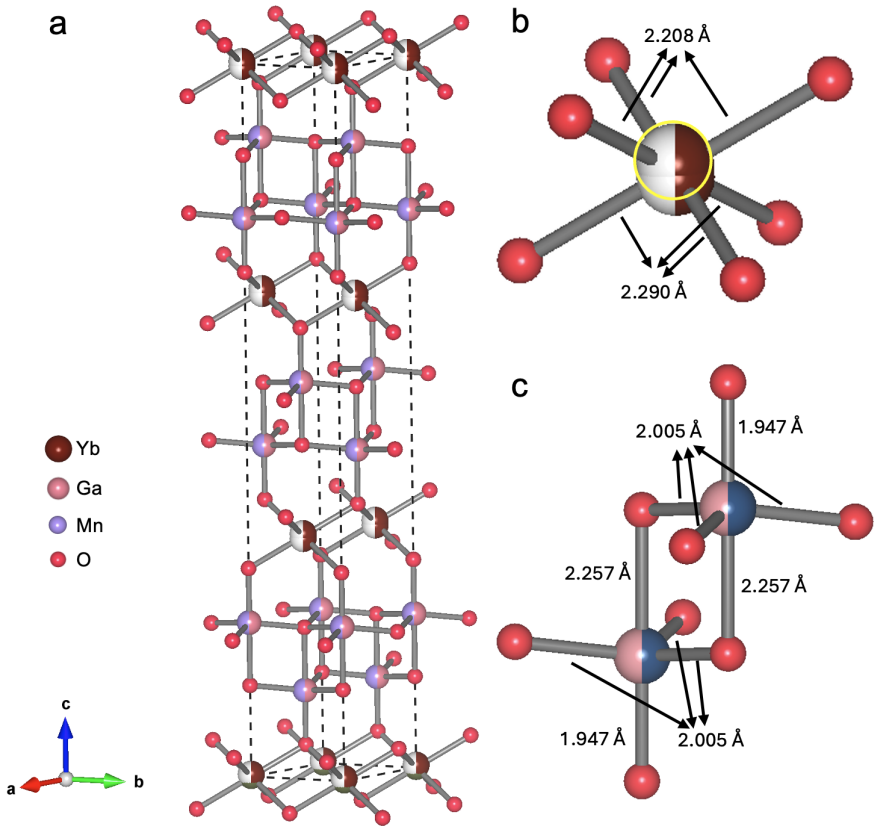


Figure 4.10: Crystal structure of $YbMnGaO_4$. (a) The unit cell of $YbMnGaO_4$ viewed along the *c*-axis, showing alternating layers of YbO6 octahedra and Mn/GaO5 polyhedra. Yb, Ga, Mn, and O atoms are represented by brown, pink, purple, and red spheres, respectively. (b) Local coordination environment of Yb, forming a slightly distorted YbO6 octahedron with individual Yb-O bond lengths labeled. (c) The Mn/Ga-O5 double bipyramidal structure, where Mn and Ga share the same crystallographic site; all Mn/Ga-O bond lengths are labeled.

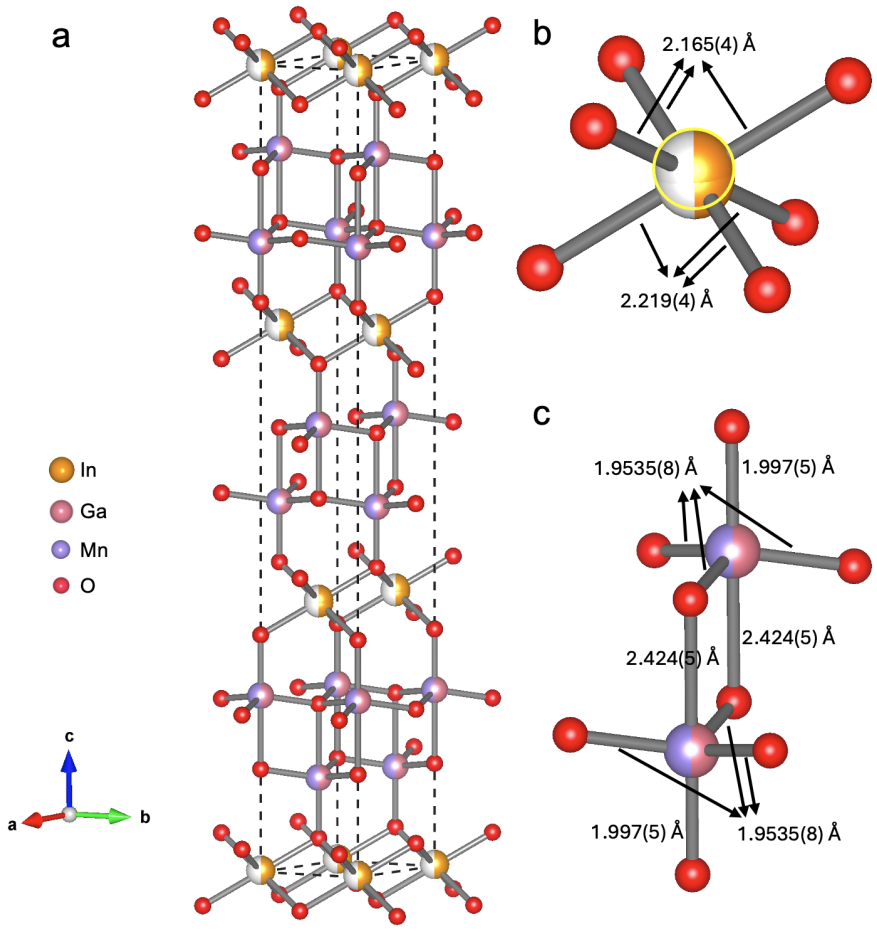


Figure 4.11: Crystal structure of $InMnGaO_4$. (a) The unit cell of $InMnGaO_4$ viewed along the *c*-axis, showing alternating layers of InO6 octahedra and Mn/GaO5 polyhedra. In, Ga, Mn, and O atoms are represented by gold, pink, purple, and red spheres, respectively. (b) Local coordination environment of In, forming a slightly distorted InO6 octahedron with all In-O bond lengths labeled. (c) The Mn/Ga-O5 double bipyramidal structure, where Mn and Ga share the same crystallographic site; all Mn/Ga-O bond lengths are labeled.

4.3.4 Oxidation states and magnetism

The oxidation states of magnetic ions (Yb^{3+} and $Mn^{2+/3+}$) in $YbMnGaO_4$, $YbMnGaO_{4.5}$, and $InMnGaO_4$ were confirmed through temperature-dependent magnetic susceptibility measurements. As shown in Figure 4.12, $YbMnGaO_4$ exhibits simple paramagnetic behavior, whereas the oxidized phase $YbMnGaO_{4.5}$ shows the onset of antiferromagnetic order with a Néel temperature (T_N) of 11 K.

To determine the oxidation states, we analyzed the magnetic data using the Curie-Weiss law (Eq. (4.1)) which describes how magnetic moments in a paramagnet tend to align with an externally applied field [102].

$$\chi = \frac{C}{T - \theta_{\mathrm{CW}}} \tag{4.1}$$

χ	magnetic susceptibility
C	Curie constant
T	absolute temperature
θ_{CW}	Curie-Weiss temperature

By inverting the susceptibility, we obtained a linear relationship for χ^{-1} vs. T, allowing for the determination of C and θ_{CW}. In this form, the slope is $1/C$ and the y-intercept is $-\theta_{\mathrm{CW}}/C$.

$$\chi^{-1} = \frac{T - \theta_{\mathrm{CW}}}{C} = \frac{T}{C} - \frac{\theta_{\mathrm{CW}}}{C} \tag{4.2}$$

The Curie constant is directly related to the number of unpaired electrons, and it can be used

to calculate the effective magnetic moment per ion in units of Bohr magnetons, μ_B.

$$\mu_{\text{eff}} = \sqrt{8C}\mu_B \tag{4.3}$$

This value can be compared to the calculated effective magnetic moment,

$$\mu_{\text{cal}} = g_J\sqrt{J(J+1)}\mu_B \tag{4.4}$$

where, g_J denotes the Landé g-value with an equation,

$$g_J = \frac{3}{2} + \frac{S(S+1) - L(L+1)}{2J(J+1)} \tag{4.5}$$

where S, L, and J represent the spin quantum number, orbital quantum number, and total angular momentum, respectively. In $3d$ transition metals, the magnetic properties are primarily dictated by the valence electrons within the partially filled d shells, which are the outermost orbitals that contribute to chemical bonding. These electrons interact strongly with surrounding ligands or ions in a crystal lattice that it "quenches" the orbital angular momentum, making $L = 0$ [102]. In this case, since $J = S + L$, J essentially becomes equal to the spin S. Substituting $J = S$ into Eq. (4.4), we derive the following approximation:

$$\mu_s = \sqrt{4S(S+1)}\mu_B \tag{4.6}$$

For $YbMnGaO_4$ and its oxidized phase, the total theoretical magnetic moment is derived by considering the individual contributions of the magnetic ions, assuming they act as independent centers:

$$\mu_{\text{eff}} = \sqrt{\mu_{\text{eff},1}^2 + \mu_{\text{eff},2}^2}\mu_B \tag{4.7}$$

Using theoretical values of 4.54 μ_B for Yb^{3+}, 5.92 μ_B for Mn^{2+}, and 4.90 μ_B for Mn^{3+}, we

calculate expected moments of 7.46 μ_B for and 6.68 μ_B for $YbMnGaO_{4.5}$.

We performed Curie-Weiss fits on the χ^{-1} versus T plots for $YbMnGaO_4$ and $YbMnGaO_{4.5}$ within the 150 K–300 K temperature range, where a linear regime is clearly observed. The experimental effective magnetic moments, derived from the resulting Curie constants, show excellent agreement with the theoretical values: 7.578(5) μ_B for $YbMnGaO_4$ and 6.734(3) μ_B for $YbMnGaO_{4.5}$ (Figure 4.12). These values confirm the respective oxidation states of the Yb and Mn ions in both compounds.

For $InMnGaO_4$, only manganese is the magnetically active ion in the compound. We compared the experimental μ_{eff} to the theoretical value for Mn^{2+} (5.92 μ_B). Magnetic susceptibility measurements were collected at applied fields of 100 Oe and 1000 Oe; we utilize the 1000 Oe data for fitting due to the improved signal-to-noise ratio and enhanced dipole alignment. As shown in Figure 4.13, the fit yielded an effective moment of 5.749 μ_B in the 180 K – 300 K linear regime, confirming the 2+ oxidation state for Mn.

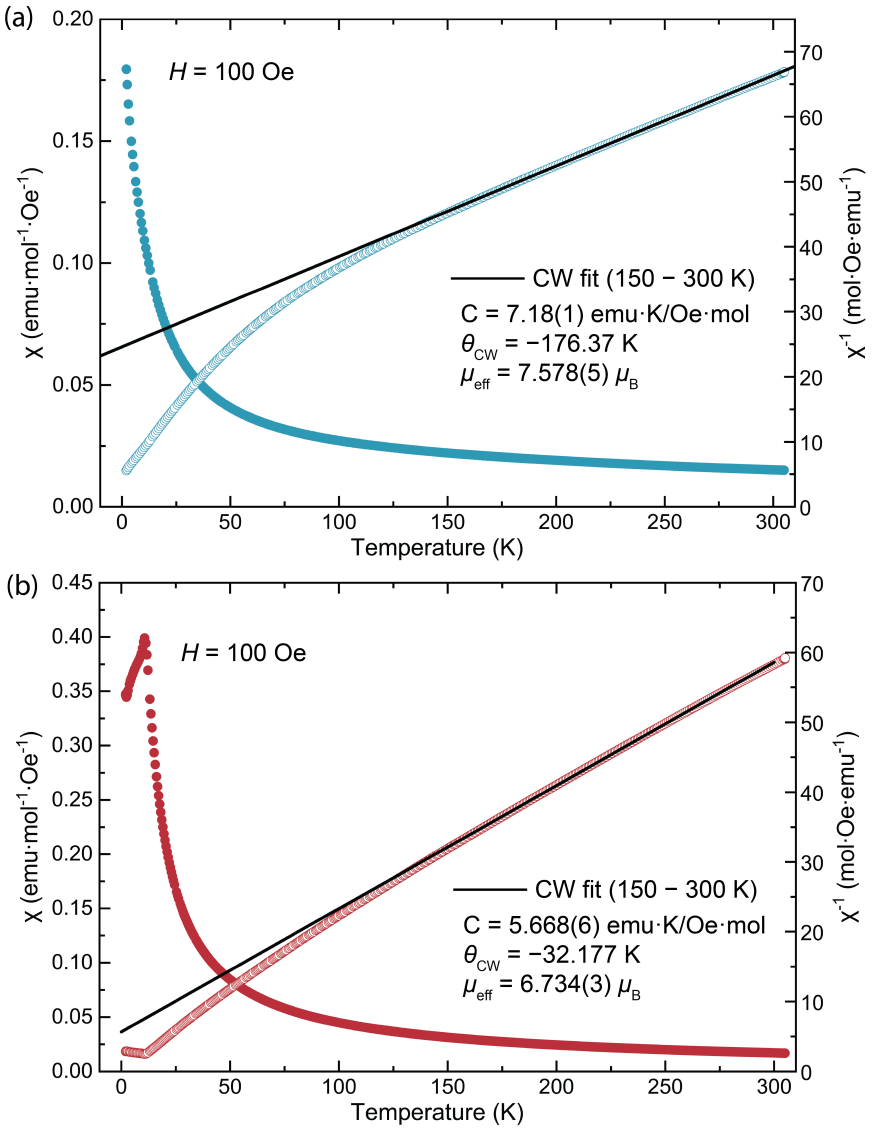


Figure 4.12: Temperature-dependent magnetic susceptibility of (a) $YbMnGaO_4$ and (b) $YbMnGaO_{4.5}$ measured under zero field cooled (ZFC) conditions in an applied field of $H = 100$ Oe. The left axis and filled symbols represent the magnetic susceptibility (χ) and the right axis and open symbols represent inverse magnetic susceptibility (χ^{-1}). The solid black lines represent the Curie-Weiss (CW) fits, performed over the temperature range of 150 K − 299 K.

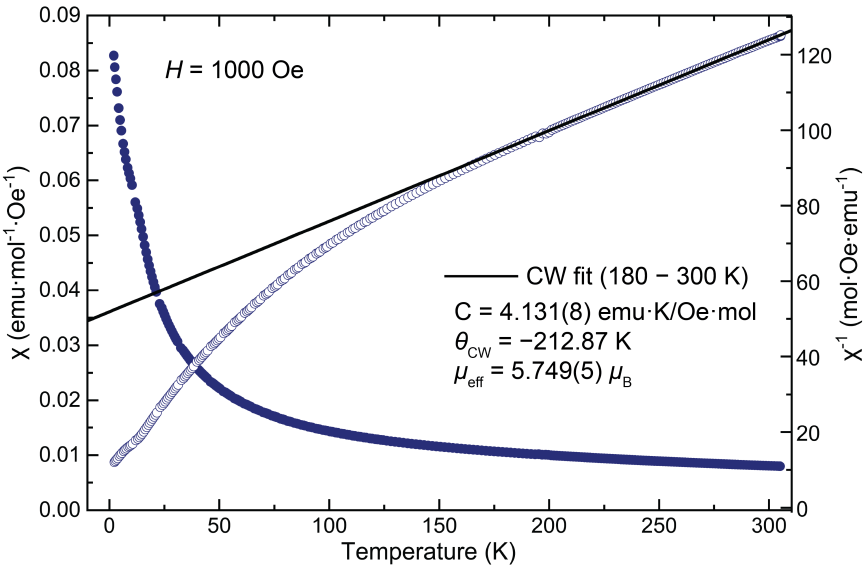


Figure 4.13: Temperature-dependent magnetic susceptibility of $InMnGaO_4$ measured under zero field cooled (ZFC) conditions in an applied field of $H = 1000$ Oe. The left axis and filled symbols represent the magnetic susceptibility (χ) and the right axis and open symbols represent inverse magnetic susceptibility (χ^{-1}). The solid black line represents the Curie-Weiss (CW) fit, performed over the temperature range of 180 K − 299 K.

Although our experimental data generally aligned with the Curie-Weiss law, we observed that the χ^{-1} versus T plots did not exhibit perfect linearity, instead displaying a slight positive curvature. To investigate whether this behavior originated from a temperature-independent contribution to magnetic susceptibility (χ_0), we applied a modified form of the Curie-Weiss law:

$$\chi = \frac{C}{T-\theta_{\mathrm{CW}}} + \chi_0, \quad \chi^{-1} = \frac{T-\theta_{\mathrm{CW}}}{\chi_0 \cdot (T-\theta_{\mathrm{CW}}) + C} \tag{4.8}$$

This temperature-independent term (χ_0) accounts for several underlying physical phenomena: core diamagnetism, Pauli paramagnetism, or van Vleck paramagnetism [102]. Core diamagnetism is present in all materials, its magnitude is typically negligible compared to the paramagnetic signal of materials with unpaired electrons. It is only relevant

to materials that has diamagnetism as the only contributor or insulators with no unpaired electrons. Pauli paramagnetism [103] is characteristic of metals and arises from the spin imbalance of conduction electrons in an applied field, whereas Van Vleck paramagnetism arises from the Zeeman-induced mixing of ground and excited electronic states [103, 104].

In our compounds, the χ^{-1} vs. T plots exhibit a slight positive curvature at lower temperatures, deviating marginally from strict linearity. To test whether this curvature originated from temperature-independent contributions, we performed fits using the modified Curie-Weiss model. However, the parameters derived from these fits were physically inconsistent with the expected electronic configurations of our compounds. This discrepancy confirms that χ_0 contributions in our samples are sufficiently small to be neglected, and that the standard Curie-Weiss model provides the most accurate and physically meaningful description of the magnetic behavior in these systems.

Beyond this Curie-Weiss analysis, it is important to note that the downward curvature at lower temperatures in χ^{-1} is commonly attributed to short-range spin correlations. This can be found in Figure 4.12(a) for $YbMnGaO_4$ below 150 K. Furthermore, the large negative Curie-Weiss temperature ($\theta_{CW} = -176.37$ K) indicates strong antiferromagnetic (AFM) exchange interactions, where the spin configuration is driven toward an antiparallel arrangement. Such substantial negative θ_{CW} value is a hallmark of geometric frustration, particularly in systems where $S = 1/2$ ions are arranged on a triangular lattice. Similar trend can be found for $InMnGaO_4$ in Figure 4.13.

To quantify frustration in antiferromagnetic materials, we can use the frustration index ($f = -\theta_{CW}/T_N$, where T_N is the magnetic transition temperature). A value of $f > 1$ is accepted as an indicator of significant geometric frustration [105]. For $YbMnGaO_{4.5}$, using $\theta_{CW} = -32.18$ K and $T_N \approx 11$ K, we obtain $f \approx 2.9$, which definitively indicates a frustrated ground state.

Given the compelling magnetic behavior of the Yb-based compounds, we further ex-

amined their susceptibility using both Zero-Field Cooled (ZFC) and Field Cooled (FC) protocols under applied fields of 100 Oe and 1000 Oe. While $YbMnGaO_4$ displays identical trends in both ZFC and FC conditions, $YbMnGaO_{4.5}$ shows a clear divergence between the two at low temperatures. Additionally, the Néel temperature in $YbMnGaO_{4.5}$ shifts to approximately 8 K under a 1000 Oe field. This divergence between ZFC and FC conditions, coupled with the field-dependent shift in T_N, is a characteristic signature of spin-glass behavior. To further elucidate the magnetic structure of these materials, we conducted neutron diffraction measurements.

We performed neutron diffraction measurements on both $YbMnGaO_4$ and $YbMnGaO_{4.5}$ at different temperatures. For $YbMnGaO_4$, the diffraction patterns at 300 K and 7 K remain nearly identical, with the exception of a broad feature emerging in the low-Q region (1.2 $-$ 1.4 Å^{-1}) at 7 K (Figure 4.15). Notably, no new sharp magnetic Bragg reflections were observed at 7 K. This feature indicates the development of short-range magnetic correlations, consistent with the susceptibility data suggesting a magnetically frustrated state.

For the oxidized phase, $YbMnGaO_{4.5}$, the diffraction data were collected at 300 K, 20 K, and 7 K (Figure 4.16). While the structural Bragg reflections remain invariant across this temperature range, a notable broad diffuse feature emerges at $Q = 0.6$–0.9 Å^{-1} upon cooling to 7 K. No new sharp magnetic Bragg reflections were observed at 7 K. The appearance of this broad diffuse feature, rather than sharp magnetic peaks, confirms the presence of short-range magnetic correlations rather than long-range order. This observation directly corroborates the divergence between the Zero-Field Cooled (ZFC) and Field Cooled (FC) susceptibility curves observed in the SQUID measurement in Figure 4.14(b). Together, these results indicate that the frustrated spins in $YbMnGaO_{4.5}$ do not undergo long-range ordering, but instead transition to a randomly frozen, spin-glass state below the transition temperature of 11 K.

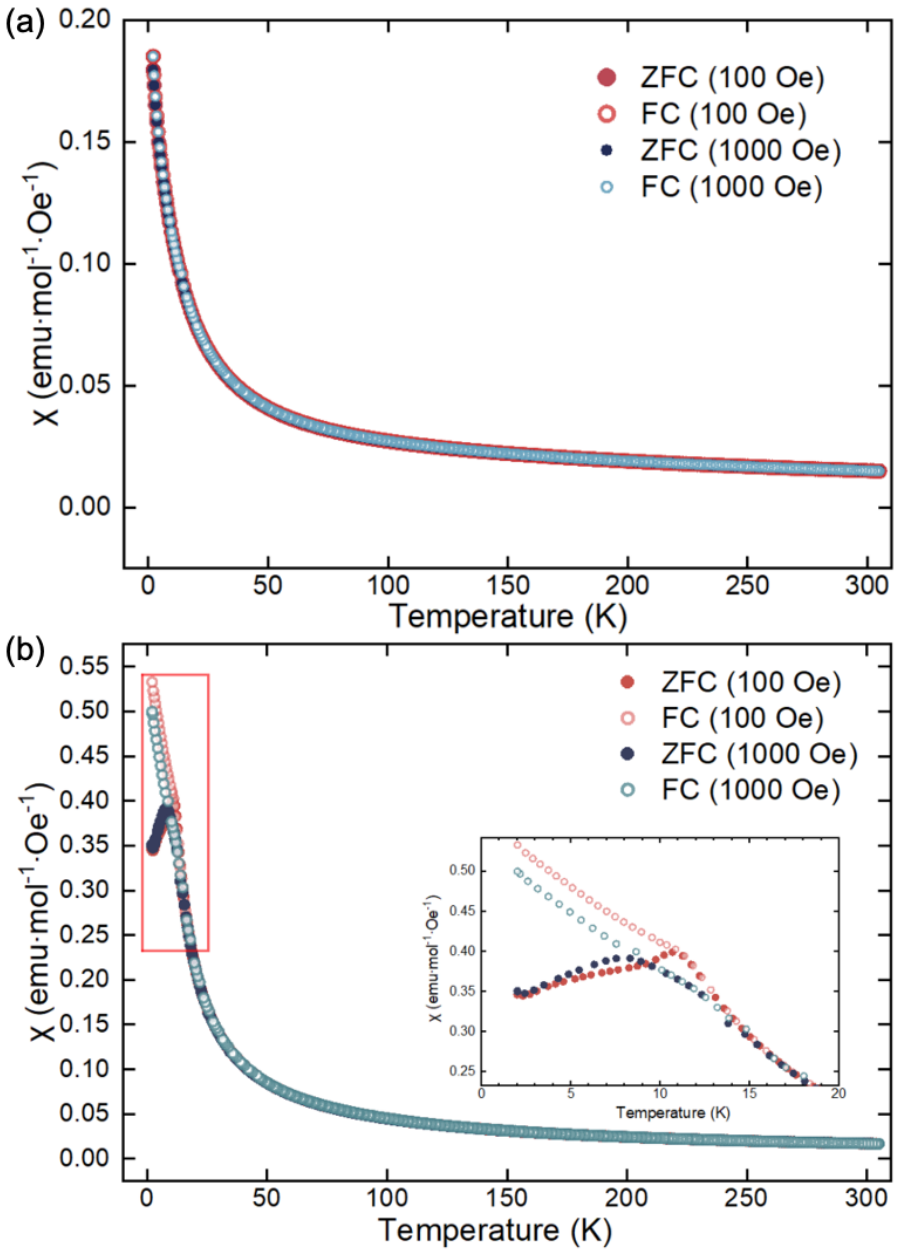


Figure 4.14: Temperature-dependent magnetic susceptibility (χ) for (a) $YbMnGaO_4$ and (b) $YbMnGaO_{4.5}$, measured under zero-field cooled (ZFC, solid circles) and field cooled (FC, open circles) conditions at 100 Oe (red) and 1000 Oe (blue). The inset in (b) shows a magnified view of the low-temperature region, marked by the red rectangle in the main panel, between 0 K and 20 K.

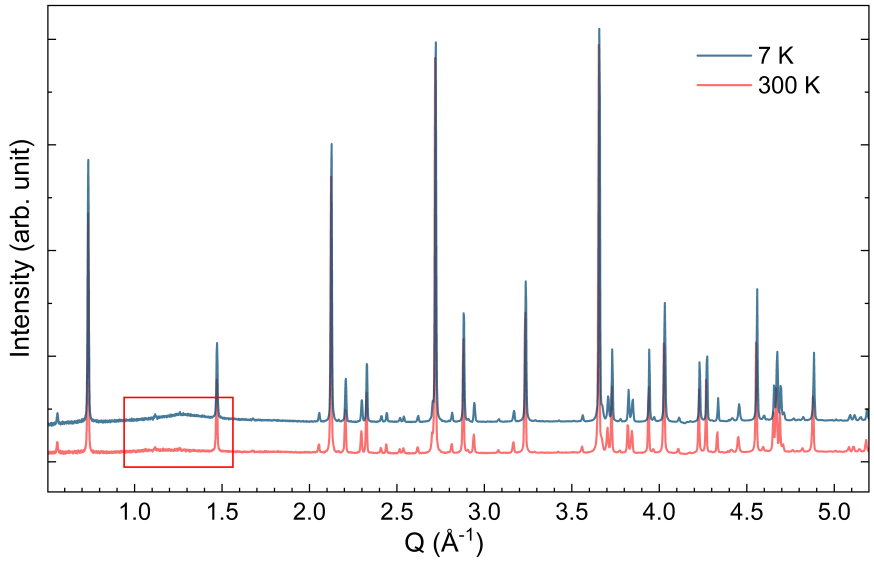


Figure 4.15: Neutron powder diffraction patterns of $YbMnGaO_4$ from POWGEN, ORNL, meausured at 7 K and 300 K. The red box highlights a broad peak at 7 K (Q = 1.2 − 1.4 $Å^{-1}$) that is absent at 300 K.

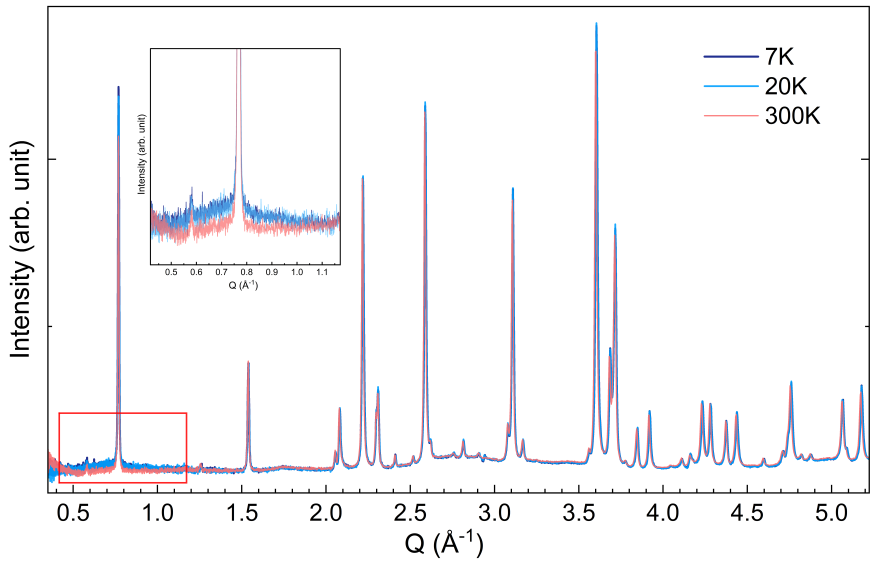


Figure 4.16: Neutron powder diffraction patterns of $YbMnGaO_{4.5}$ from POWGEN, ORNL, measured at 7 K, 20 K, and 300 K. The inset provides an enlarged view of the red box, which shows an emergence of a broad diffuse feature centered near $Q = 0.6 - 0.9$ $Å^{-1}$ under the (001) Bragg peak at low temperatures.

4.4 Conclusion

We investigated how variations in *A*-site cation chemistry influence the structural behavior and oxygen reactivity of layered $A\mathrm{MnGaO_4}$ oxides by comparing the Yb and In analogues. Using high-resolution synchrotron X-ray diffraction, thermogravimetric analysis, magnetic susceptibility measurements, and neutron diffraction, we established that subtle differences in *A*-site composition lead to markedly different structural and redox behaviors.

$\mathrm{YbMnGaO_4}$ behaves similarly to $\mathrm{LuMnGaO_4}$ in that they readily incorporates additional oxygen upon heating in air, accompanied by a crystallographic symmetry change from the $R\bar{3}m$ to the $P\bar{3}$ phase and the incorporation of approximately 0.6 oxygen atoms per formula unit to form $\mathrm{YbMnGaO_{4.5}}$. In contrast, $\mathrm{InMnGaO_4}$ maintains its original crystal structure over a wide temperature range and does not exhibit oxygen insertion into the lattice. Instead, thermal treatment at elevated temperatures eventually destabilizes the phase and produces a new crystalline product.

These contrasting behaviors arise from differences in the bonding characteristics of the *A*-site cations. The smaller ionic radius and stronger In–O bonding create a more rigid lattice that suppresses oxygen insertion, whereas the relatively more flexible Yb–O framework allows structural rearrangement and oxygen incorporation. This comparison demonstrates that *A*-site substitution can strongly influence lattice flexibility and oxygen mobility in layered $AB_2\mathrm{O_4}$-type oxides.

Magnetic characterization using magnetic susceptibility measurements and neutron diffraction further revealed that the *Yb*-based phases exhibit complex low-temperature magnetic behavior. While the reduced phase appear to have a paramagnetic behavior, the Curie-Weiss analysis and neutron diffraction at low temperature suggest a short-range magnetic ordering. The oxidized phase develops frustrated magnetic interactions and transitions into a spin-glass state at low temperatures, consistent with the short-range

correlations observed in neutron diffraction measurements.

Overall, this study demonstrates that the selection of *A*-site cations provides an effective strategy for controlling both the redox chemistry and physical properties of layered oxide materials. Extending this approach to other rare-earth or post-transition-metal substitutions may provide broader insight into how lattice rigidity, bonding character, and electronic structure collectively govern oxygen exchange processes and emergent magnetic phenomena in complex oxides.

Chapter 5: Systematic Study of *A* and *B* site Substitutions in AB_2O_4 Oxides

5.1 Introduction

The functional properties of complex metal oxides are linked to the strategic arrangement of cations within the lattice. In the previous chapters, we explored the structural and magnetic implications of substituting ions in the hexagonal AB_2O_4-type materials. To further elucidate the role of these substitutions, it is important to examine parallel strategies employed in other oxide frameworks. The perovskite family is a well studied and widely used material for various energy-related applications, and therefore serves as a good comparison.

Perovskite-type oxides are named after $CaTiO_3$ and belong to a class of oxides with the common formula ABO_3 (*A* = rare- or alkaline-earth metal, *B* = transition metal). In its ideal cubic structure, *A*-site cations are located at the corners of the cube (0, 0, 0) and are 12-fold coordinated. The *B*-site cations occupy the body-centered position (1/2, 1/2, 1/2), sitting directly within an octahedron and the oxygen atoms are situated at the face-center positions (1/2, 1/2, 0), surrounding the *B*-cation to form the octahedral structure (Figure 5.1) [106].

Among this perovskite family, manganese-based perovskites ($LnMnO_3$), which share the chemistry of the Mn on the *B*-site that is central to this thesis, provide a strong comparative model to understand how the lattice engineering dictates properties. These materials have emerged as a compelling alternative to fluorite-structured ceria (CeO_2) in solar thermochemical water-splitting (STWS) applications, primarily due to their remarkable compositional flexibility [26, 107, 108].

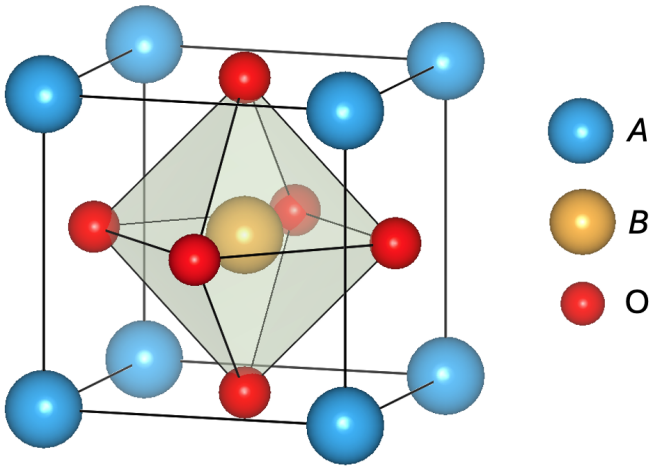


Figure 5.1: Crystal structure of a cubic perovskite (ABO_3).

Substitution at the *A*-site serves as a critical parameter for tailoring the thermodynamics involved in water-splitting cycles. The introduction of divalent cations, such as Sr^{2+} into $LaMnO_3$, facilitates the formation of oxygen vacancies (δ) and induces a mixed-valence state in the *B*-site transition metals [109, 110]. This $La_{1-x}Sr_xMnO_{3-\delta}$ system demonstrates significantly lowered reduction temperatures compared to binary metal oxides, thereby increasing the overall efficiency of solar collector systems [110].

The ionic radius of the *A*-site cation also impose significant structural constraints. Research has demonstrated that the ionic radius of the rare-earth (*Ln*) species governs the degree of octahedral distortion and the resulting tolerance factor [111]. Specifically, manganites with smaller rare-earth ions exhibit increased size disorder, which correlates with a significant reduction in the activation energy for CO_2 and H_2O splitting. These structural distortions are critical in maximizing the yields of O_2 and CO. [111].

While the *A*-site often controls the structural stability and vacancy concentration, *B*-site substitution modulates the redox kinetics and capacity. This is clearly evidenced in the $BaCeO_3$ and $BaMnO_3$ systems. While $BaCeO_3$ exhibits poor reduction and $BaMnO_3$ suffers from excessive reduction that hinders reoxidation, the synthesis of a solid solution,

$BaCe_{0.25}Mn_{0.75}O_3$, results in a material with excellent reduction capacity below 1400 °C and fast reoxidation kinetics [25]. Recent advancements have pushed toward concurrent substitutions at both sites, such as in the $Sr_xLa_{1-x}Mn_yAl_{1-y}O_{3-\delta}$ (SLMA) system [108, 112]. By simultaneously doping the *A*-site with Sr^{2+} and the *B*-site with Al^{3+}, researchers can stabilize the perovskite phase while precisely controlling the $Mn^{2+}/Mn^{3+}/Mn^{4+}$ ratios.

The perovskite systems discussed above primarily facilitate oxygen transport via a vacancy-mediated mechanism, where the lattice remains largely intact while oxygen ions migrate through vacancies. The hexagonal AB_2O_4 series investigated in this work, however, operates through a phase transition mechanism. In the latter, the material undergoes a structural transformation during the reduction and oxidation cycles to accommodate changes in oxygen stoichiometry. Despite these divergent pathways for oxygen exchange, the fundamental influence of cation substitution remains a common denominator. The strategic selection of *A*-site and *B*-site occupants governs the thermodynamic thresholds of these transitions and the structural stability of the resulting phases.

This chapter provides a systematic investigation into the $A^{3+}B^{2+}B'^{3+}O_4$ series, where $A =$ Lu, Yb, Er, Y; $B =$ Mn, Fe; and $B' =$ Fe, Ga. By utilizing a diverse range of rare-earth radii at the *A*-site and exploring the interplay between Mn and Fe/Ga at the *B*-sites, we aim to uncover the fundamental relationships between lattice geometry and oxygen storage behavior.

5.2 Experimental

5.2.1 Materials synthesis

AMnFeO$_4$ ($A =$ Lu, Yb, Er, Y), AFe$_2$O$_4$ ($A =$ Lu, Yb, Er), and AMnGaO$_4$ ($A =$ Lu, Yb) powders were all synthesized via high temperature solid-state reactions.

The starting reagents for AMnFeO$_4$ were stoichiometric amounts of A_2O_3, MnO, Fe_2O_3.

For AFe$_2$O$_4$, A_2O$_3$, Fe$_2$O$_3$ and Fe powder were used. For AMnGaO$_4$, A_2O$_3$, MnO, Ga$_2$O$_3$ were used. These reagents were ground using a mortar and pestle, then pressed into 13 mm pellets. The pellets were placed in a 2 mL alumina crucible which fits into a quartz ampoule (14 mm ID, 16 mm OD); the ampoule was then sealed under a vacuum of at least 7.5×10^{-3} Torr. The sealed ampoules were placed in a high-temperature furnace and heated to 1150–1180 °C at a heating rate of 5 °C/min for 12 hours, followed by an ice-bath quench. To oxidize these samples, the reduced phases were heated in ambient air at 550–650 °C for 12 hours. See Table 5.1 for detailed information of the reagents used in the syntheses.

Table 5.1: Reagent company and purity

Reagent	Company	Purity (%)
Lu_2O_3	MSE Supplies	99.995
Yb_2O_3	MSE Supplies	99.99
Y_2O_3	Sigma Aldrich	99.99
Er_2O_3	MSE Supplies	99.99
Fe_2O_3	Sigma Aldrich	≥99
Ga_2O_3	Sigma Aldrich	99.99
MnO	Alfa Aesar	99.99
Fe	Alfa Aesar	99.5

5.2.2 Thermogravimetric analysis (TGA)

TGA of the reduced phases were performed using a TA Instruments Discovery TGA-5500. Approximately 10 mg of each sample was loaded into platinum pans (100 μL) and heated under flowing air (25 mL/min) to 700 °C at a rate of 5 °C min^{-1}. Reduction experiments of the oxidized phases were tested under 3% H_2/Ar gas (25 mL/min) and

heated to 1000 °C at a rate of 5 °C min^{-1}. An instrumental error of 0.1 % was accounted for in all mass measurements.

5.2.3 X-ray diffraction (XRD)

Laboratory XRD data were collected on a Bruker D8 Advance diffractometer equipped with a Cu Kα radiation source at the X-ray Crystallographic Center at University of Maryland under ambient conditions.

Some of the data were collected from the Brookhaven National Laboratory National Synchrotron Light Source (NSLS) II, 28-ID-2 beamline using wavelength $\lambda = 0.1824$ Å.

Rietveld analyses were performed on each XRD data using GSAS-II ([59] and TOPAS [60] softwares.

5.3 Results and Discussion

5.3.1 *A*-site substitution

5.3.1.1 AMnFeO$_4$ (A = Y, Er, Yb, Lu) series

First, we start with *A*-site substitutions within the AMnFeO$_4$ (A = Y, Er, Yb, Lu) system. The structural and magnetic properties of Y-, Yb- and LuMnFeO$_4$ have been previously reported [50], however the oxygen storage property of ErMnFeO$_4$ remained unexplored. Here, we synthesized ErMnFeO$_4$ alongside the known compounds to provide a comprehensive comparison. All other compounds were resynthesized, and their structural and thermal behavior were verified via X-ray diffraction (XRD) and thermogravimetric analysis (TGA). The XRD patterns for the reduced and oxidized phases are presented in Figure 5.2. As expected, all reduced phases crystallized in the $R\bar{3}m$ space group, whereas the oxidized phases adopted the $P\bar{3}$ symmetry. The synthesized reduced phases appeared to be phase-pure, with

no detectable impurities. Upon oxidation, satellite peaks emerged in the diffraction patterns at positions consistent with previously reported structural modulations [50]. $ErMnFeO_4$ also showed satellite peaks at similar positions. Detailed lattice parameters obtained from Rietveld refinement are summarized in Table 5.2 for reduced phases and Table 5.3 for oxidized phases.

Using the refinement results, we investigated the lattice parameters for the reduced (Figure 5.3) and oxidized phases (Figure 5.4). In the reduced state, the substitution of larger *A*-site cations induces an expansion of the *a*-axis and a contraction of the *c*-axis. Despite the axial shortening, the total unit cell volume increases proportionally with the *A*-site ionic radius, confirming that the expansion in the basal plane outweighs the vertical contraction.

This structural behavior is driven by the steric effects of the *A*-site cation. As a larger *A*-site cation is introduced, its increased ionic volume exerts lateral pressure within the *A*-O framework, forcing the coordinated oxygen atoms to displace outward to accommodate the larger radius. This lateral expansion results in the observed expansion of the *ab*-plane. The contraction along the *c*-axis serves as a structural compensation mechanism to stabilize the lattice energy and maintain optimal bond lengths. By reducing the interlayer spacing, the system effectively "squeezes" the $Mn/Fe-O_5$ bipyramidal layers. This axial compression allows the transition metal centers to maintain a stable coordination environment while the lattice adjust to the steric bulk of the *A*-site cation.

In the oxidized state, the lattice parameter *a* and the unit cell volume continue to follow a clear positive correlation with the *A*-site ionic radius, similar to the trends observed in the reduced phases. However, the *c* parameter deviates from the linear decrease seen in the reduced phases. The values for the *c*-axis are remarkably similar across the series, which makes a definitive analysis of a size-dependent trend for this parameter difficult. Consequently, the overall increase in unit cell volume for larger *A*-site cations is primarily driven by the expansion of the *ab*-plane.

The relative changes in these parameters during the transition from the reduced to the oxidized state are illustrated in Figure 5.5. To facilitate a direct comparison, the *c*-axis values for the reduced phases were normalized by a factor of three. Upon oxidation, all compounds exhibit expansion in the *ab*-plane and a significant contraction along the *c*-axis, resulting in a net decrease in unit cell volume. We have previously reported that the contraction of the *c* parameter is attributed to the contraction of the Mn/FeO bipyramidal double layers as oxygen enters the layers [50]. The magnitude of these structural shifts is further quantified by the ratios of the oxidized-to-reduced parameters (a'/a, c'/c, V'/V) as a function of the *A*-site ionic radius (Figure 5.6). The data indicates that smaller *A*-site cations facilitate a more pronounced expansion in the *ab*-direction. However, this is outweighed by a much more severe contraction along the *c*-axis, leading to an overall reduction in unit cell volume for compounds with smaller *A*-site radii.

The oxidation behavior of the reduced phases was monitored under flowing air at a heating rate of 5 °C/min (Figures 5.7 and 5.9). The onset temperatures for bulk oxidation were determined to be around 266 °C, 267 °C, 321 °C, 312 °C for *A* = Y, Er, Yb, and Lu, respectively. Oxidation reached completion at 460 °C, 630 °C, 591 °C and 540 °C, respectively. Notably, $YMnFeO_4$ showed both the lowest onset and completion temperatures for oxygen uptake. $YbMnFeO_4$ starts oxidation at the highest temperature but finishes oxidation at similar temperature as $LuMnFeO_4$. All compounds formed stable oidized phases that did not undergo spontaneous reduction upon cooling to room temperature.

The total oxygen uptake, calculated from the TGA weight gain (Table 5.4), yielded values of 0.53(2), 0.63(3), 0.59(3), and 0.58(3) oxygen atoms per formula unit for *A* = Y, Er, Yb, and Lu, respectively. These values slightly exceed the theoretical stoichiometry of 0.5, suggesting the partial over-oxidation of Mn^{2+} to Mn^{4+}. Also it is notable that $ErMnFeO_4$ exhibited the highest degree of oxygen incorporation within the lattice.

To evaluate the reversibility of the oxygen storage process, the oxidized materials

were heated to 1000 °C under a reducing atmosphere 3% H_2/Ar (Figure 5.8. The onset temperatures for bulk reduction were 587 °C (Y), 706°C (Er), 650°C (Yb), and 591°C (Lu). A detailed view of these reduction profiles up to 750 °C is provided in Figure 5.9, allowing for a clearer observation of the initial weight loss transitions.

Based on the TGA profiles, all compounds appear to lose mass continuously following the bulk reduction rather than reaching a stable weight plateau. The calculated oxygen loss at 750 °C is summarized in Table 5.5 and indicates that the materials release more oxygen than was initially incorporated during the oxidation phase. This results in a slightly oxygen-deficient final stoichiometry, $A\mathrm{MnFeO}_{4-\delta}$ (See Table 5.5 for δ values). Among the series, $\mathrm{ErMnFeO_4}$ demonstrated the highest stability, with its final reduced state remaining closest to the original $A\mathrm{MnFeO_4}$ stoichiometry.

As the temperature increased further, a second major weight loss event occurred at onset temperatures of 731 °C, 792 °C, 723 °C, 741 °C for the Y, Er, Yb, and Lu compounds, respectively. While the Y, Yb, and Lu compounds reached a mass equilibrium between 950 °C and 980 °C, $\mathrm{ErMnFeO_4}$ continued to lose weight up to the instrumental limit of 1000 °C. Post-experimental XRD analysis was performed to investigate the state of the materials after heating to 1000 °C under a reducing atmosphere. The results confirmed that the compounds underwent decomposition into their starting reagents or other reduced phases. Specifically, $\mathrm{YMnFeO_4}$ and $\mathrm{LuMnFeO_4}$ decomposed into $\mathrm{Y_2O_3}$/$\mathrm{Lu_2O_3}$, MnO and Fe. For $\mathrm{YbMnFeO_4}$, the residue consisted of a mixture of $\mathrm{Yb_2O_3}$, $\mathrm{Mn_2O_7}$, MnO, and $\mathrm{YbGaMn_2O_5}$. These findings confirm that while the materials are capable of reversible oxygen exchange, they are susceptible to structural decomposition under a reducing atmosphere at high temperatures.

Generally, smaller *A*-site cations induced a more significant reduction in unit cell volume upon oxidation and a lower capacity for oxygen uptake (with the exception of $\mathrm{YMnFeO_4}$). Among the compounds investigated, $\mathrm{ErMnFeO_4}$ emerges as the most promising candidate for oxygen storage applications. It demonstrated the highest oxygen absorption capacity

while showing the best structural stability during the reduction process, recovering its original stoichiometry more effectively than the other variants.

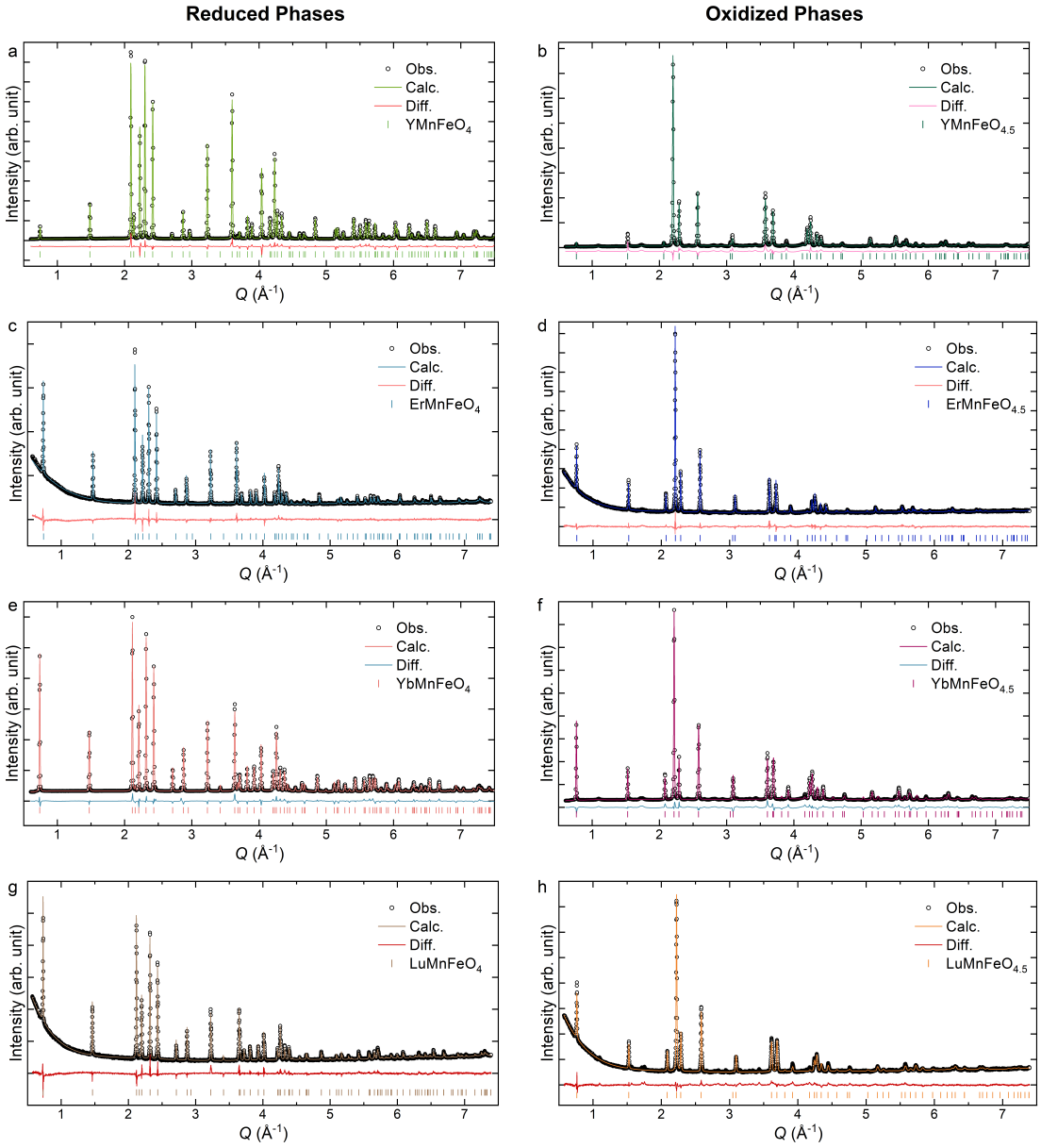


Figure 5.2: Rietveld refinement of powder X-ray diffraction patterns for reduced and oxidized $A\mathrm{MnFeO}_{4+\delta}$ phases. The left column (a, c, e, g) corresponds to the reduced $A\mathrm{MnFeO}_4$ phases, and the right column (b, d, f, h) corresponds to the oxidized $A\mathrm{MnFeO}_{4.5}$ phases for A = Y, Er, Yb, and Lu. Experimental data are shown as open circles (Obs.), with the calculated Rietveld profile (Calc.) and the difference curve (Diff.) indicated by solid lines. Vertical tick marks indicate the positions of allowed Bragg reflections. Data in (a, b) and (e, f) were collected at the Brookhaven National Laboratory synchrotron light source ($\lambda = 0.1824$ Å). Data in (c, d) and (g, h) were collected using a laboratory Cu K_α diffractometer.

Table 5.2: Refined structural parameters for reduced AMnFeO$_4$ (A = Y, Er, Yb, Lu) obtained from Rietveld refinement of powder X-ray diffraction data at 300 K.

YMnFeO$_4$	**Atom**	**Wyc. Pos.**	**x**	**y**	**z**	**Site Occ.**	**U_{iso}**
$R\bar{3}m$	Y	3a	0	0	0	1	0.0146(3)
$a = b$ = 3.49255(1) Å	Mn	6c	0	0	0.21507(4)	0.5	0.0079(4)
c = 25.4137(2) Å	Fe	6c	0	0	0.21507(4)	0.5	0.0079(4)
α = β = 90° γ = 120°	O1	6c	0	0	0.2924(2)	1	0.0098(1)
vol = 268.463(3) Å^3	O2	6c	0	0	0.1277(2)	1	0.0224(1)
R_{wp} = 8.34 %							
ErMnFeO$_4$	**Atom**	**Wyc. Pos.**	**x**	**y**	**z**	**Site Occ.**	**U_{iso}**
$R\bar{3}m$	Er	3a	0	0	0	1	0.0093(5)
$a = b$ = 3.47986(7) Å	Mn	6c	0	0	0.21452(7)	0.5	0.021(8)
c = 25.5559(3) Å	Fe	6c	0	0	0.21452(7)	0.5	0.021(8)
α = β = 90° γ = 120°	O1	6c	0	0	0.2903(2)	1	0.022(2)
vol = 268.007(8) Å^3	O2	6c	0	0	0.1267(2)	1	0.022(2)
R_{wp} = 3.381 %							
YbMnFeO$_4$	**Atom**	**Wyc. Pos.**	**x**	**y**	**z**	**Site Occ.**	**U_{iso}**
$R\bar{3}m$	Yb	3a	0	0	0	1	0.0134(3)
$a = b$ = 3.45433(2) Å	Mn	6c	0	0	0.21569(6)	0.5	0.01330
c = 25.5821(3) Å	Fe	6c	0	0	0.21569(6)	0.5	0.01330
α = β = 90° γ = 120°	O1	6c	0	0	0.2924(2)	1	0.016(2)
vol = 264.360(4) Å^3	O2	6c	0	0	0.1270(2)	1	0.0303(2)
R_{wp} = 3.60 %							
LuMnFeO$_4$	**Atom**	**Wyc. Pos.**	**x**	**y**	**z**	**Site Occ.**	**U_{iso}**
$R\bar{3}m$	Lu	3a	0	0	0	1	0.0017(4)
$a = b$ = 3.44437(5) Å	Mn	6c	0	0	0.2150(1)	0.5	0.0210
c = 25.7340(3) Å	Fe	6c	0	0	0.2150(1)	0.5	0.0210
α = β = 90° γ = 120°	O1	6c	0	0	0.2892(3)	1	0.042(3)
vol = 264.398(4) Å^3	O2	6c	0	0	0.1274(3)	1	0.042(3)
R_{wp} = 4.384 %							

Table 5.3: Refined structural parameters for oxidized AMnFeO$_{4.5}$ (A = Y, Er, Yb, Lu) obtained from Rietveld refinement of powder X-ray diffraction data at 300 K.

YMnFeO$_{4.5}$	**Atom**	**Wyc. Pos.**	**x**	**y**	**z**	**Site Occ.**	**U$_{iso}$**
$P\bar{3}$	Y	1a	0	0	0	1	0.0483(2)
$a = b$ = 3.51614(6) Å	Mn	2d	0.66667	0.33333	0.3538(3)	0.5	0.00887(8)
c = 8.2282(3) Å	Fe	2d	0.66667	0.33333	0.3538(3)	0.5	0.00887(8)
α = β = 90° γ = 120°	O1	2d	0.66667	0.33333	0.122(1)	1	0.0329(4)
vol = 88.098(4) Å^3	O2	2d	0.33333	0.66667	0.415(2)	0.71(2)	0.0456(5)
R_{wp} = 13.47 %	O3	2c	0	0	0.324(2)	0.54(2)	0.0456(5)
ErMnFeO$_{4.5}$	**Atom**	**Wyc. Pos.**	**x**	**y**	**z**	**Site Occ.**	**U$_{iso}$**
$P\bar{3}$	Er	1a	0	0	0	1	0.0210(8)
$a = b$ = 3.50546(9) Å	Mn	2d	0.66667	0.33333	0.3561(5)	0.5	0.010(1)
c = 8.2526(2) Å	Fe	2d	0.66667	0.33333	0.3561(5)	0.5	0.010(1)
α = β = 90° γ = 120°	O1	2d	0.66667	0.33333	0.1528(9)	1	0.064(3)
vol = 87.823(4) Å^3	O2	2d	0.33333	0.66667	0.418(2)	0.79(1)	0.064(3)
R_{wp} = 3.09 %	O3	2c	0	0	0.312(2)	0.46(1)	0.064(3)
YbMnFeO$_{4.5}$	**Atom**	**Wyc. Pos.**	**x**	**y**	**z**	**Site Occ.**	**U$_{iso}$**
$P\bar{3}$	Yb	1a	0	0	0	1	0.02850(9)
$a = b$ = 3.485465(9) Å	Mn	2d	0.66667	0.33333	0.3523(7)	0.5	0.0141(2)
c = 8.2295(3) Å	Fe	2d	0.66667	0.33333	0.3523(7)	0.5	0.0141(2)
α = β = 90° γ = 120°	O1	2d	0.66667	0.33333	0.133(2)	1	0.0545(5)
vol = 86.582(4) Å^3	O2	2d	0.33333	0.66667	0.414(3)	0.77(2)	0.0545(5)
R_{wp} = 6.07 %	O3	2c	0	0	0.292(4)	0.48(2)	0.0545(5)
LuMnFeO$_{4.5}$	**Atom**	**Wyc. Pos.**	**x**	**y**	**z**	**Site Occ.**	**U$_{iso}$**
$P\bar{3}$	Lu	1a	0	0	0	1	0.0102(4)
$a = b$ = 3.4773(2) Å	Mn	2d	0.66667	0.33333	0.3528(6)	0.5	0.0102(4)
c = 8.2492(3) Å	Fe	2d	0.66667	0.33333	0.3528(6)	0.5	0.0102(4)
α = β = 90° γ = 120°	O1	2d	0.66667	0.33333	0.160(1)	1	0.023(3)
vol = 86.382(8) Å^3	O2	2d	0.33333	0.66667	0.407(2)	0.89(1)	0.023(3)
R_{wp} = 4.05 %	O3	2c	0	0	0.297(3)	0.36(1)	0.023(3)

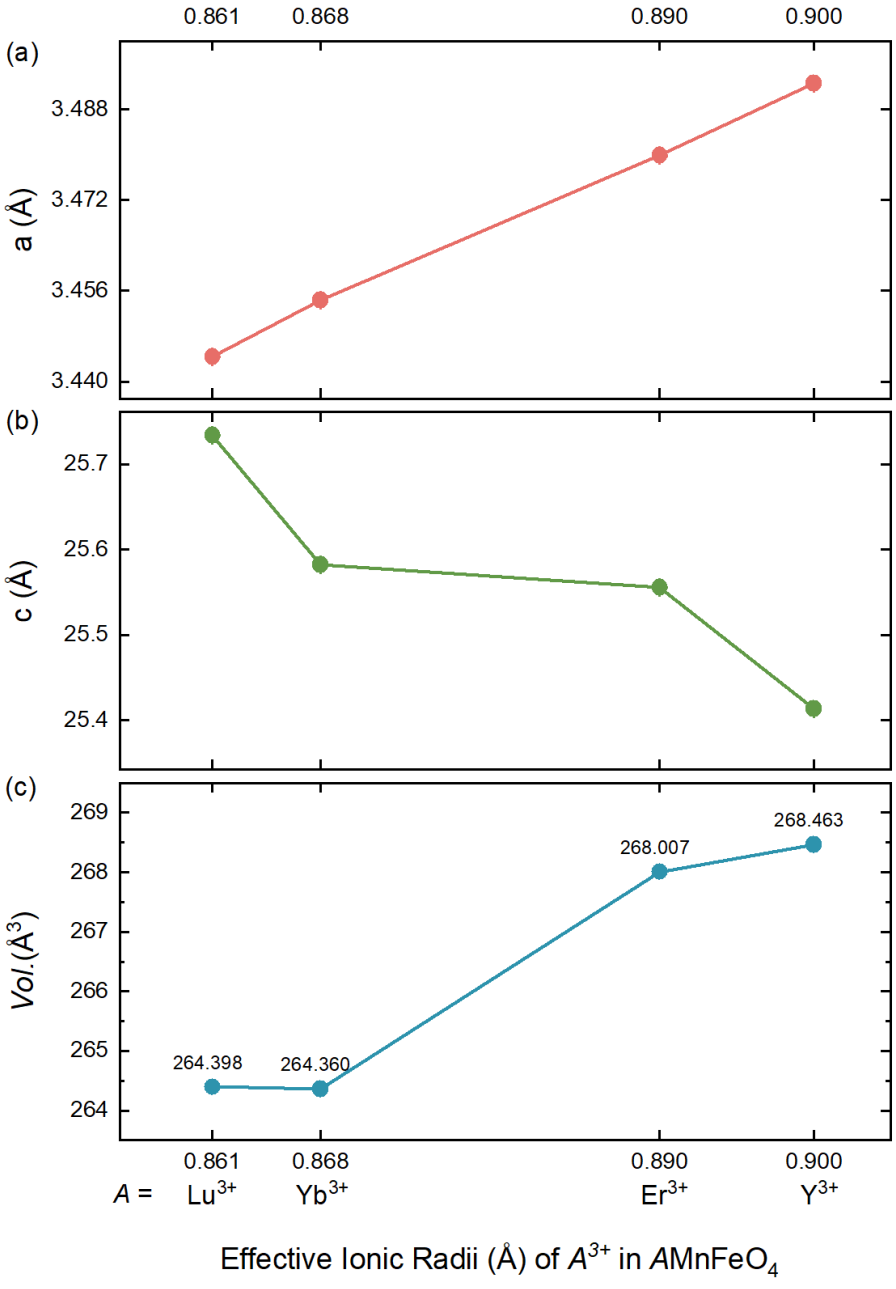


Figure 5.3: Comparison of lattice parameters and unit cell volume as a function of A-site ionic radius for AMnFeO$_4$ (A = Lu, Yb, Er, Y). (a) lattice parameter a, (b) lattice parameter c, and (c) unit cell volume ($Vol.$) are plotted against the effective ionic radii of the A^{3+} cations in VI-fold octahedral coordination [113]. Error bars are smaller than the symbol size and are therefore not visible.

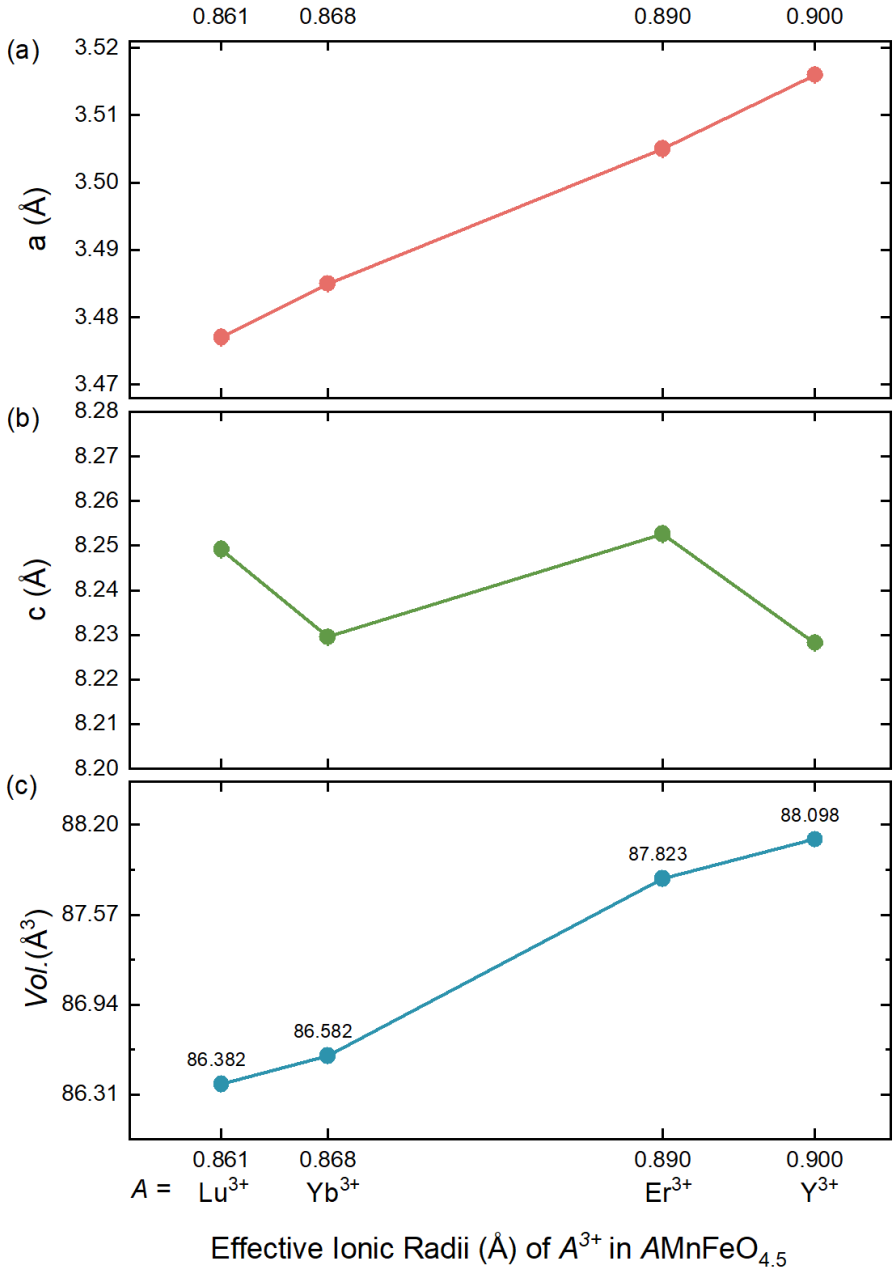


Figure 5.4: Comparison of lattice parameters and unit cell volume for oxidized AMnFeO$_{4.5}$ (A = Lu, Yb, Er, Y) as a function of A-site ionic radius. (a) lattice parameter a, (b) lattice parameter c, and (c) unit cell volume (*Vol.*) are plotted against the effective ionic radii of the A^{3+} cations in VI-fold octahedral coordination [113]. Error bars are smaller than the symbol size and are therefore not visible.

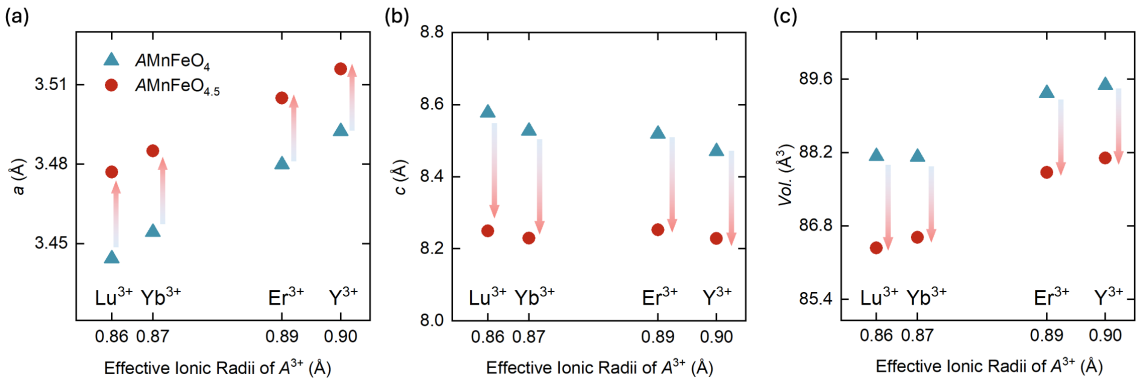


Figure 5.5: Evolution of lattice parameters and unit cell volume upon oxidation of AMnFeO$_4$. Comparison of (a) lattice parameter a, (b) lattice parameter c, and (c) unit cell volume for AMnFeO$_{4+\delta}$ (A = Lu, Yb, Er, Y). Blue triangles represent the reduced phases (O$_4$) and red circles represent the oxidized phases (O$_{4.5}$). Arrows indicate the oxygen uptake direction. c lattice parameters are normalized for the reduced phases and are divided by 3 for direct comparison. Error bars are smaller than the symbol size and are therefore not visible.

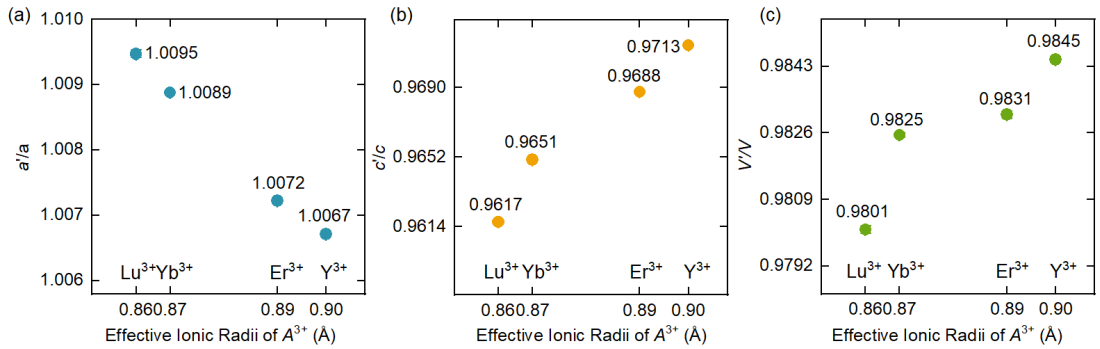


Figure 5.6: Relative structural changes in AMnFeO$_{4+\delta}$ upon oxidation. The panels show the ratio of the oxidized ($'$) to reduced parameters for (a) lattice parameter a'/a, (b) lattice parameter c'/c, and (c) unit cell volume V'/V as a function of A^{3+} effective ionic radii[113]. Ratios > 1 indicate an expansion, while ratio < 1 indicate a contraction upon oxygen uptake.

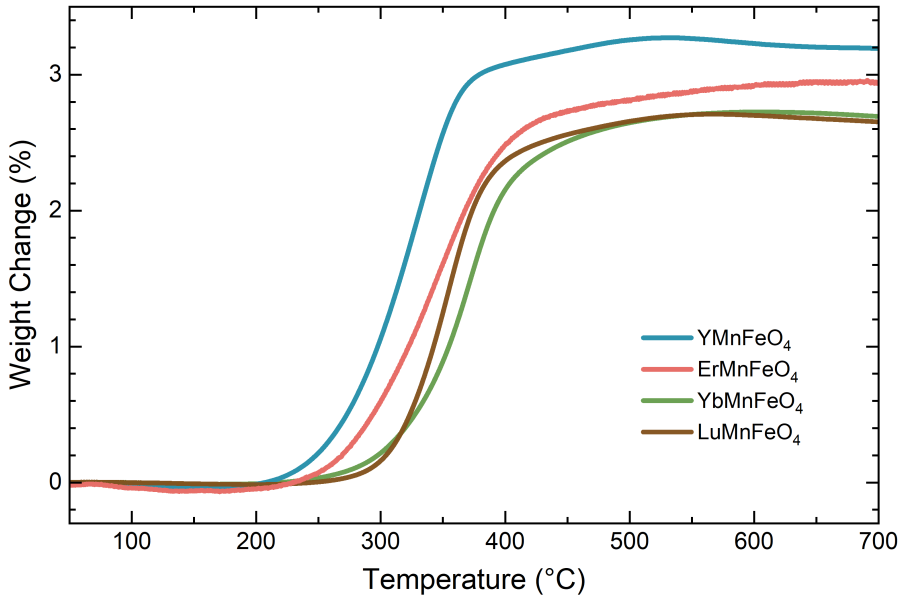


Figure 5.7: Thermogravimetric analysis (TGA) of AMnFeO$_4$ (A = Y, Er, Yb, Lu) in flowing air. The weight change (%) is plotted as a function of temperature from 50–700 °C. All samples were measured with a heating rate of 5 °C/min.

Table 5.4: Experimental weight gain and calculated oxygen stoichiometry for AMnFeO$_4$ (A = Y, Er, Yb, Lu) following oxidation in air up to 700 °C.

Compound	ΔW (%)	Oxygen Atoms Added	Final Stoichiometry
YMnFeO$_4$	3.2(1)	0.53(2)	YMnFeO$_{4.53}$
ErMnFeO$_4$	2.9(1)	0.63(3)	ErMnFeO$_{4.63}$
YbMnFeO$_4$	2.7(1)	0.59(3)	YbMnFeO$_{4.59}$
LuMnFeO$_4$	2.7(1)	0.58(3)	LuMnFeO$_{4.58}$

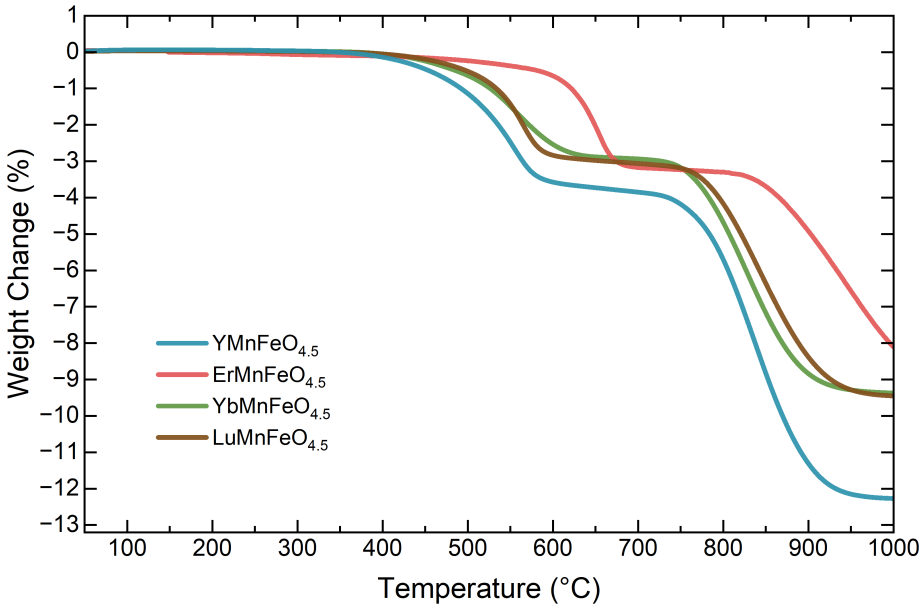


Figure 5.8: Thermogravimetric analysis (TGA) of the reduction of oxidized AMnFeO$_{4.5}$ (A = Y, Er, Yb, Lu) in a 3% H$_2$/Ar atmosphere. The weight change (%) is recorded from 50–1000 °C at a constant heating rate of 5 °C/min.

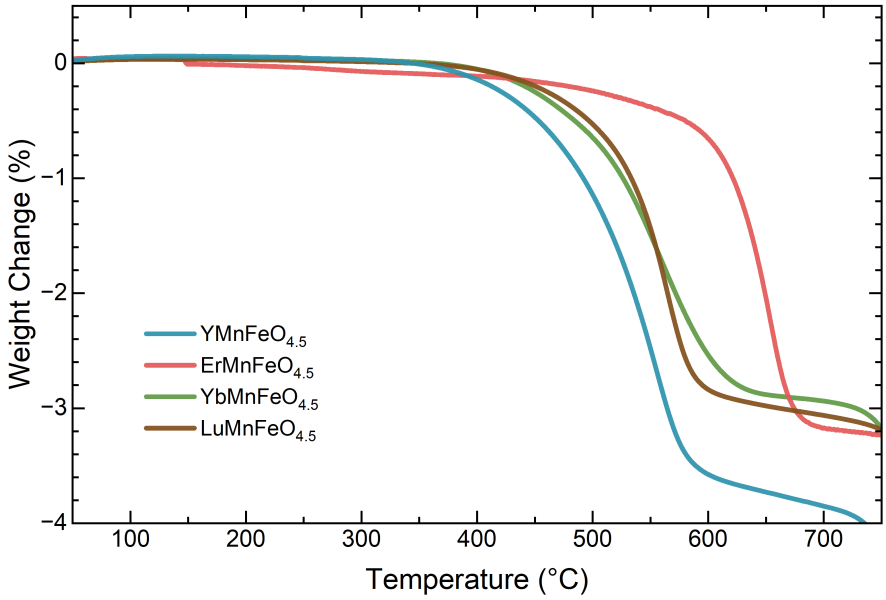


Figure 5.9: Thermogravimetric analysis (TGA) of the reduction of oxidized AMnFeO$_{4.5}$ (A = Y, Er, Yb, Lu) in a 3% H$_2$/Ar atmosphere. The weight change (%) is recorded from 50–750 °C at a constant heating rate of 5 °C/min.

Table 5.5: Experimental weight loss and calculated oxygen stoichiometry for oxidized AMnFeO$_{4+\delta}$ (A = Y, Er, Yb, Lu) following reduction in 3% H_2/Ar up to 750 °C.

Compound	**ΔW (%)**	**Oxygen Atoms Released**	**Final Stoichiometry**
YMnFeO$_{4.53}$	−3.8(1)	0.65(2)	YMnFeO$_{3.88}$
ErMnFeO$_{4.63}$	−3.2(1)	0.69(3)	ErMnFeO$_{3.94}$
YbMnFeO$_{4.59}$	−2.9(1)	0.66(3)	YbMnFeO$_{3.93}$
LuMnFeO$_{4.58}$	−3.06(1)	0.69(3)	LuMnFeO$_{3.89}$

5.3.1.2 AFe$_2$O$_4$ (A = Er, Yb, Lu) series

Similar analyses were performed for the A-site substituted compounds in the AFe$_2$O$_4$ system. The XRD patterns of synthesized materials, obtained via both laboratory and synchrotron sources, are presented in Figure 5.10. Consistent with previous reports, the reduced phases crystallized in the $R\bar{3}m$ space group, while the oxidized phases transitioned to the $P\bar{3}$ symmetry. Rietveld analysis of the synthesized ErFe$_2$O$_4$ revealed a minor ErFeO$_3$ (*Pbnm* space group) impurity with a 7.7 % phase fraction. Upon oxidation, this impurity fraction decreased to 2.5 %; however, this discrepancy is likely attibutable to batch variations. Similarly, the oxidized LuFe$_2$O$_4$ sample exhibited a Lu$_2$Fe$_3$O$_{7.5}$ impurity, which was also identified as a result of utilizing a different synthesis batch. The refined structural parameters are summarized in Tables 5.6 and 5.7. For a comprehensive comparison, literature values for YFe$_2$O$_4$ and InFe$_2$O$_4$ [48] are included in Table 5.6. However, as the oxidizized crystal structures for these compounds have not been previously reported, they were excluded from the oxidized phase comparison.

The structural evolution of the AFe$_2$O$_4$ series exhibits an analogous trend to the AMnFeO$_4$ system. As illustrated in Figure 5.11, an increase in the A-site ionic radius correlates with an expansion of the a parameter and a concomitant contraction of the c parameter, resulting in an overall trend in unit cell volume. The influence of the A-site cation is particularly evident when comparing InFe$_2$O$_4$ to the rare-earth and Y^{3+} analogues. Because In^{3+} is significantly smaller than the other cations in this series, its unit cell volume (263 Å^3) is predictably lower. A direct correlation exists between the ionic radius and the unit cell volume across the series: the smaller Lu^{3+} and Yb^{3+} cations yield comparable volumes ($\sim$263 Å^3), while the larger Er^{3+} and Y^{3+} cations result in expanded volumes ($\sim$ 265 Å^3).

In the oxidized phases, the comparison was limited to A = Lu, Yb, Er. These compounds exhibit the same trend: expansion in the *ab*-plane and contraction along the c-axis, leading to

a net increase in volume. While $YbFe_2O_{4.5}$ shows a slightly smaller volume than $LuFe_2O_{4.5}$, the values are too close to allow for a meaningful distinction.

The interesting observation was when we were comparing the lattice parameter change as the materials oxidized. Unlike the AMnFeO$_4$ series where as oxidation the lattice expanded in the *ab* plane and reduced in the *c* direction, here all the AFe_2O_4 materials expand in both *ab* and *c* direction (Figures 5.13 and 5.14. This opposite trend seemed to be a relation of the *B* site cation, which we will discuss in the following section.

The thermogravimetric profiles for the oxidized $AFe_2O_{4+\delta}$ ($A =$ Er, Yb, Lu) series are presented in Figures 5.15 and 5.17. In contrast to the AMnFeO$_4$ series, these compounds exhibit lower oxygen stoichiometry, with δ values falling below the target 0.5. The *A*-site cation size trend remains consistent: larger *A*-site cations facilitate greater oxygen intercalation into the lattice.

During the reduction experiments, bulk oxygen loss occurs approximately at 500 - 510 °C for $ErFe_2O_{4.5}$ and $LuFe_2O_{4.5}$, and 570 °C for $YbFe_2O_{4.5}$. Notably, none of the $AFe_2O_{4+\delta}$ compounds exhibit a stable plateau corresponding to the stoichiometric AFe_2O_4 phase. Instead, the continuous weight loss suggests that the reduced phase is highly metastable and begins to decompose soon after the initial reduction step. Among the series, $YbFe_2O_{4.5}$ demonstrates the lowest structural stability at elevated temperatures. Quantitative analysis of the TGA curves indicates that the total oxygen loss exceeds the amount initially intercalated (Figure 5.17).

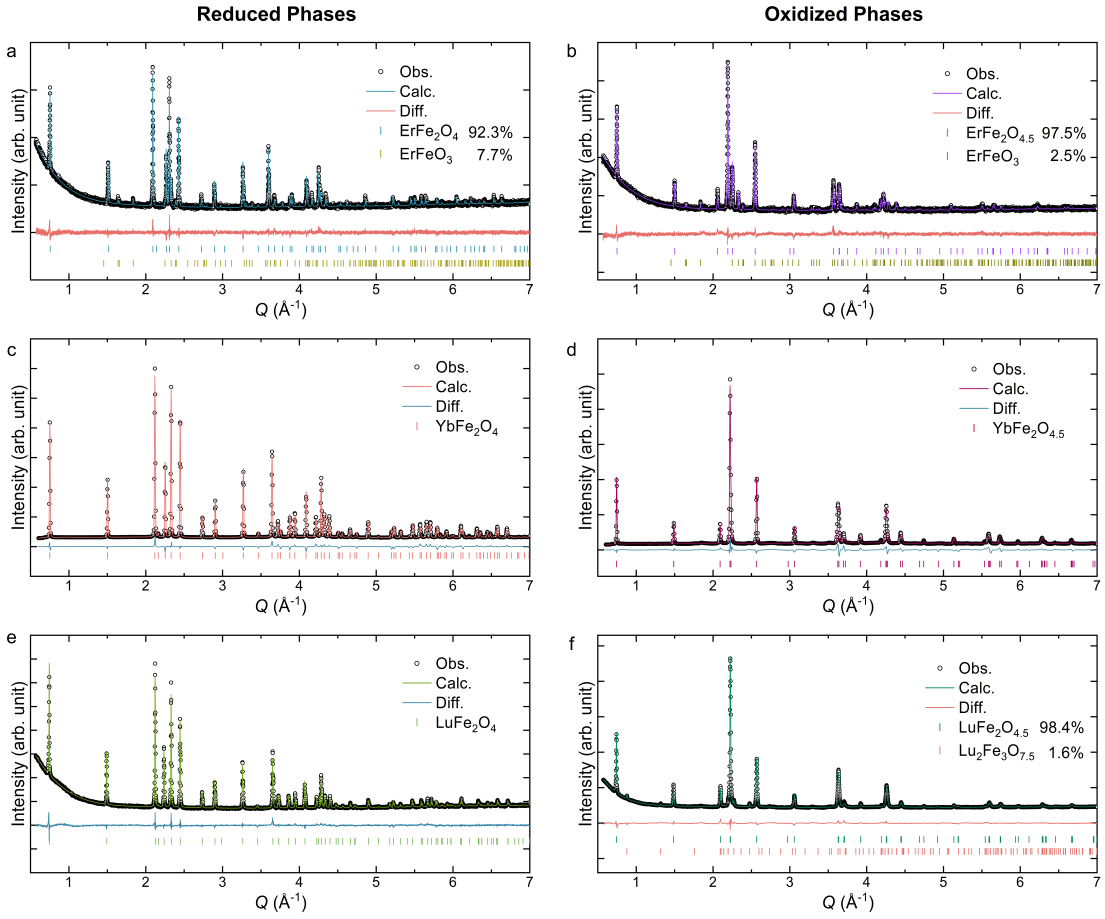


Figure 5.10: Rietveld refinement of powder X-ray diffraction patterns for reduced and oxidized $A\mathrm{Fe_2O_{4+\delta}}$ phases. The left column (a, c, e) corresponds to the reduced $A\mathrm{Fe_2O_4}$ phases, and the right column (b, d, f) corresponds to the oxidized $A\mathrm{Fe_2O_{4.5}}$ phases for $A =$ Er, Yb, and Lu. Experimental data are shown as open circles (Obs.), with the calculated Rietveld profile (Calc.) and the difference curve (Diff.) indicated by solid lines. Vertical tick marks indicate the positions of allowed Bragg reflections. Data in (c and b) were collected at the Brookhaven National Laboratory synchrotron light source ($\lambda = 0.1824$ Å). Data in (a, b, e, f) were collected using a laboratory Cu K_α diffractometer.

Table 5.6: Refined structural parameters for reduced AFe_2O_4 (A = Er, Yb, Lu, Y, In) obtained from Rietveld refinement of powder X-ray diffraction data at 300 K. *Data for YFe_2O_4 and $InFe_2O_4$ were taken from a previously reported study [48].

$ErFe_2O_4$	**Atom**	**Wyc. Pos.**	**x**	**y**	**z**	**Site Occ.**	**U_{iso}**
$R\bar{3}m$ $a = b$ = 3.49169(4) Å c = 24.9288(2) Å α = β = 90° γ = 120° vol = 263.210(3) Å^3 R_{wp} = 3.26 %	Er	3a	0	0	0	1	0.0089(6)
	Fe	6c	0	0	0.21512(8)	1	0.0021(9)
	O1	6c	0	0	0.2878(2)	1	0.017(3)
	O2	6c	0	0	0.1286(3)	1	0.050(3)
$YbFe_2O_4$	**Atom**	**Wyc. Pos.**	**x**	**y**	**z**	**Site Occ.**	**U_{iso}**
$R\bar{3}m$ $a = b$ = 3.44893(1) Å c = 25.1003(1) Å α = β = 90° γ = 120° vol = 258.571(2) Å^3 R_{wp} = 3.72 %	Y	3a	0	0	0	1	0.01684(3)
	Fe	6c	0	0	0.21511(6)	1	0.00912(5)
	O1	6c	0	0	0.2925(2)	1	0.0236(2)
	O2	6c	0	0	0.1278(2)	1	0.0103(2)
$LuFe_2O_4$	**Atom**	**Wyc. Pos.**	**x**	**y**	**z**	**Site Occ.**	**U_{iso}**
$R\bar{3}m$ $a = b$ = 3.43846(6) Å c = 25.2532(3) Å α = β = 90° γ = 120° vol = 258.568(7) Å^3 R_{wp} = 2.664 %	Lu	3a	0	0	0	1	0.0060(2)
	Fe	6c	0	0	0.21460(7)	1	0.0060(2)
	O1	6c	0	0	0.2887(2)	1	0.024(2)
	O2	6c	0	0	0.1279(2)	1	0.025(2)
YFe_2O_4*	**Atom**	**Wyc. Pos.**	**x**	**y**	**z**	**Site Occ.**	**U_{iso}**
$R\bar{3}m$ $a = b$ = 3.51188(1) Å c = 24.84257(7) Å α = β = 90° γ = 120° vol = 265.342(2) Å^3 R_{wp} = 12.03 %	Y	3a	0	0	0	1	$U_{11} = U_{22}$ = 0.00230(8) U_{33} = 0.0629(3) U_{12} = 0.00115(8)
	Fe	6c	0	0	0.21454(1)	1	0.01341(9)
	O1	6c	0	0	0.29193(6)	1	0.0197(3)
	O2	6c	0	0	0.12828(5)	1	0.0197(3)
$InFe_2O_4$*	**Atom**	**Wyc. Pos.**	**x**	**y**	**z**	**Site Occ.**	**U_{iso}**
$R\bar{3}m$ $a = b$ = 3.51188(1) Å c = 24.84257(7) Å α = β = 90° γ = 120° vol = 265.342(2) Å^3 R_{wp} = 12.03 %	In	3a	0	0	0	1	$U_{11} = U_{22}$ = 0.00350(8) U_{33} = 0.072(1) U_{12} = 0.00175(8)
	Fe	6c	0	0	0.21653(1)	1	0.0065(1)
	O1	6c	0	0	0.12861(6)	1	0.0096(3)
	O2	6c	0	0	0.29290(6)	1	0.0096(3)

Table 5.7: Refined structural parameters for oxidized $A\mathrm{Fe_2O_{4.5}}$ (A = Er, Yb, Lu) obtained from Rietveld refinement of powder X-ray diffraction data at 300 K.

$\mathrm{ErFe_2O_{4.5}}$	**Atom**	**Wyc. Pos.**	**x**	**y**	**z**	**Site Occ.**	**U_{iso}**
$P\bar{3}$ $a = b = 3.52183(6)$ Å $c = 8.3731(1)$ Å α = β = 90° γ = 120° vol = 89.940(2) Å^3 $R_{wp} = 3.400$ %	Er	1a	0	0	0	1	0.0205(8)
	Fe	2d	0.66667	0.33333	0.3474(7)	1	0.016(2)
	O1	2d	0.66667	0.33333	0.129(1)	1	0.090(5)
	O2	2d	0.33333	0.66667	0.419(3)	0.56(2)	0.090(5)
	O3	2c	0	0	0.329(2)	0.70(2)	0.090(5)
$\mathrm{YbFe_2O_{4.5}}$	**Atom**	**Wyc. Pos.**	**x**	**y**	**z**	**Site Occ.**	**U_{iso}**
$P\bar{3}$ $a = b = 3.46778(1)$ Å $c = 8.4397(2)$ Å α = β = 90° γ = 120° vol = 87.894(3) Å^3 $R_{wp} = 2.665$ %	Yb	1a	0	0	0	1	0.03154(8)
	Fe	2d	0.66667	0.33333	0.3466(8)	1	0.0222(2)
	O1	2d	0.66667	0.33333	0.140(2)	1	0.1494(1)
	O2	2d	0.33333	0.66667	0.411(5)	0.82(3)	0.0253(1)
	O3	2c	0	0	0.279(4)	0.43(3)	0.0253(1)
$\mathrm{LuFe_2O_{4.5}}$	**Atom**	**Wyc. Pos.**	**x**	**y**	**z**	**Site Occ.**	**U_{iso}**
$R\bar{3}m$ $a = b = 3.46284(7)$ Å $c = 8.4662(2)$ Å α = β = 90° γ = 120° vol = 87.919(2) Å^3 $R_{wp} = 2.076$ %	Yb	1a	0	0	0	1	0.0293(8)
	Fe	2d	0.66667	0.33333	0.3528(8)	1	0.009(1)
	O1	2d	0.66667	0.33333	0.1410(8)	1	0.062(4)
	O2	2d	0.33333	0.66667	0.404(4)	0.67(1)	0.062(4)
	O3	2c	0	0	0.323(2)	0.58(1)	0.062(4)

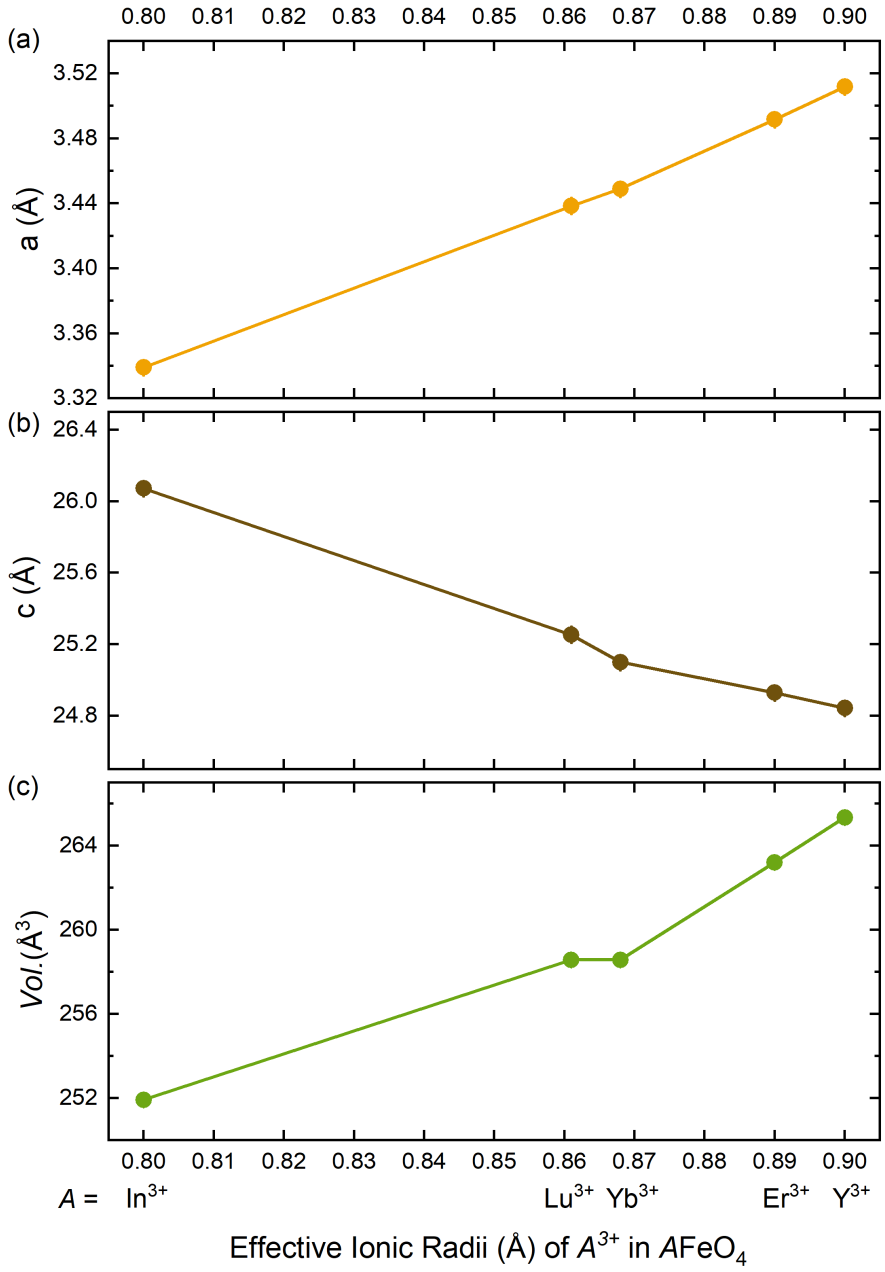


Figure 5.11: Comparison of lattice parameters and unit cell volume as a function of *A*-site ionic radius for AFe_2O_4 (*A* = In, Lu, Yb, Er, Y). (a) lattice parameter *a*, (b) lattice parameter *c*, and (c) unit cell volume (*Vol.*) are plotted against the effective ionic radii of the A^{3+} cations in VI-fold octahedral coordination [113]. Error bars are smaller than the symbol size and are therefore not visible.

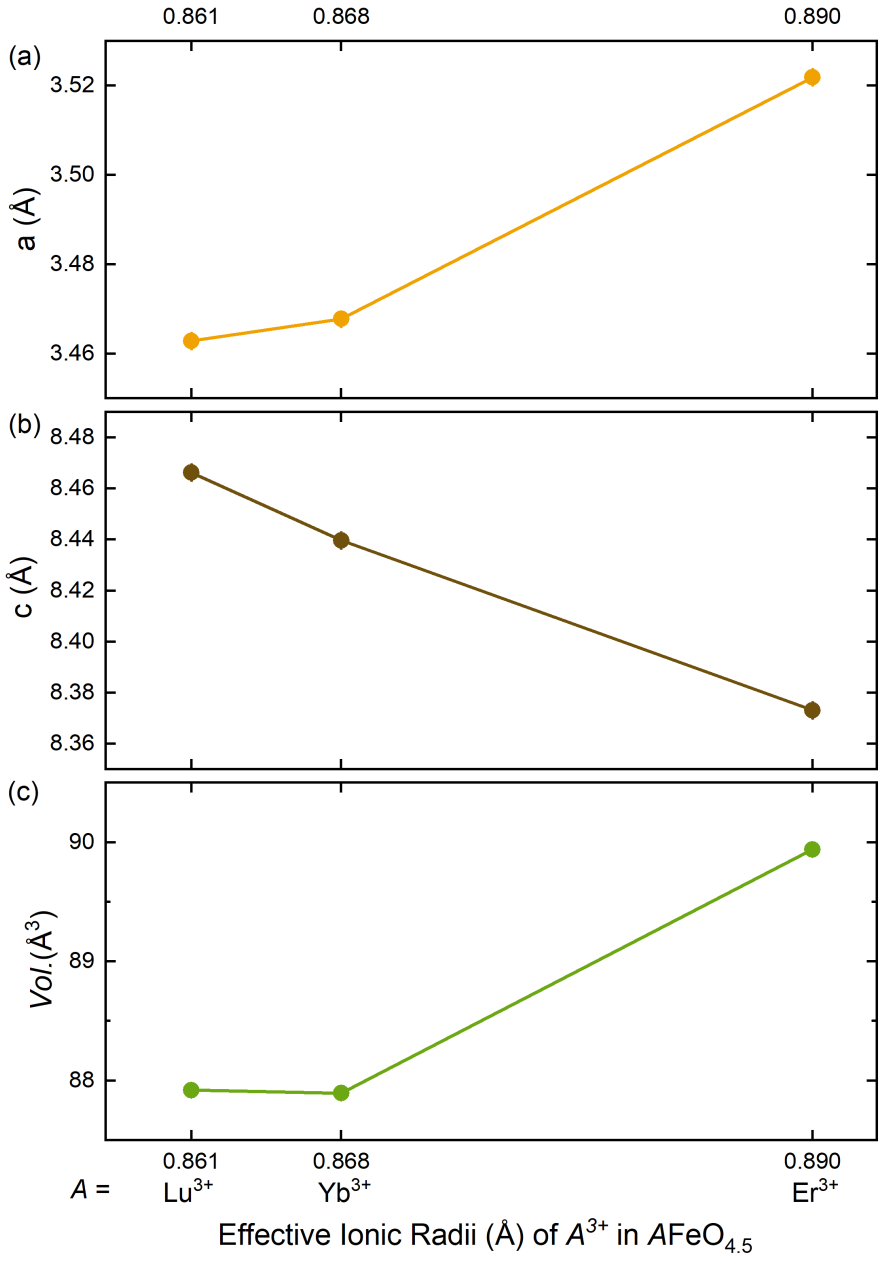


Figure 5.12: Comparison of lattice parameters and unit cell volume for oxidized $A\mathrm{Fe_2O_{4.5}}$ (A = Lu, Yb, Er) as a function of A-site ionic radius. (a) lattice parameter a, (b) lattice parameter c, and (c) unit cell volume (*Vol.*) are plotted against the effective ionic radii of the A^{3+} cations in VI-fold octahedral coordination [113]. Error bars are smaller than the symbol size and are therefore not visible.

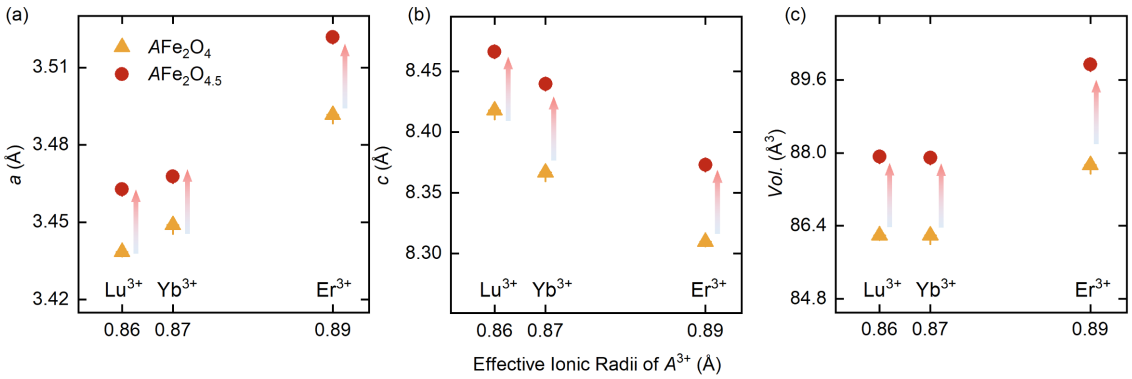


Figure 5.13: Evolution of lattice parameters and unit cell volume upon oxidation of AFe_2O_4. Comparison of (a) lattice parameter a, (b) lattice parameter c, and (c) unit cell volume for $AFe_2O_{4+\delta}$ (A = Lu, Yb, Er). Yello triangles represent the reduced phases (O_4) and red circles represent the oxidized phases ($O_{4.5}$). Arrows indicate the oxygen uptake direction. c lattice parameters are normalized for the reduced phases and are divided by 3 for direct comparison. Error bars are smaller than the symbol size and are therefore not visible.

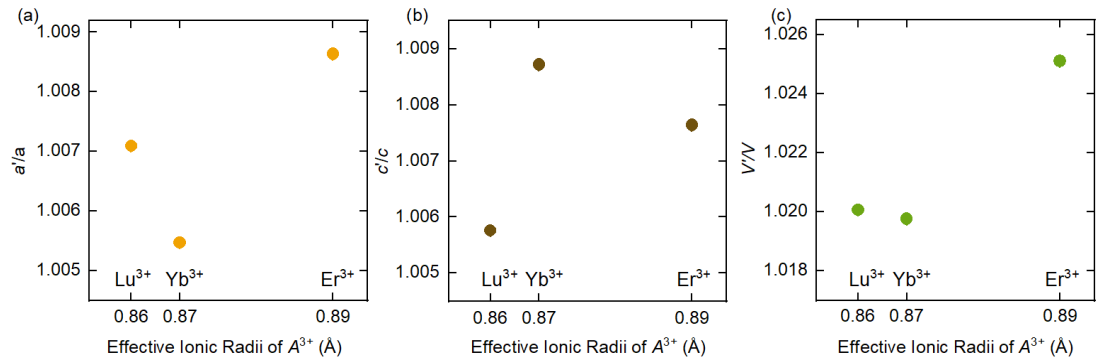


Figure 5.14: Relative structural changes in $AFe_2O_{4+\delta}$ upon oxidation. The panels show the ratio of the oxidized ($'$) to reduced parameters for (a) lattice parameter a'/a, (b) lattice parameter c'/c, and (c) unit cell volume V'/V as a function of A^{3+} effective ionic radii[113]. Ratios > 1 indicate an expansion.

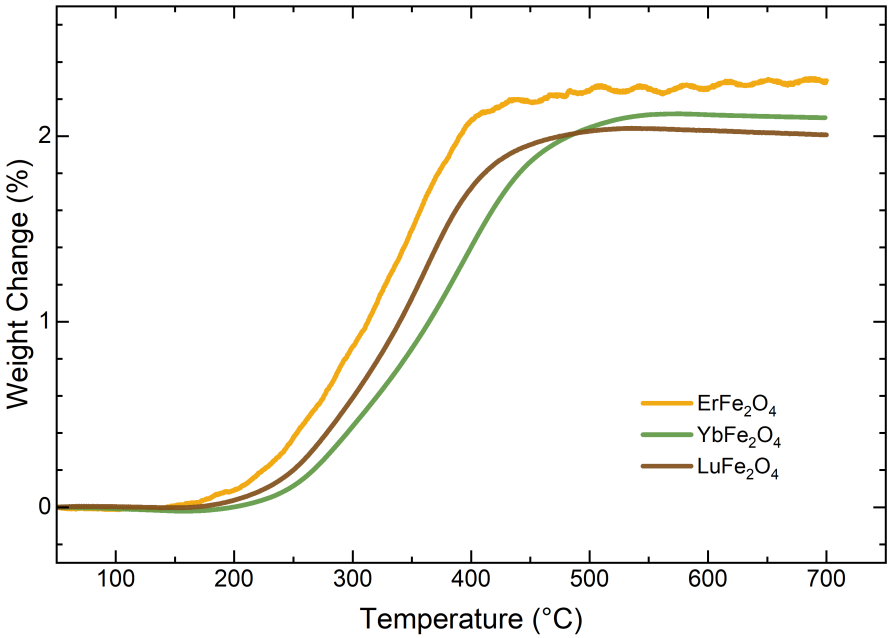


Figure 5.15: Thermogravimetric analysis (TGA) of $A\mathrm{Fe_2O_4}$ (A = Er, Yb, Lu) in flowing air. The weight change (%) is plotted as a function of temperature from 50–700 °C. All samples were measured with a heating rate of 5 °C/min.

Table 5.8: Experimental weight gain and calculated oxygen stoichiometry for $A\mathrm{Fe_2O_4}$ (A = Er, Yb, Lu) following oxidation in air up to 700 °C.

Compound	ΔW (%)	Oxygen Atoms Added	Final Stoichiometry
$\mathrm{ErFe_2O_4}$	2.3(1)	0.49(3)	$\mathrm{ErFe_2O_{4.49}}$
$\mathrm{YbFe_2O_4}$	2.1(1)	0.46(3)	$\mathrm{YbFe_2O_{4.46}}$
$\mathrm{LuFe_2O_4}$	2.0(1)	0.44(3)	$\mathrm{LuFe_2O_{4.44}}$

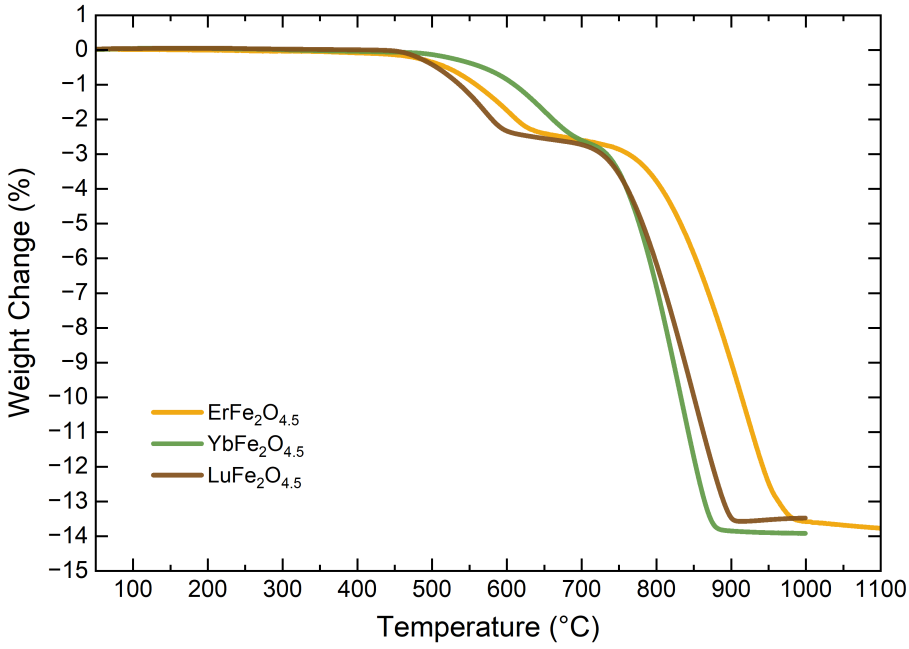


Figure 5.16: Thermogravimetric analysis (TGA) of the reduction of oxidized AMnFeO$_{4.5}$ (A = Y, Er, Yb, Lu) in a 3% H_2/Ar atmosphere. The weight change (%) is recorded from 50–1000 °C (1100 °C for $ErFe_2O_4$) at a constant heating rate of 5 °C/min.

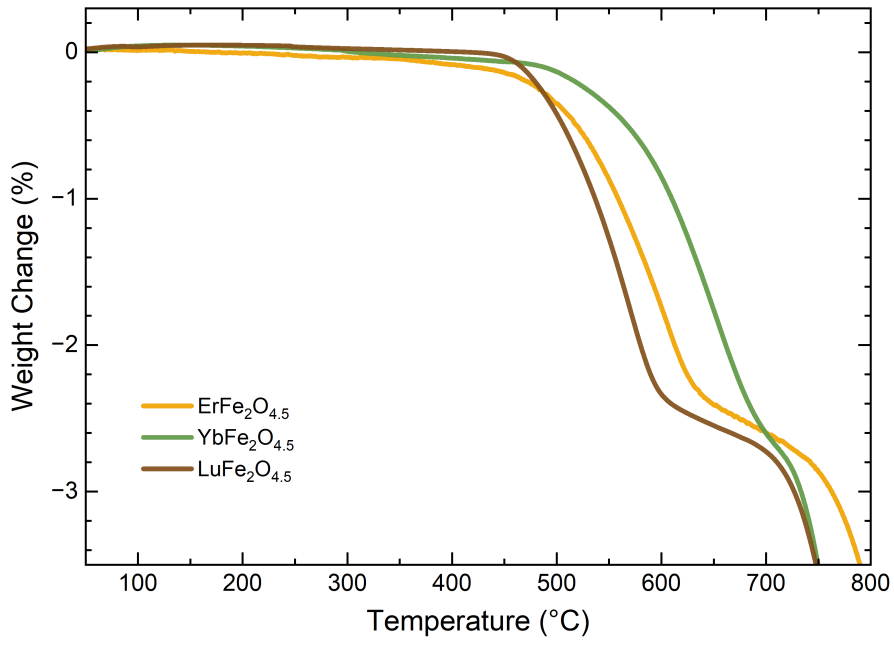


Figure 5.17: Thermogravimetric analysis (TGA) of the reduction of oxidized AFe$_2$O$_{4.5}$ (A = Er, Yb, Lu) in a 3% H_2/Ar atmosphere. The weight change (%) is recorded from 50–750 °C at a constant heating rate of 5 °C/min.

Table 5.9: Experimental weight loss and calculated oxygen stoichiometry for oxidized $A\mathrm{Fe_2O_{4+\delta}}$ (A = Er, Yb, Lu) following reduction in 3% $\mathrm{H_2}$/Ar at 700 °C (Er), 715 °C (Yb), 650 °C (Lu).

Compound	ΔW (%)	Oxygen Atoms Released	Final Stoichiometry
$\mathbf{ErFe_2O_{4.49}}$	−2.6(1)	0.57(3)	$\mathrm{ErFe_2O_{3.92}}$
$\mathbf{YbFe_2O_{4.46}}$	−2.7(1)	0.61(3)	$\mathrm{YbFe_2O_{3.83}}$
$\mathbf{LuFe_2O_{4.44}}$	−2.5(1)	0.60(3)	$\mathrm{LuFe_2O_{3.87}}$

5.3.2 *B*-site substitution

To investigate the influence of *B*-site cation substitution, a comparative analysis was performed on $LuFe_2O_4$, $LuMnFeO_4$, and $LuMnGaO_4$. The refined structural parameters, unit cell volumes, and oxygen over-stoichiometry (δ) after oxidation are summarized in Table 5.10, with corresponding TGA profiles provided in Figure 5.18.

Table 5.10: Refined lattice parameters (a, c), unit cell volume (V) for reduced (R) and oxidized (O) phases of $LuFe_2O_{4+\delta}$, $LuMnFeO_{4+\delta}$, $LuMnGaO_{4+\delta}$ and oxygen stoichiometry (δ) after oxygen uptake. The ratio of oxidized-to-reduced parameters (O/R) is provided to illustrate the relative structural shifts upon oxygen intercalation.

	$LuFe_2O_{4+\delta}$			$LuMnFeO_{4+\delta}$			$LuMnGaO_{4+\delta}$		
	R	O	O/R	R	O	O/R	R	O	O/R
a	3.43846(6)	3.46284(7)	1.00709(3)	3.44437(5)	3.4773(2)	1.00576(3)	3.42515(2)	3.4801(1)	1.02007(3)
c	8.4177(1)	8.4662(2)	1.00956(6)	8.578(1)	8.2492(3)	0.9617(1)	8.58737(7)	8.1714(2)	0.98013(9)
V	86.189(2)	87.919(2)	1.01604(3)	88.133(1)	86.382(8)	0.95156(2)	87.2470(7)	85.707(3)	0.98235(4)
δ	0.44(3)			0.58(3)			0.603(2)		

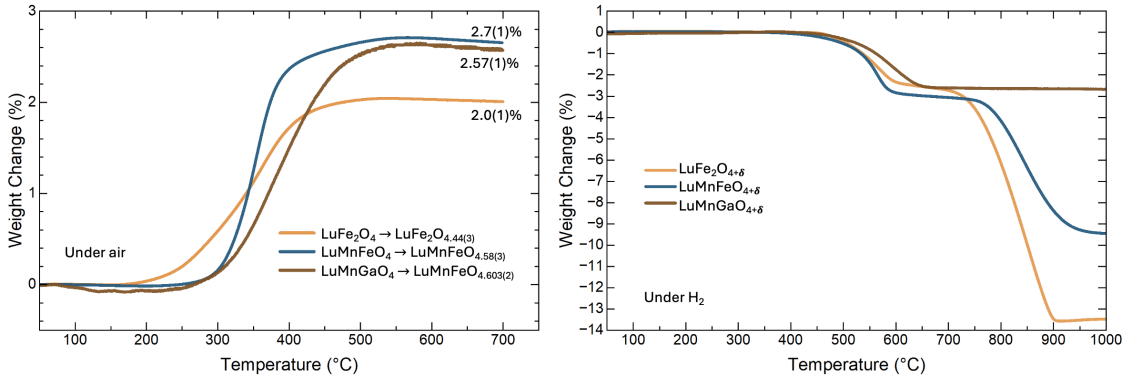


Figure 5.18: Thermogravimetric analysis (TGA) of $LuFe_2O_{4+\delta}$, $LuMnFeO_{4+\delta}$, $LuMnGaO_{4+\delta}$. (Left) Oxidation under air from 50 °C to 700 °C. (Right) Reduction under 3% H_2/Ar from 50 °C to 1000 °C.

As briefly mentioned in the previous section, a primary distinction between the $LuFe_2O_4$ and $LuMnFeO_4$ series lies in their divergent structural responses to oxidation. $LuFe_2O_4$

exhibits near-isotropic expansion of the unit cell. Conversely, $LuMnFeO_4$ and $LuMnGaO_4$ demonstrate anisotropic behavior: while the *a*- parameter expands, the *c*-parameter undergoes significant contraction. This results in a net decrease in unit cell volume upon oxidation, suggesting that the B^{2+}-site chemistry (Mn^{2+} vs Fe^{2+}) dictates the lattice response.

The isotropic expansion of $LuFe_2O_4$ is consistent with typical lattice dilation following oxygen intercalation. As oxygen anions enter the lattice, Coulombic repulsion between anions drives a global expansion of the unit cell. However, the volume contraction in Mn-substituted analogues can be explained through the lens of crystal field theory (CFT) by considering the coordination environments of the Mn ions. In the reduced phase, the transition metal cations occupy trigonal bipyramidal (TBP) sites. Upon oxidation, oxygen intercalation induces a transition toward a mixed coordination environment comprising TBP, octahedral, and tetrahedral polyhedra.

In the first case, where the coordination remains TBP, the oxidation of Mn^{2+} (d^5) to Mn^{3+} (d^4) results in the loss of an electron from the e' or e'' levels. Figure 5.19 shows the Jahn-Teller effect causing the degenerate orbital splitting of the TBP coordination. The The Jahn-Teller distortion occurs when degenerate electronic states are unequally occupied; the system undergoes a spontaneous symmetry-breaking distortion to lift this degeneracy and minimize its total energy. This electronic transition manifests as a structural distortion, typically through the stretching or compression of coordination bonds and angles [114]. As shown in Figure 5.19, the resulting d^4 state does not benefit from, has any energy gain with the Jahn-Teller stabilization in this geometry. Consequently, the TBP site remains relatively rigid.

In the second case, where Mn^{3+} (d^4) occupies an octahedral site, the ion becomes highly Jahn-Teller active. The e_g level splits to remove electronic degeneracy, allowing for two possible distortion modes. The experimental observation of *a*-axis expansion and *c*-axis contraction aligns with the axially compressed octahedral model shown in the left of

Figure 5.20. In this state, the $d_{x^2-y^2}$ orbital is lowered in energy, favoring lateral expansion in the *ab*-plane, while the destabilization of the d_{z^2} orbital correlates with the observed *c*-axis shortening. The refined bond lengths provide direct evidence for this transition from trigonal bipyramidal to octahedral coordination. For the $LuMnGaO_4$ case, the axial Mn/Ga–O1 and Mn/Ga–O2 bonds in the TBP phase are 1.861(2) Å and 2.387(2) Å, respectively; upon oxidation, these significantly contract to 1.813(9) Å and 2.037(9) Å in the octahedral environment. Conversely, the equatorial (lateral) Mn/Ga bonds expand from 2.0145(4) Å in the reduced phase to 2.024(1) Å and 2.071(2) Å in the oxidized phase.

The axial bond contraction observed in this system represents an unconventional departure from the structural behavior typically associated with Mn^{3+}. Typically, Mn^{3+} (d^4) in the octahedral coordination of perovskite or spinel structures is characterized by a pronounced axial elongation [115–117]. This is a well-known result of the Jahn-Teller effect, which lifts the degeneracy of the e_g orbitals, specifically stabilizing the d_{z^2} orbital to accommodate the single remaining electron as shown in Figure 5.20 (Right).

While the underlying mechanism for the slight axial compression observed in our system remains under investigation, we hypothesize it may be driven by the cationic ordering of Mn^{3+} and Fe^{3+} occupying equivalent sites. Furthermore, the localized strain induced by the ionic radius disparity during the Mn^{2+} to Mn^{3+} oxidation process likely plays a critical role in modulating these bond lengths. CFT only provides a simple, qualitative framework for this structural transition. Density functional theory (DFT) calculations would be required to further quantify these electronic contributions.

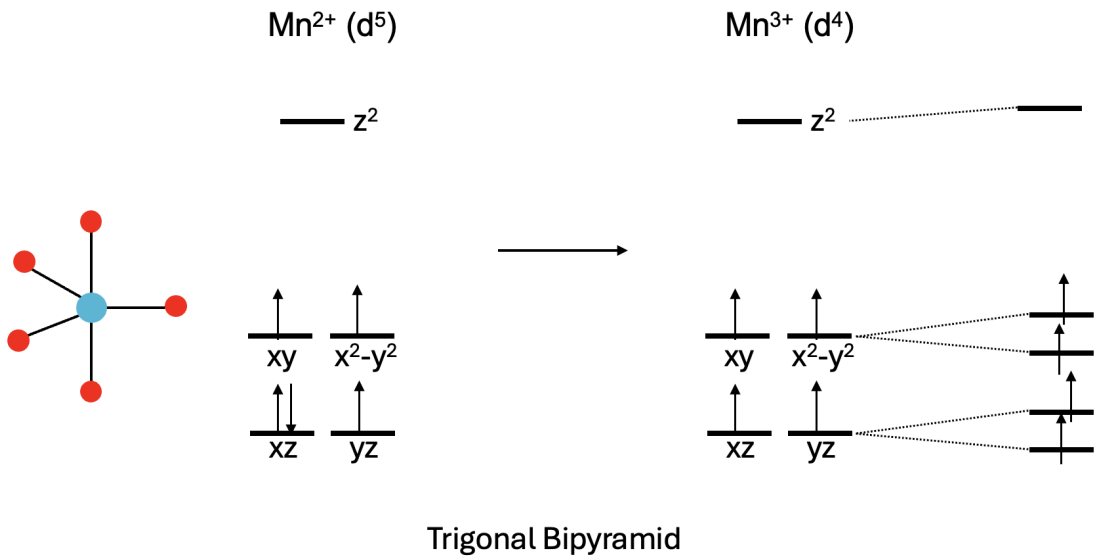


Figure 5.19: Crystal field splitting and electron configuration of high-spin Mn^{2+} (d^5) in a trigonal bipyramidal coordination.

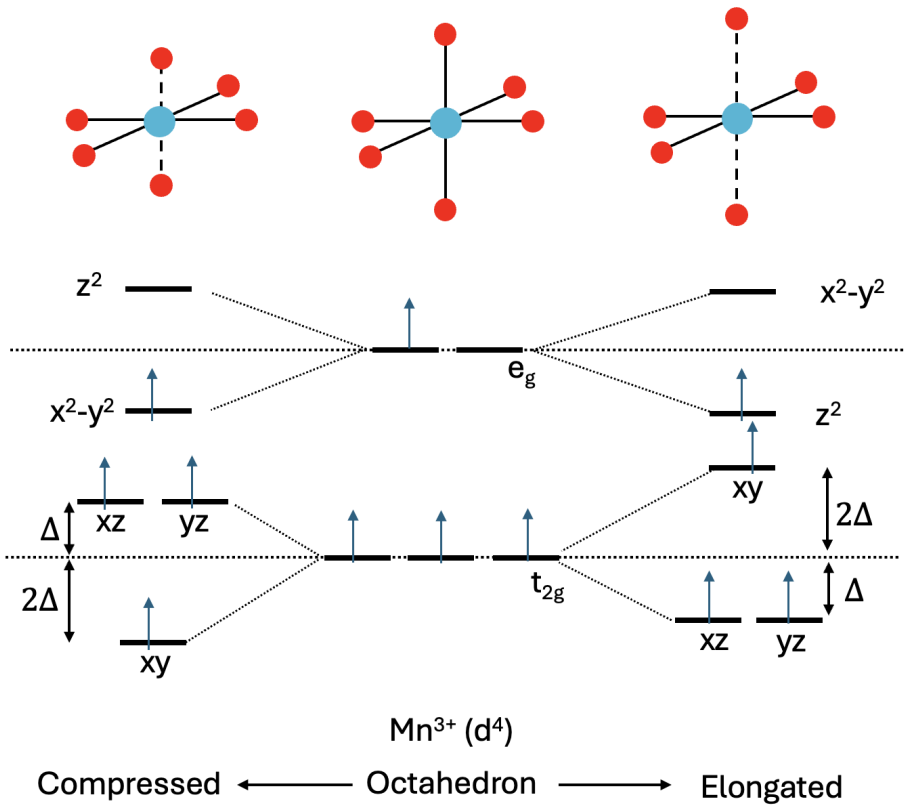


Figure 5.20: Crystal field splitting and electron configuration of high-spin Mn^{3+} (d^4) in an octahedral coordination.

The oxygen storage capacity also varies significantly between $LuFe_2O_4$ and the Mn-substituted analogues ($LuMnFeO_4$ and $LuMnGaO_4$). As summarized in Table 5.10, both Mn-containing compounds exceed the expected stoichiometry of $\delta = 0.5$ upon full oxidation, whereas $LuFe_2O_4$ remains restricted below this limit. This enhanced capacity is attributed to the flexible oxidation states of manganese. While iron is chemically restricted to the Fe^{3+} as Fe^{4+} is generally unstable in this lattice [118, 119], manganese can readily oxidize from Mn^{3+} to Mn^{4+}. The stability of the Mn^{4+} state is well-documented in literature [120–122], and its formation likly facilitates the intercalation of additional oxygen beyond the formal $O_{4.5}$ limit.

Another interesting note is the high thermal stability of $LuMnGaO_{4.5}$ under a reducing atmosphere. In the reduction TGA profiles in Figure 5.18, while $LuFe_2O_{4+\delta}$ and $LuMnFeO_{4+\delta}$ undergo structural decomposition above 700°C, $LuMnGaO_{4+\delta}$ maintains its structure up to 1000°C. This divergence is driven by the susceptibility of iron to deep reduction; in a hydrogen-rich atmosphere, Fe species readily reduce to metallic Fe^0 at elevated temperatures (650–700°C), triggering a total collapse of the parent $R\bar{3}m$ structure [123, 124]. In contrast, Ga^{3+} is a redox-inert cation that remains exceptionally stable in its trivalent state. The presence of Ga^{3+} on the B^{3+}-site acts as a structural "anchor," preventing the complete reduction of the *B*-site network and allowing the lattice to withstand significantly higher temperatures without decomposing.

The Yb-substituted ($YbFe_2O_4$, $YbMnFeO_4$, $YbMnGaO_4$) and Er-substituted ($ErFe_2O_4$, $ErMnFeO_4$) analogues exhibit similar structural changes and oxgyen storage capacities. Data regarding their lattice evolution and thermogravimeteric profiles can be found in Tables 5.11 and 5.12 and Figures 5.21 and 5.22.

Table 5.11: Refined lattice parameters (a, c), unit cell volume (V) for reduced (R) and oxidized (O) phases of $YbFe_2O_{4+\delta}$, $YbMnFeO_{4+\delta}$, $YbMnGaO_{4+\delta}$ and oxygen stoichiometry (δ) after oxygen uptake. The ratio of oxidized-to-reduced parameters (O/R) is provided to illustrate the relative structural shifts upon oxygen intercalation. The c-parameter and volume for reduced phases are normalized by 3.

	$YbFe_2O_{4+\delta}$			$YbMnFeO_{4+\delta}$			$YbMnGaO_{4+\delta}$		
	R	O	O/R	R	O	O/R	R	O	O/R
a	3.44893(1)	3.46778(1)	1.00546(4)	3.45433(2)	3.485465(9)	1.009013(6)	3.43817(1)	3.49211(5)	1.01569(1)
c	8.3668(3)	8.4397(2)	1.00870(4)	8.5274(1)	8.2295(3)	0.96507(4)	8.54381(3)	8.1513(1)	0.95406(1)
V	86.1903(7)	87.894(3)	1.01978(4)	88.120(1)	86.582(4)	0.98255(5)	87.4657(3)	86.086(1)	0.98423(1)
δ	0.46(3)			0.58(3)			0.56(3)		

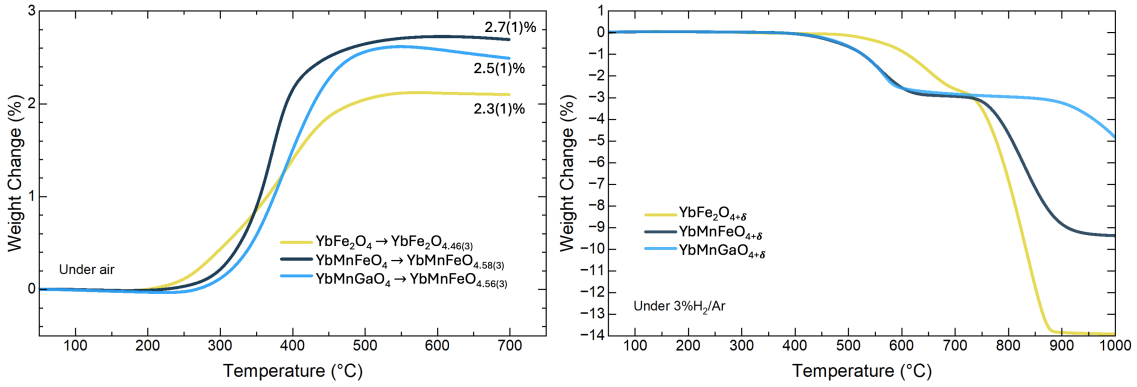


Figure 5.21: Thermogravimetric analysis (TGA) of $YbFe_2O_{4+\delta}$, $YbMnFeO_{4+\delta}$, $YbMnGaO_{4+\delta}$. (Left) Oxidation under air from 50 °C to 700 °C. (Right) Reduction under 3% H_2/Ar from 50 °C to 1000 °C.

Table 5.12: Refined lattice parameters (a, c), unit cell volume (V) for reduced (R) and oxidized (O) phases of $ErFe_2O_{4+\delta}$ and $ErMnFeO_{4+\delta}$ and oxygen stoichiometry (δ) after oxygen uptake. The ratio of oxidized-to-reduced parameters (O/R) is provided to illustrate the relative structural shifts upon oxygen intercalation. The c-parameter and volume for reduced phases are normalized by 3.

	$ErFe_2O_{4+\delta}$			$ErMnFeO_{4+\delta}$		
	R	O	O/R	R	O	O/R
a	3.49169(4)	3.52183(6)	1.00863(2)	3.47986(7)	3.50546(9)	1.00737(3)
c	8.3096(7)	8.3731(1)	1.00764(1)	8.5186(1)	8.2526(2)	0.96876(3)
V	87.7367(1)	89.940(2)	1.02512(3)	88.336(2)	87.823(4)	0.99416(5)
δ		0.49(3)			0.63(3)	

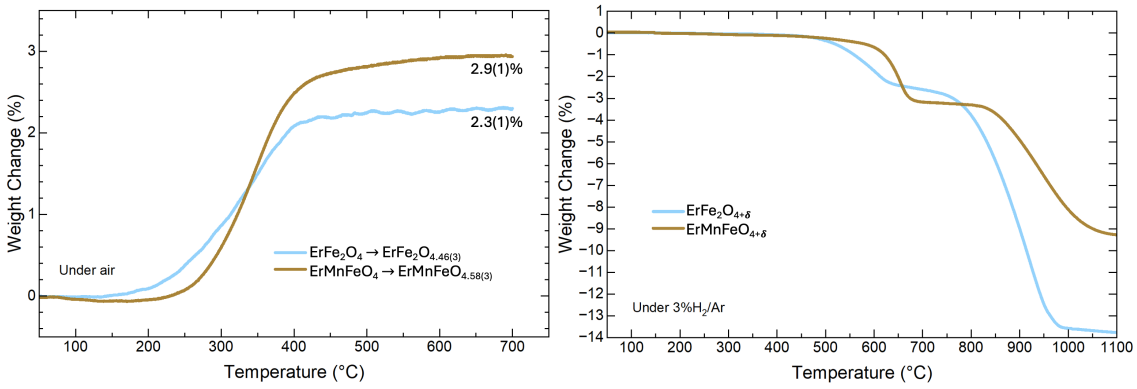


Figure 5.22: Thermogravimetric analysis (TGA) of $ErFe_2O_{4+\delta}$ and $ErMnFeO_{4+\delta}$. (Left) Oxidation under air from 50 °C to 700 °C. (Right) Reduction under 3% H_2/Ar from 50 °C to 1100 °C.

5.4 Conclusion

This chapter presented a systematic investigation into the effects of *A*- and *B*-site substitution on the structural evolution and oxygen storage behavior of $AB_2O_{4+\delta}$ compounds.

The results indicate that the *A*-site ionic radius influences lattice size. Across all investigated series, increasing the *A*-site radius consistently expanded the *a*-axis and unit cell volume in the reduced state, a result of steric effects within the $A-O$ framework. Larger *A*-site cations generally facilitated a higher degree of oxygen intercalation, likely due to the increased interstitial space provided by the expanded lattice. Conversely, smaller *A*-site cations induced more severe structural shifts upon oxidation, specifically a pronounced contraction along the *c*-axis, which may negatively impact long-term material stability and cyclability.

A significant finding is the divergent structural response to oxidation based on *B*-site occupancy. The $A\mathrm{Fe_2O_4}$ series undergoes an expansion in both the *ab*-plane and the *c*-direction upon oxidation, representing a typical lattice dilation following oxygen intercalation. Interestingly, the $A\mathrm{MnFeO_4}$ and $A\mathrm{MnGaO_4}$ series exhibit a contraction in the *c*-lattice parameter and overall unit cell volume upon oxygen uptake. This phenomenon is likely driven by the changing coordination environment and effective ironic radii of manganese (Mn^{2+} to Mn^{3+}) on the *B*-site. The unconventional compression of the axial bonds within the octahedral coordination of Mn^{3+} warrants further investigation. The $A\mathrm{Fe_2O_4}$ series demonstrated lower oxygen stoichiometry and higher metastability than the Mn-and Ga-substituted analogues. The reduction experiments confirmed that the oxygen uptake is reversible, however materials containing Fe are susceptible to decomposition into consituent oxides and elemental Fe at temperatures exceeding 750°C under reducing atmospheres.

Chapter 6: Conclusions and Future Directions

This dissertation provided a comprehensive investigation into the structural evolution and redox behavior of hexagonal AB_2O_4 type oxygen storage materials. Unlike conventional cubic fluorite and perovskite materials, which rely on vacancy formation and annihilation to transport oxygen, these hexagonal AB_2O_4 compounds utilize a topotactic phase transition. This mechanism involves the sliding of AO_6 layers to incorporate oxygen at lower temperatures. We first focused on $LuMnGaO_4$ using neutron and synchrotron X-ray diffraction to unveil the complex oxygen disorder within its oxidized phase. Alongside these oxygen storage properties, we investigated a notable colorimetric transition from greenish-grey in the reduced state to black upon oxidation which highlights the material's potential for optical oxygen sensing.

Subsequent research investigated the impact of *A*-site substitution, revealing that $InMnGaO_4$ does not exhibit oxygen storage behavior despite adapting the same $R\bar{3}m$ structure as other reduced phases. This finding underscores the critical role of *A*-site cation selection in supporting the structural framework required for $AB_2O_{4+\delta}$ stability. A broader survey of *A*-site (Lu, Yb, Er, Y) and *B*-site (Mn, Fe, Ga) substitutions established key design principles: Larger *A*-site cations increase unit cell volume, which facilitates higher degrees of oxygen intercalation and the B^{2+} cation dictates the structural response to oxidation. Manganese-containing oxides showed an anisotropic contraction (*c*-axis contraction with *ab*-plane expansion), resulting in an overall volume decrease. In contrast, the AFe_2O_4 series showed a near-isotropic expansion. This unit cell compression in Mn-phases is attributed to

the unconventional compression of the Mn^{3+} octahedral coordination.

Now that we have a thorough fundamental structural understanding of the materials, the next step will be testing the practical applicability. We are specifically interested in testing these materials for solar thermochemical water splitting (STWS) and solid oxide fuel cells (SOFCs).

Thermogravimetric analysis (TGA) has provided precise temperature ranges for the oxidation (in air) and reduction (in 3% H_2/Ar) of each compound. Future studies will leverage these parameters to perform long-term cycling measurements, evaluating the kinetics and structural stability of these materials over repeated redox cycles.

To evaluate STWS viability, future work must transition from air-based oxidation to steam-based oxidation. While we have confirmed the ability of these materials to uptake oxygen from the atmosphere, their capability to split water molecules to produce hydrogen remains to be tested. Steam-exposure experiments coupled with mass spectrometry would quantify the hydrogen yield and the materials' stability under hydrothermal conditions [125, 126].

For SOFC applications, the chemical and mechanical compatibility of $AB_2O_{4+\delta}$ materials with standard cell components is a critical hurdle. Future research should focus on testing the potential interfacial reactions between the AB_2O_4 phases and common electrolytes, such as Gadolinium-doped Ceria (GDC) or Yttria-stabilized Zirconia (YSZ) at relevant operating temperatures [14, 15].

Bibliography

[1] Mir Sayed Shah Danish, Arnab Bhattacharya, Diana Stepanova, Alexey Mikhaylov, Maria Luisa Grilli, Mahdi Khosravy, and Tomonobu Senjyu. A systematic review of metal oxide applications for energy and environmental sustainability. *Metals*, 10(12):1604, 2020.

[2] Goutam Kumar Dalapati, Himani Sharma, Asim Guchhait, Nilanjan Chakrabarty, Priyanka Bamola, Qian Liu, Gopalan Saianand, Ambati Mounika Sai Krishna, Sabyasachi Mukhopadhyay, Avishek Dey, Terence Kin Shun Wong, Siarhei Zhuk, Siddhartha Ghosh, Sabyasachi Chakrabortty, Chandreswar Mahata, Sajal Biring, Avishek Kumar, Camila Silva Ribeiro, Seeram Ramakrishna, Amit K. Chakraborty, Satheesh Krishnamurthy, Prashant Sonar, and Mohit Sharma. Tin oxide for optoelectronic, photovoltaic and energy storage devices: a review. *Journal of Materials Chemistry A*, 9(31):16621–16684, 2021.

[3] Taposhree Dutta, Tanzila Noushin, Shawana Tabassum, and Satyendra K. Mishra. Road map of semiconductor metal-oxide-based sensors: A review. *Sensors*, 23(15):6849, 2023.

[4] Anna Isabel Hofmann, Eric Cloutet, and Georges Hadziioannou. Materials for transparent electrodes: From metal oxides to organic alternatives. *Advanced Electronic Materials*, 4(10), 2018.

[5] Maria Luisa Grilli. Metal oxides. *Metals*, 10(6):820, 2020.

[6] Tiziano Montini, Michele Melchionna, Matteo Monai, and Paolo Fornasiero. Fundamentals and catalytic applications of CeO2-based materials. *Chemical Reviews*, 116(10):5987–6041, 2016.

[7] R. D. Shannon. Revised effective ionic radii and systematic studies of interatomic distances in halides and chalcogenides. *Acta Crystallographica A*, pages 751 – 767, 1976.

[8] Neelima Mahato, Alka Gupta, and Kantesh Balani. Doped zirconia and ceria-based electrolytes for solid oxide fuel cells: a review. *Nanomaterials and Energy*, 1(1):27–45, 2015.

[9] Masatomo Yashima, Hiroyuki Takashina, Masato Kakihana, and Masahiro Yoshimura. Low-temperature phase equilibria by the flux method and the metastable–stable phase diagram in the ZrO2–CeO2 system. *Journal of the American Ceramic Society*, 77(7):1869–1874, 1994.

[10] Y. Madier, C. Descorme, A. M. Le Govic, and D. Duprez. Oxygen mobility in CeO2 and ce x zr(1 - x)o2 compounds: Study by CO transient oxidation and 18o/16o isotopic exchange. *The Journal of Physical Chemistry B*, 103(50):10999–11006, 1999.

[11] Yuhua Wu, Zilin Yan, Jiawei Xu, Zheng Zhong, and Xinhai Xu. Insight into mechanism of boosted oxygen reduction reaction in mixed-conducting composite cathode of solid oxide fuel cell via a novel open-source pore-scale model. *Chemical Engineering Journal*, 469:143854, 2023.

[12] M.A. Laguna-Bercero. Reference module in earth systems and environmental sciences. pages 331–341, 2017.

[13] Navadol Laosiripojana, Wisitsree Wiyaratn, Worapon Kiatkittipong, Arnornchai Arpornwichanop, Apinan Soottitantawat, and Suttichai Assabumrungrat. Reviews on solid oxide fuel cell technology. *Engineering Journal*, 13(1):65–84, 2009.

[14] Jeffrey W. Fergus. Electrolytes for solid oxide fuel cells. *Journal of Power Sources*, 162(1):30–40, 2006.

[15] Saddam Hussain and Li Yangping. Review of solid oxide fuel cell materials: cathode, anode, and electrolyte. *Energy Transitions*, 4(2):113–126, 2020.

[16] Francesco Bozza, Riccardo Polini, and Enrico Traversa. High performance anode-supported intermediate temperature solid oxide fuel cells (IT-SOFCs) with la0.8sr0.2ga0.8mg0.2o3 electrolyte films prepared by electrophoretic deposition. *Electrochemistry Communications*, 11(8):1680–1683, 2009.

[17] Alidad Mohammadi, Tsung-han Wu, Alevtina L. Smirnova, Jakub Pusz, and Nigel M. Sammes. All-perovskite solid oxide fuel cells, synthesis and characterization. *Journal of Fuel Cell Science and Technology*, 6(2):021308, 2009.

[18] Kening Sun, Jing Zhang, Taizhi Jiang, Jinshuo Qiao, Wang Sun, David Rooney, and Zhenhua Wang. Flash-sintering and characterization of la0.8sr0.2ga0.8mg0.2o3-electrolytes for solid oxide fuel cells. *Electrochimica Acta*, 196:487–495, 2016.

[19] Furat Dawood, Martin Anda, and G.M. Shafiullah. Hydrogen production for energy: An overview. *International Journal of Hydrogen Energy*, 45(7):3847–3869, 2020.

[20] Pavlos Nikolaidis and Andreas Poullikkas. A comparative overview of hydrogen production processes. *Renewable and Sustainable Energy Reviews*, 67:597–611, 2017.

[21] M. Hermesmann and T.E. Müller. Green, turquoise, blue, or grey? environmentally friendly hydrogen production in transforming energy systems. *Progress in Energy and Combustion Science*, 90:100996, 2022.

[22] Marian Chatenet, Bruno G. Pollet, Dario R. Dekel, Fabio Dionigi, Jonathan Deseure, Pierre Millet, Richard D. Braatz, Martin Z. Bazant, Michael Eikerling, Iain Staffell, Paul Balcombe, Yang Shao-Horn, and Helmut Schäfer. Water electrolysis: from textbook knowledge to the latest scientific strategies and industrial developments. *Chemical Society Reviews*, 51(11):4583–4762, 2022.

[23] Marcus Newborough and Graham Cooley. Developments in the global hydrogen market: The spectrum of hydrogen colours. *Fuel Cells Bulletin*, 2020(11):16–22, 2020.

[24] Akira Fujishima and Kenichi Honda. Electrochemical photolysis of water at a semiconductor electrode. *Nature*, 238(5358):37–38, 1972.

[25] Debora R. Barcellos, Michael D. Sanders, Jianhua Tong, Anthony H. McDaniel, and Ryan P. O'Hayre. BaCe 0.25 mn 0.75 o 3 —a promising perovskite-type oxide for solar thermochemical hydrogen production. *Energy & Environmental Science*, 11(11):3256–3265, 2018.

[26] Stéphane Abanades. Metal oxides applied to thermochemical water-splitting for hydrogen production using concentrated solar energy. *ChemEngineering*, 3(3):63, 2019.

[27] William C. Chueh and Sossina M. Haile. A thermochemical study of ceria: exploiting an old material for new modes of energy conversion and CO2 mitigation. *Philosophical Transactions of the Royal Society A: Mathematical, Physical and Engineering Sciences*, 368(1923):3269–3294, 2010.

[28] William C. Chueh and Sossina M. Haile. Ceria as a thermochemical reaction medium for selectively generating syngas or methane from h2o and CO2. *ChemSusChem*, 2(8):735–739, 2009.

[29] Anthony H. McDaniel, Elizabeth C. Miller, Darwin Arifin, Andrea Ambrosini, Eric N. Coker, Ryan O'Hayre, William C. Chueh, and Jianhua Tong. Sr- and mn-doped LaAlO 3 for solar thermochemical h 2 and CO production. *Energy & Environmental Science*, 6(8):2424–2428, 2013.

[30] Shuai He, Yuanfeng Zou, Kongfa Chen, and San P. Jiang. A critical review of key materials and issues in solid oxide cells. *Interdisciplinary Materials*, 2(1):111–136, 2023.

[31] Nathan P. Siegel, James E. Miller, Ivan Ermanoski, Richard B. Diver, and Ellen B. Stechel. Factors affecting the efficiency of solar driven metal oxide thermochemical cycles. *Industrial & Engineering Chemistry Research*, 52(9):3276–3286, 2013.

[32] Anita Haeussler, Stéphane Abanades, Julien Jouannaux, and Anne Julbe. Non-stoichiometric redox active perovskite materials for solar thermochemical fuel production: A review. *Catalysts*, 8(12):611, 2018.

[33] N. Kimizuka, A. Takenaka, Y. Sasada, and T. Katsura. A series of new compounds a3+fe2 o4 (a = ho, er, tm, yb, and lu). *Solid State Communications*, 15(8):1321–1323, 1974.

[34] Noboru Kimizuka and Eiji Takayama. Ln(fe3+m2+)o4 compounds with layer structure [ln : Y, er, tm, yb, and lu, m : Mg, mn, co, cu, and zn]. *Journal of Solid State Chemistry*, 40(1):109–116, 1981.

[35] Noboru Kimizuka and Eiji Takayama. Survey of the phase formation in the yb2o3ga2o3MO and yb2o3cr2o3MO systems in air at high temperatures (m: Co, ni, cu, and zn). *Journal of Solid State Chemistry*, 43(3):278–284, 1982.

[36] Noboru Kimizuka and Eiji Takayama. Ln(GaM2+)o4 and ln(AlMn2+)o4 compounds having a layer structure [ln = lu, yb, tm, er, ho, and y, and m = mg, mn, co, cu, and zn]. *Journal of Solid State Chemistry*, 41(2):166–173, 1982.

[37] M. Isobe, N. Kimizuka, J. Iida, and S. Takekawa. Structures of LuFeCoO4 and LuFe2o4. *Acta Crystallographica Section C*, 46(10):1917–1918, 1990.

[38] Noboru Kimizuka and Takahiko Mohri. Structural classification ofRAO3(MO)n compounds (r =sc, in, y, or lanthanides; a =fe(III), ga, cr, or al; m =divalent cation; n = 1–11). *Journal of Solid State Chemistry*, 78(1):98–107, 1989.

[39] Satoru Funahashi, Jun Akimitsu, Kiiti Siratori, Noboru Kimizuka, Midori Tanaka, and Hideshi Fujishita. Two-dimensional spin correlation in YFe2o4. *Journal of the Physical Society of Japan*, 53(8):2688–2696, 1984.

[40] Naoshi Ikeda, Kay Kohn, Nobuyuki Myouga, Eri Takahashi, Hijiri Kitôh, and Shunji Takekawa. Charge frustration and dielectric dispersion in LuFe2o4. *Journal of the Physical Society of Japan*, 69(5):1526–1532, 2000.

[41] Naoshi Ikeda, Hiroyuki Ohsumi, Kenji Ohwada, Kenji Ishii, Toshiya Inami, Kazuhisa Kakurai, Youichi Murakami, Kenji Yoshii, Shigeo Mori, Yoichi Horibe, and Hijiri Kitô. Ferroelectricity from iron valence ordering in the charge-frustrated system LuFe2o4. *Nature*, 436(7054):1136–1138, 2005.

[42] Sang-Wook Cheong and Maxim Mostovoy. Multiferroics: a magnetic twist for ferroelectricity. *Nature Materials*, 6(1):13–20, 2007.

[43] N. Ikeda, S. Mori, K. Yoshii, and Y. Matsuo. Electronic ferroelectricity from charge ordering in RFe2o4. *2007 Sixteenth IEEE International Symposium on the Applications of Ferroelectrics*, pages 253–254, 2007.

[44] Rosa Grajczyk and M.A. Subramanian. Structure–property relationships of YbFe2o4– and yb2fe3o7–type layered oxides: A bird's eye view. *Progress in Solid State Chemistry*, 43(1-2):37–46, 2015.

[45] M. Hervieu, A. Guesdon, J. Bourgeois, E. Elkaïm, M. Poienar, F. Damay, J. Rouquette, A. Maignan, and C. Martin. Oxygen storage capacity and structural flexibility of LuFe2o4+x (0x0.5). *Nature Materials*, 13(1):74–80, 2014.

[46] M. Hervieu, F. Damay, A. Maignan, and C. Martin. Rare earth ferrites LuFe2o4x polymorphism, polytypism and metastable phases. *Solid State Sciences*, 48:A1–A16, 2015.

[47] M. Hervieu, F. Damay, M. Poienar, E. Elkaïm, J. Rouquette, A.M. Abakumov, G. Van Tendeloo, A. Maignan, and C. Martin. Nanostructures in LuFe2o4+. *Solid State Sciences*, 23:26–34, 2013.

[48] R. S. Jayathilake, B. D. Levitas, and E. E. Rodriguez. In situ diffraction studies on reversible oxygen uptake and release in AFe 2 o 4 + (a= lu, yb, y, and in). *Journal of Materials Chemistry A*, 6(11):4801–4810, 2018.

[49] Tianyu Li, Rishvi Jayathilake, Lahari Balisetty, Yuan Zhang, Brandon Wilfong, Timothy J. Diethrich, and Efrain E. Rodriguez. Crystal field-induced lattice expansion upon reversible oxygen uptake/release in YbMn x fe 2x o 4. *Materials Advances*, 3(2):1087–1100, 2021.

[50] Tianyu Li, Sz-Chian Liou, Stephanie J. Hong, Qiang Zhang, H. Cein Mandujano, and Efrain E. Rodriguez. Structural modulation and spin glassiness upon oxidation in oxygen storage material LnFeMnO4+x for ln = y, lu, and yb. *APL Materials*, 11(6):061120, 2023.

[51] Stephanie Jinhwa Hong, Tianyu Li, H. Cein Mandujano, Alicia Manjón-Sanz, SzChian Liou, Yuchen Niu, and Efrain E Rodriguez. Reversible structural and colorimetric transitions in LuMnGaO 4 upon oxygen uptake and release. *Dalton Transactions*, 2025.

[52] Anthony R. West. *Solid State Chemistry and its Applications*. Wiley, 2014.

[53] International Union of Crystallography. Crystal. Online Dictionary of Crystallography, 2021. Accessed: 2024-05-22.

[54] Vitalij K. Pecharsky and Peter Y. Zavalij. *Fundamentals of Powder Diffraction and Structural Characterization of Materials*. Springer, New York, NY, 2nd edition, 2009.

[55] S. P. Thompson, J. E. Parker, J. Potter, T. P. Hill, A. Birt, T. M. Cobb, F. Yuan, and C. C. Tang. Beamline i11 at diamond: A new instrument for high resolution powder diffraction. *Review of Scientific Instruments*, 80(7):075107, 2009.

[56] Erich H Kisi and Christopher J Howard. *Applications of Neutron Powder Diffraction*, volume 15 of *Oxford Series on Neutron Scattering in Condensed Matter*. Oxford University Press, Oxford, UK, 2008.

[57] Tapan Chatterji, editor. *Neutron Scattering from Magnetic Materials*. Elsevier Science, Amsterdam, 2006.

[58] Ashfia Huq, Melanie Kirkham, Peter F. Peterson, Jason P. Hodges, Pamela S. Whitfield, Katharine Page, Thomas Hűgle, Erik B. Iverson, Andre Parizzi, and George Rennich. POWGEN: rebuild of a third-generation powder diffractometer at the spallation neutron source. *Journal of Applied Crystallography*, 52(Pt 5):1189–1201, 2019.

[59] Brian H. Toby and Robert B. Von Dreele. GSAS-II: the genesis of a modern open-source all purpose crystallography software package. *Journal of Applied Crystallography*, 46(2):544–549, 2013.

[60] A.A. Coelho. TOPAS and TOPAS-academic: an optimization program integrating computer algebra and crystallographic objects written in c++. *Journal of Applied Crystallography*, 51(1):210–218, 2018.

[61] H. M. Rietveld. A profile refinement method for nuclear and magnetic structures. *Journal of Applied Crystallography*, 2(2):65–71, 1969.

[62] Hugo M Rietveld. Line profiles of neutron powder-diffraction peaks for structure refinement. *Acta Crystallographica*, 22(1):151–152, 1967.

[63] R A Young. *The Rietveld Method*. Oxford University Press, 04 1993.

[64] Bertram Eugene Warren. *X-ray Diffraction*. Addison-Wesley Pub. Co., Reading, Mass., 1969.

[65] Jeremy Karl Cockcroft. Whole pattern fitting: Ii. LeBail method. Birkbeck College, University of London, online course material, 1997–2006. Accessed: 2024-05-22.

[66] Sarah Nicoud, Marielle Huve, Olivier Hernandez, Alain Pautrat, Mathieu Duttine, Alain Wattiaux, Claire Colin, Houria Kabbour, and Olivier Mentre. Comprehensive study of oxygen storage in YbFe2o4+x (x 0.5): Unprecedented coexistence of FeO n polyhedra in one single phase. *Journal of the American Chemical Society*, 139(47):17031–17043, 2017.

[67] R. Ramamoorthy, P. K. Dutta, and S. A. Akbar. Oxygen sensors: Materials, methods, designs and applications. *Journal of Materials Science*, 38(21):4271–4282, 2003.

[68] Xiangpeng Meng, Saehoon Kim, Pradeep Puligundla, and Sanghoon Ko. Carbon dioxide and oxygen gas sensors-possible application for monitoring quality, freshness, and safety of agricultural and food products with emphasis on importance of analytical signals and their transformation. *Journal of the Korean Society for Applied Biological Chemistry*, 57(6):723–733, 12 2014.

[69] Andreas W. Hempel, Dmitri B. Papkovsky, and Joseph P. Kerry. Use of optical oxygen sensors in non-destructively determining the levels of oxygen present in combined vacuum and modified atmosphere packaged pre-cooked convenience-style foods and the use of ethanol emitters to extend product shelf-life. *Foods*, 2(4):507–520, 2013.

[70] Xu-dong Wang and Otto S. Wolfbeis. Optical methods for sensing and imaging oxygen: materials, spectroscopies and applications. *Chemical Society Reviews*, 43(10):3666–3761, 2014.

[71] Johannes W. Schwank and Michael DiBattista. Oxygen sensors: Materials and applications. *MRS Bulletin*, 24(6):44–48, 1999.

[72] Wojciech Bulowski, Rafał Knura, Robert P. Socha, Maciej Basiura, Katarzyna Skibińska, and Marek Wojnicki. Thin film semiconductor metal oxide oxygen sensors: Limitations, challenges, and future progress. *Electronics*, 13(17):3409, 2024.

[73] V. Di Castro and G. Polzonetti. XPS study of MnO oxidation. *Journal of Electron Spectroscopy and Related Phenomena*, 48(1):117–123, 1989.

[74] H.W. Nesbitt and D. Banerjee. Interpretation of XPS mn(2p) spectra of mn oxyhydroxides and constraints on the mechanism of MnO2 precipitation. *American Mineralogist*, 83(3-4):305–315, 1998.

[75] Eugene S. Ilton, Jeffrey E. Post, Peter J. Heaney, Florence T. Ling, and Sebastien N. Kerisit. XPS determination of mn oxidation states in mn (hydr)oxides. *Applied Surface Science*, 366:475–485, 2016.

[76] Jose M. Cerrato, Michael F. Hochella, William R. Knocke, Andrea M. Dietrich, and Thomas F. Cromer. Use of XPS to identify the oxidation state of mn in solid surfaces of filtration media oxide samples from drinking water treatment plants. *Environmental Science & Technology*, 44(15):5881–5886, 2010.

[77] A. Abragam and B. Bleaney. *Electron Paramagnetic Resonance of Tranition Ion*. Dover Publications, 7 2012.

[78] Junji Iida, Midori Tanaka, and Yasuaki Nakagawa. Magnetization of single crystal YFeMnO4. *Journal of the Physical Society of Japan*, 59(12):4443–4448, 1990.

[79] Mitsumasa Isobe, Massimo Nespolo, Junji Iida, and Noboru Kimizuka. Crystal structure and charge distribution of YbFeMnO4. *Acta Crystallographica Section B*, 56(5):805–810, 2000.

[80] R.J. Cava, A.P. Ramirez, Q. Huang, and J.J. Krajewski. Compounds with the YbFe2o4structure type: Frustrated magnetism and spin-glass behavior. *Journal of Solid State Chemistry*, 140(2):337–344, 1998.

[81] J. Bourgeois, M. Hervieu, M. Poienar, A. M. Abakumov, E. Elkaïm, M. T. Sougrati, F. Porcher, F. Damay, J. Rouquette, G. Van Tendeloo, A. Maignan, J. Haines, and C. Martin. Evidence of oxygen-dependent modulation in LuFe2o4. *Physical Review B*, 85(6):064102, 2012.

[82] Shiqing Deng, Lijun Wu, Hao Cheng, Jin-Cheng Zheng, Shaobo Cheng, Jun Li, Wenbin Wang, Jian Shen, Jing Tao, Jing Zhu, and Yimei Zhu. Charge-lattice coupling in hole-doped LuFe2o4+: The origin of second-order modulation. *Physical Review Letters*, 122(12):126401, 2019.

[83] Andrew E. Smith, Hiroshi Mizoguchi, Kris Delaney, Nicola A. Spaldin, Arthur W. Sleight, and M. A. Subramanian. Mn3+ in trigonal bipyramidal coordination: A new blue chromophore. *Journal of the American Chemical Society*, 131(47):17084–17086, 2009.

[84] Jun Li and M.A. Subramanian. Inorganic pigments with transition metal chromophores at trigonal bipyramidal coordination: Y(in,mn)o3 blues and beyond. *Journal of Solid State Chemistry*, 272:9–20, 2019.

[85] Andrew E. Smith, Matthew C. Comstock, and M.A. Subramanian. Spectral properties of the UV absorbing and near-IR reflecting blue pigment, YIn1-xMnxO3. *Dyes and Pigments*, 133:214–221, 2016.

[86] P. Kubelka and F. Munk. Ein beitrag zur optik der farbanstriche. *Z. Techn. Phys.*, 12:593–601, 1931.

[87] G. R. Levi. The crystal structure of MnO. *Rendiconti dell'Istituto Lombardo di Science e Lettere Classe di Science Mathematiche e Naturali*, 57:619–624, 1924.

[88] Jinjia Liu, Tao Yang, Aiju Xu, Richard L. Martin, Yong Yang, Haijun Jiao, Yongwang Li, and Xiao-Dong Wen. Predication of screened hybrid functional on transition metal monoxides: From mott insulator to charge transfer insulator. *Journal of Alloys and Compounds*, 808:151707, 2019.

[89] A Fujimori, N Kimizuka, T Akahane, T Chiba, S Kimura, F Minami, K Siratori, M Taniguchi, S Ogawa, and S Suga. Electronic structure of MnO. *Physical Review B*, 42(12):7580–7586, 1990.

[90] B. K. Pandey, A. K. Shahi, and R. Gopal. Optical and electrical transport properties of MnO nanoparticles. *Materials Focus*, 2(3):221–226, 2013.

[91] Bin Liu, Jinyin Zhuang, and Gang Wei. Recent advances in the design of colorimetric sensors for environmental monitoring. *Environmental Science: Nano*, 7(8):2195–2213, 2020.

[92] Reddicherla Umapathi, Sonam Sonwal, Min Ji Lee, Gokana Mohana Rani, Eun-Seon Lee, Tae-Joon Jeon, Sung-Min Kang, Mi-Hwa Oh, and Yun Suk Huh. Colorimetric based on-site sensing strategies for the rapid detection of pesticides in agricultural foods: New horizons, perspectives, and challenges. *Coordination Chemistry Reviews*, 446:214061, 2021.

[93] Zhicheng Jin, Wonjun Yim, Maurice Retout, Emily Housel, Wenbin Zhong, Jiajing Zhou, Michael S. Strano, and Jesse V. Jokerst. Colorimetric sensing for translational applications: from colorants to mechanisms. *Chem. Soc. Rev.*, 53:7681–7741, 2024.

[94] Khushboo Gupta, O. P. Thakur, and Manish Kumar. Effect of a-site substitution on LaMnO3 perovskite via sr ions for energy applications. *Journal of Electronic Materials*, 52(7):4279–4288, 2023.

[95] Yidan Zhang, Fuxu Feng, Chuanhui Zhang, Qilong Zheng, Chunchang Wang, Haibo Hu, Mingzai Wu, and Youmin Guo. Enhanced catalytic activity of LaMnO3 by a-site substitution as air electrode of zn–air batteries with attractive durability. *Energy & Fuels*, 34(8):10170–10177, 2020.

[96] Pian Pian Ma, Qiu Ling Lu, Na Lei, Yong Kun Liu, Bo Yu, Jian Ming Dai, Shu Hong Li, and Guo Hua Jiang. Effect of a-site substitution by ca or sr on the structure and electrochemical performance of LaMnO3 perovskite. *Electrochimica Acta*, 332:135489, 2020.

[97] P. Muhammed Shafi, Debananda Mohapatra, V. Pradeep Reddy, Ganesh Dhakal, Deivasigamani Ranjith Kumar, Dirk Tuma, Thierry Brousse, and Jae-Jin Shim. Sr- and fe-substituted LaMnO3 perovskite: Fundamental insight and possible use in asymmetric hybrid supercapacitor. *Energy Storage Materials*, 45:119–129, 2022.

[98] María Luisa Medarde. Structural, magnetic and electronic properties of perovskites (r = rare earth). *Journal of Physics: Condensed Matter*, 9(8):1679, 1997.

[99] Yuesheng Li. YbMgGaO4: A triangular-lattice quantum spin liquid candidate. *Advanced Quantum Technologies*, 2(12), 2019.

[100] F. L. Pratt, F. Lang, W. Steinhardt, S. Haravifard, and S. J. Blundell. Spin dynamics, entanglement, and the nature of the spin liquid state in YbZnGaO4. *Physical Review B*, 106(6):L060401, 2022.

[101] Juan R. Chamorro, Tyrel M. McQueen, and Thao T. Tran. Chemistry of quantum spin liquids. *Chemical Reviews*, 121(5):2898–2934, 2021.

[102] Sam Mugiraneza and Alannah M. Hallas. Tutorial: a beginner's guide to interpreting magnetic susceptibility data with the curie-weiss law. *Communications Physics*, 5(1):95, 2022.

[103] Stephen Blundell. Magnetism in condensed matter. 2001.

[104] Dheeraj Ranaut and K. Mukherjee. Van vleck paramagnetism and enhancement of effective moment with magnetic field in rare earth orthovanadate EuVO4. *Physics Letters A*, 465:128710, 2023.

[105] A P Ramirez. Strongly geometrically frustrated magnets. *Annual Review of Materials Science*, 24(1):453–480, 1994.

[106] Tenzin Dawa and Baharak Sajjadi. Exploring the potential of perovskite structures for chemical looping technology: A state-of-the-art review. *Fuel Processing Technology*, 253:108022, 2024.

[107] M. Ezbiri, M. Takacs, D. Theiler, R. Michalsky, and A. Steinfeld. Tunable thermodynamic activity of la x sr 1x mn y al 1y o 3 (0 x 1, 0 y 1) perovskites for solar thermochemical fuel synthesis. *Journal of Materials Chemistry A*, 5(8):4172–4182, 2017.

[108] Cijie Liu, Jiyun Park, Héctor A. De Santiago, Boyuan Xu, Wei Li, Dawei Zhang, Lingfeng Zhou, Yue Qi, Jian Luo, and Xingbo Liu. Perovskite oxide materials for solar thermochemical hydrogen production from water splitting through chemical looping. *ACS Catal.*, 14(19):14974–15013, 10 2024. doi: 10.1021/acscatal.4c03357.

[109] Rui Ran, Xiaodong Wu, Duan Weng, and Jun Fan. Oxygen storage capacity and structural properties of ni-doped LaMnO3 perovskites. *Journal of Alloys and Compounds*, 577:288–294, 2013.

[110] María Orfila, María Linares, Raúl Molina, Juan Ángel Botas, Raúl Sanz, and Javier Marugán. Perovskite materials for hydrogen production by thermochemical water splitting. *International Journal of Hydrogen Energy*, 41(42):19329–19338, 2016.

[111] Sunita Dey, B. S. Naidu, and C. N. R. Rao. Ln0.5a0.5mno3 (ln=lanthanide, a= ca, sr) perovskites exhibiting remarkable performance in the thermochemical generation of CO and h2 from CO2 and h2o. *Chemistry – A European Journal*, 21(19):7077–7081, 2015.

[112] Nobuyuki Gokon, Kazuki Hara, Yuta Sugiyama, Selvan Bellan, Tatsuya Kodama, and Cho Hyun-seok. Thermochemical two-step water splitting cycle using perovskite oxides based on LaSrMnO3 redox system for solar h2 production. *Thermochimica Acta*, 680:178374, 2019.

[113] R.D. Shannon and C.T. Prewitt. Effective ionic radii in oxides and fluorides. *Acta Crystallographica Section B: Structural Crystallography and Crystal Chemistry*, 25(5):925–946, 1969.

[114] Jeanet Conradie. Jahn-teller effect in high spin d4 and d9 octahedral metal-complexes. *Inorganica Chimica Acta*, 486:193–199, 2019.

[115] Han-Jin Noh, S. Yeo, J.-S. Kang, C. L. Zhang, S.-W. Cheong, S.-J. Oh, and P. D. Johnson. Jahn-teller effect in spinel manganites probed by soft x-ray absorption spectroscopy. *Applied Physics Letters*, 88(8):081911, 2006.

[116] Yunshan Zheng, Huixian Xie, Junfeng Li, Kwan San Hui, Zhenjiang Yu, Huifang Xu, Duc Anh Dinh, Zhengqing Ye, Chenyang Zha, and Kwun Nam Hui. Insights into the jahn-teller effect in layered oxide cathode materials for potassium-ion batteries. *Advanced Energy Materials*, 14(14), 2024.

[117] J. A. Alonso, M. J. Martínez-Lope, M. T. Casais, and M. T. Fernández-Díaz. Evolution of the jahnteller distortion of MnO6 octahedra in RMnO3 perovskites (r = pr, nd, dy, tb, ho, er, y): A neutron diffraction study. *Inorganic Chemistry*, 39(5):917–923, 2000.

[118] Elena O. Filatova, Yulia V. Egorova, Kristina A. Galdina, Tobias Scherb, Gerhard Schumacher, Henny J.M. Bouwmeester, and Stefan Baumann. Effect of fe content on atomic and electronic structure of complex oxides sr(ti,fe)o3. *Solid State Ionics*, 308:27–33, 2017.

[119] Eungje Lee, Dennis E. Brown, Esen E. Alp, Yang Ren, Jun Lu, Jung-Je Woo, and Christopher S. Johnson. New insights into the performance degradation of fe-based layered oxides in sodium-ion batteries: Instability of fe3+/fe4+ redox in -NaFeO2. *Chemistry of Materials*, 27(19):6755–6764, 2015.

[120] R Stoyanova, M Gorova, and E Zhecheva. EPR of mn4+ in spinels li1+xMn2xO4 with 0x0.1. *Journal of Physics and Chemistry of Solids*, 61(4):609–614, 2000.

[121] Wencong Wang, Wei Liu, Masao Kamiko, and Shunsuke Yagi. Enhanced catalytic activity of perovskite la 1x sr x MnO 3+ for the oxygen reduction reaction. *New Journal of Chemistry*, 46(27):13082–13088, 2022.

[122] Guilherme Oliveira Siqueira, Rose Marie Belardi, Pedro Hespanha Almeida, Charles Luís da Silva, Márcia Caldeira Brant, Tulio Matencio, and Rosana Zacarias Domingues. Determination of the mn3+/mn4+ ratio in la1xSrxMnO3d powders. *Journal of Alloys and Compounds*, 521:50–54, 2012.

[123] Zhiyuan Chen, Christiaan Zeilstra, Jan van der Stel, Jilt Sietsma, and Yongxiang Yang. Review and data evaluation for high-temperature reduction of iron oxide particles in suspension. *Ironmaking & Steelmaking*, 47(7):741–747, 2020.

[124] Lukas Braun, Jonas Spielmann, Dmitry E. Doronkin, Carola Kuhn, Aleksandr Maliugin, Dmitry I. Sharapa, Isabel Huck, Jianing Bao, Steffen Tischer, Felix Studt, Olaf Deutschmann, Ulrike I. Kramm, and Jan-Dierk Grunwaldt. Following the structural changes of iron oxides during reduction under transient conditions. *ChemSusChem*, 17(24):e202401045, 2024.

[125] Michael D. Sanders, Anyka M. Bergeson-Keller, Eric N. Coker, and Ryan P. O'Hayre. A thermogravimetric temperature-programmed thermal redox protocol for rapid screening of metal oxides for solar thermochemical hydrogen production. *Frontiers in Energy Research*, 10:856943, 2022.

[126] Christopher L. Muhich, Samuel Blaser, Marie C. Hoes, and Aldo Steinfeld. Comparing the solar-to-fuel energy conversion efficiency of ceria and perovskite based thermochemical redox cycles for splitting h2o and CO2. *International Journal of Hydrogen Energy*, 43(41):18814–18831, 2018.